Monte Carlo Summation of Higher Order Feynman Diagram Expansions For Strongly Correlated Electron Models

by

Wenduo Zhou

(Under the direction of Heinz-Bernd Schüttler)

Abstract

The Hubbard model is one of the most important solid state physics models to describe strongly correlated electron systems. Unfortunately, an exact or reliable approximate method for solving this model has still not been found. The self-consistent diagrammatic expansion method is a useful tool to obtain approximate solutions. However, the current computing power limits both the sizes of physical systems and the orders of diagrammatic approximation that can be treated by conventional numerical brute force summation approaches. In order to overcome this obstacle, we have developed a novel technique, combining Monte Carlo summation, with the self-consistent conserving diagrammatic approximation method. We demonstrate the feasibility of our method by applying it to the two-dimensional Hubbard Model at band filling $\frac{1}{2}$, searching for the Mott-Hubbard gap and studying the strong antiferromagnetism.

Index words: two dimensional Hubbard model, many-body electronic interacting system, High-T_c superconductor, Feynman diagram, Fermi liquid, Monte Carlo summation

Monte Carlo Summation of Higher Order Feynman Diagram Expansions For Strongly Correlated Electron Models

by

Wenduo Zhou

B.S., Shanghai Jiaotong University, 1996

M.S., The University of Georgia, Athens, GA, 2004

A Dissertation Submitted to the Graduate Faculty

of The University of Georgia in Partial Fulfillment

of the

Requirements for the Degree

Doctor of Philosophy

Athens, Georgia

2006

Monte Carlo Summation of Higher Order Feynman Diagram Expansions For Strongly Correlated Electron Models

by

Wenduo Zhou

Approved:

Major Professor: Heinz-Bernd Schüttler

Committee: Bill Dennis
David Landau
Steven Lewis

Electronic Version Approved:

Maureen Grasso
Dean of the Graduate School
The University of Georgia
August 2006

Dedication

To My Parents and Grandmother

Acknowledgments

Prof. Heinz-Bernd Schüttler, my major professor has offered me much useful advice and great help in my research. I'd like to express my gratitude to him for the guidance. I wish to acknowledge Prof. Bill Dennis, Prof. David Landau and Prof. Steve Lewis for serving as my advisory committee members. I want to thank Prof. Mark Jarrell for providing me with the maximum entropy code, and Prof. Robert W. Robinson for providing me with the self-energy graphs and vertex graphs. I want to show my thanks to Dr. Shan-ho Tsai, Mike Caplinger and Jeff Deroshia for their assistance with the computing facility.

I would like to thank my parents and my grandmother. Without the support from them, I would never have enough strength to undertake and carry out my research.

This research was supported by NSF Grant DMR-0081789.

Table of Contents

List of Figures

List of Tables

Chapter 1

Introduction

The Hubbard model [1] is at the center of strongly correlated electron physics due to its ability to account for the most fundamental aspects of interacting electrons in solids. It takes into account both the delocalization and repulsive Coulomb interaction of the electrons. The Hubbard model is a highly simplified version of the inhomogeneous electron gas (IEG) model of a solid, written in terms of a Wannier basis function representation. Three simplifying approximations are needed to reduce the inhomogeneous electron gas model to the (extended) Hubbard model. First is the truncation of the electron Hilbert space to retain only the Wannier orbitals associated with the electronic conduction band(s). Second, all 3-center and 4-center Coulomb interaction matrix elements of these Wannier orbitals are neglected. Third, all 2-center Coulomb matrix elements, except for the most dominant "direct" interaction elements, are neglected. The result of these approximations is referred to as the extended Hubbard model. If, in addition, all 2-center Coulomb interaction matrix elements are neglected, and only the single-center or "on-site" Coulomb interaction is retained, we has the the so-called pure Hubbard model. In spite of its simplicity, the model exhibits a very rich phenomenology and is able to provide insights into various condensed matter phenomena, including those observed in high-T_c superconductors (HTS) and heavy fermion materials. The two dimensional Hubbard model, which is believed to be essential to explain the high-T_c cuprates [2], cannot be solved exactly. Even numerical approaches face great difficulty in the intermediate and strong coupling regime (the intermediate and strong coupling regimes are defined respectively as those parameters of the regimes of the model with on-site Coulomb repulsion matrix element that is comparable to or much large than the electron

bandwidth). Many numerical methods, such as quantum Monte Carlo [3][4][5], dynamical mean field theory [6][7], dynamical cluster approximation [8], and exact diagonalization [9], have been developed for this purpose. So far all these methods have not led to a complete understanding of the Hubbard model, and especially the question about the possible superconducting phase in the Hubbard model.

In this thesis, we introduce a novel method to calculate the self-energy and the single- and two-particle Green's functions of the Hubbard model self-consistently based on a finite-order version of the "conserving approximation" scheme by Baym[10]. The number of Feynman diagrams grows exponentially with the perturbation order, and at intermediate and strong coupling, the high order Feynman diagrams make a non-negligible contribution to the self-energy. In order to overcome this obstacle, we employ an iterated self-consistent perturbation expansion to include all diagrams that are comprised in a much smaller subset, i.e, so-called irreducible Feynman diagrams. This subset is truncated at a specific finite order cut-off. However, with increasing expansion order, even the number of irreducible Feynman diagrams, even though only a minor subset of all Feynman diagrams, does also increase exponentially, and the computation complexity for calculating the self-energy grows accordingly.

The Monte Carlo summation technique is an essential element of our approach. It provides us with an efficient method to carry out the summations over high-dimensional momentum and frequency domains that are necessary to calculate the self-energy contributions from high-order Feynman diagrams with a satisfactory precision in realistic CPU times.

We implement this methodology to calculate the imaginary-frequency one-particle Green's function, self-energy and two-particle irreducible vertex function of the two-dimensional Hubbard model. The Mott-Hubbard gap is then searched for in the two-dimensional Hubbard model by several different approaches, including the single-particle spectral function and the compressibility. The strong antiferromagnetism of the Hubbard model is demonstrated by studying the spin susceptibility as a function of wave vector and temperature. We also show that the higher-order diagrammatic corrections are essential to

the formation of the Mott-Hubbard gap, and that they are able to push the Neél transition seen in the spin susceptibility to a much lower temperature compared to the lower-order approximation.

The thesis is organized as follows: A general introduction on the Hubbard model, especially in two dimension case, is given in Chapter 2. In Chapter 3, the self-consistent diagrammatic approximation methods, which are designed to calculate the Green's function, the self-energy and the single electron spectral function are explained in detail, along with the introduction of our Monte Carlo summation technique. The approximation approach to calculate the irreducible vertex function and, from it, the spin susceptibility is discussed. Our simulation results are presented in Chapter 4. For simplicity and due to the limitation of time and computational resources, we only studied the single-band Hubbard model with only a non-zero first neighbor hybridization term on the two-dimensional square lattice (mostly for 4×4 and in some cases 8×8 lattices) with periodic boundary conditions. We demonstrate the convergence of the self-consistent Monte Carlo approach, and discuss results for the Green's function, the self-energy, the spectral function and density of states of the two-dimensional Hubbard model in order to search for the existence of the Mott-Hubbard gap. We also show a series of results for the spin susceptibility in the first- and second-order approximation, and discuss its temperature and wave vector dependence. Finally, in Chapter 5, we present our conclusion and discuss the future work. In the Appendix, some detailed formalisms, which are related to previous discussions, are shown.

Chapter 2

General Introduction To The Hubbard Model

2.1 The Hubbard Model in Solid State Physics

Originally proposed as a model of magnetic and electrical transport properties of transition metals, the Hubbard model, introduced independently by Gutzwiller[11], Hubbard [1] and Kanamori [12], is the simplest realistic model of correlated electron systems, containing only the essential aspects of electrons in a solid - the competition and interplay between Coulomb interaction and kinetic energy of the electrons, the filling of the available electronic band and the structure of underlying lattice.

In decades of study, the Hubbard model as been used to describe various phenomena including ferromagnetism and antiferromagnetism, superconductivity, the Mott-Hubbard metal-insulator transition and antiferromagnetic correlations for a certain class of transition metals and transition metal oxides [13][14][15][16][17][18], including the high-T_c cuprates [2] and low-T_c ruthenates [19]. Since the discovery of superconductivity in the cuprate $LaCuO_4$ [20], the mechanism of high-T_c superconductivity has become a center of interest in condensed matter physics. The importance of the two-dimensional (2D) Hubbard model lies in the fact that all known high-T_c cuprate superconductors exhibit a common phenomenology in their electronic structure, magnetic transport and optical properties, which is very similar to the "known" properties of the Hubbard model and, specifically, the Hubbard model on a two-dimensional square lattice. The cuprates are layered materials, characterized by the presence of quasi-two-dimensional CuO_2 planes [21]. The term quasi-two-dimensional here refers to the fact that the electronic coupling, specifically the electronic conduction band hybridization, between the CuO_2 layers is much weaker than within each layer. The cuprates

are highly correlated materials with an effective conduction bandwidth comparable to the effective local Coulomb repulsive interaction between the conduction band electrons. In their pure "undoped" form, the cuprates' electronic structure exhibits one conduction band associated with each CuO_2 layer. The quasi-two-dimensional conduction band is half-filled and the undoped cuprates should therefore be metals according to band theory. Yet their observed transport and optical properties show that the undoped cuprates, such as pure La_2CuO_4, are insulators. This insulating behavior is caused by the strong local Coulomb interactions of the conduction electrons and this type of insulators is referred to as a Mott-Hubbard insulator.

Furthermore, all undoped cuprates exhibit strong antiferromagnetic spin correlations, and at temperatures below about 200 - 300 K, long-range antiferromagnetic order. The cuprates become conducting and their antiferromagnetic spin correlations are suppressed by substitutionally doping them with non-iso-electronic ions, which change the conduction band electron density away from half-filling. This general phenomenology is very reminiscent of the "known" physics of the Hubbard model in its strong coupling limit, as described in more detail in Section 2.4. The rich phase diagram of the Hubbard model is of great interest in order to describe the phenomena of these materials and their phase transitions between different ordered states.

2.2 Hubbard Model: Basic theory

While the originally proposed Hubbard model retains only the short-range effects of the electron-electron Coulomb repulsions, the longer-range part of the Coulomb repulsion could also be important, especially for questions related to the superconducting pairing mechanism in the cuprates. It is therefore of interest to also include long-range Coulomb interaction effect in the framework of the Hubbard model, which thus leads to the so-called extended Hubbard model. The extended Hubbard model describes spin-$\frac{1}{2}$ electrons moving in a crystalline solid. It assumes that band electrons interact via a two-body repulsive Coulomb interaction and

the vast set of electron bands and continuum electron levels of each ion can be approximately reduced to a single or sometimes a few localized orbital levels.

Specifically the extended single-band Hubbard model is based on a representation of the electronic structure in terms of a basis of conduction band Wannier functions $\phi_{j\sigma}(\vec{x},\xi)$ of a general form

$$\phi_{j\sigma}(\vec{x},\xi) \;\; = \;\; \tilde{\phi}(\vec{x}-\vec{r}_j)\delta_{\sigma\xi} \tag{2.1}$$

where the site index j indicates a lattice site located at lattice vector $\vec{r}_j$, and σ is the spin index of the Wannier orbital that denotes spin eigenstates $\sigma =\uparrow$ or $\downarrow$. Also, ξ is the electron spin coordinate, and $\vec{x}$ is the electron position coordinate vector.

The orbital part of the Wannier function $\tilde{\phi}(\vec{x}-\vec{r}_j)$ is assumed to be centered around lattice vector $\vec{r}_j$. This $\tilde{\phi}(\vec{x}-\vec{r}_j)$ can be constructed from the Bloch wave functions of the conduction band [22]. We assume that there is only one conduction band, i.e., all other electron energy bands of the solid, except for the conduction band, are either completely full or completely empty. The basic approximation underlying the single-band Hubbard model is then to neglect all non-conduction band orbitals and retain only the conduction band Wannier orbitals $\phi_{j\sigma}$. This can provide an adequate description of the physics of the electrons for excitation energy scales of the order of 2 to 3 eV or less, i.e., at energy scales below the typical interacting-band excitation energy in the cuprates.

Some of the general formalism and basic physics discussed below will not depend on the specific choice of the lattice structure. However,we will implicitly assume simple cubic or tetragonal lattices in D-dimensions with periodic boundary conditions, and will ultimately focus on the $D = 2$ square lattice, with period boundaries and

$$N = L \times L \tag{2.2}$$

unit cells, where L is the linear lattice size of square lattice sites. Because the set of single-band Wannier functions is orthonormal and incomplete, the Hilbert space is truncated by

the restriction that only one Wannier function is allowed per unit cell. In some other cases the other orbital Wannier functions are kept, leading to the multi-band Hubbard model [23].

In addition to the single-band (or few-band) Hilbert-space truncation, the Hubbard model introduces further approximations involving the neglect of certain less important "inter-site" matrix elements of the electron-electron Coulomb interaction, as described in great detail in the literature [23][24]. The larger "on-site" Coulomb matrix elements are retained in the model; they constitute the so-called "extended Hubbard" interaction. The largest of these is the matrix element for the on-site Coulomb repulsive interaction, which plays a fundamental role in the physics of the conduction electron system. The grand canonical Hamiltonian for the extended Hubbard model in Wannier function basis is given by

$$\hat{H} = -\sum_{ij,\sigma} t_{ij} c^{+}_{i\sigma} c_{j\sigma} + \frac{1}{2} \sum_{ij\sigma\rho} V_{ij} c^{+}_{i\sigma} c^{+}_{j\rho} c_{j\rho} c_{i\sigma} - \sum_{i\sigma} \mu c^{+}_{i\sigma} c_{i\sigma} \tag{2.3}$$

where $c^{(+)}_{i\sigma}$ is the annihilation (creation) operator for an electron in $\phi_{i\sigma}$, localized at a lattice site $\vec{r}_i$ with spin $\sigma(=\uparrow,\downarrow)$, and the hybridization matrix elements t_{ij}, related to the kinetic energy, enter the hybridization term between sites $\vec{r}_i$ and $\vec{r}_j$. Site indices i and j will be summed over all N lattice sites, while σ and ρ will be summed over spin up ($\uparrow$) and spin down ($\downarrow$). μ is the chemical potential. Since the lattice has translational symmetry, $t_{ij} = t(\vec{r}_i - \vec{r}_j)$. Any hybridization terms beyond first nearest neighbors are referred to as longer-range hybridization matrix elements. V_{ij} are the Coulomb interaction matrix elements to be discussed below.

The extended Hubbard interaction can also be written in terms of electron number operators $\hat{n}_i$

$$\hat{H} = -\sum_{ij,\sigma} t_{ij} c^{+}_{i\sigma} c_{j\sigma} + \frac{1}{2} \sum_{ij} V_{ij} (\hat{n}_i - \frac{1}{2})(\hat{n}_j - \frac{1}{2}) - \sum_{i} \tilde{\mu} \hat{n}_i \tag{2.4}$$

where

$$\hat{n}_j = \sum_\sigma \hat{n}_{j\sigma}; \tag{2.5}$$

$$\hat{n}_{j\sigma} = c^+_{j\sigma} c_{j\sigma} \tag{2.6}$$

$$\tilde{\mu} = \mu - \Delta\mu \tag{2.7}$$

and $\Delta\mu$ is given by

$$\Delta\mu = \frac{1}{2}\sum_j V_{ij}. \tag{2.8}$$

$\tilde{\mu}$ is also called the particle-hole symmetric chemical potential. Note that $\Delta\mu$, as defined here, is independent of the site index i in Equation 2.8 due to the translational invariance of V_{ij}, i.e., $V_{ij} = V(\vec{r}_i - \vec{r}_j)$, and due to the translational invariance of the lattice with periodic boundary conditions.

The interaction term with the matrix elements V_{ij} comes from the repulsive Coulomb interaction between the electrons and is independent of spin. Thus the on-site interaction (i.e., $\vec{r}_i = \vec{r}_j$) is the Coulomb repulsion between two electrons with opposite spins both occupying the same Wannier orbital on the same lattice site, whereas the off-site interaction is the Coulomb repulsion between two Wannier electron clouds localized at two different sites. Due to the localized Wannier charge distribution, the off-site interaction V_{ij} with $i \neq j$ can be approximated by the Coulomb interaction between two point charges located at two lattice sites $\vec{r}_i$ and $\vec{r}_j$. The extended Hubbard interaction can be then written as

$$V_{ij} = \begin{cases} U & \text{if } \vec{r}_i = \vec{r}_j \\ V_1/(|\vec{r}_i - \vec{r}_j|/a) & \text{if } \vec{r}_i \neq \vec{r}_j \end{cases} \tag{2.9}$$

where U is the on-site interaction and V_1 is the Coulomb interaction between the first nearest neighbors, and where $|\vec{r}_i - \vec{r}_j|$ denotes the shortest distance between $\vec{r}_i$ and $\vec{r}_j$ on a finite lattice subject to periodic boundary condition and a is the first neighbor distance. Note that this form of V_{ij} preserves the translational invariance, since $V_{ij} = V(\vec{r}_i - \vec{r}_j)$.

By lattice Fourier transform, Bloch annihilation(creation) operators in momentum space $d_{\vec{k}\sigma}$ ($d^+_{\vec{k}\sigma}$) can be constructed from real space annihilation(creation) operators by

$$d_{\vec{k}\sigma} = \frac{1}{\sqrt{N}} \sum_j e^{-i\vec{k}\cdot\vec{r}_j} c_{j\sigma} \tag{2.10}$$

where j is summed over all lattice sites, N is number of the lattice sites, and $d_{\vec{k}\sigma}$ ($d^+_{\vec{k}\sigma}$) annihilates (creates) an electron in Bloch state with crystal lattice momentum $\vec{k}$ and spin σ. The crystal lattice momentum $\vec{k}$ resides in the first Brillouin zone, in a finite subset $\mathcal{B}_L$, given for the two-dimensional square lattice by

$$\mathcal{B}_L = \{\vec{k} = (\frac{2\pi l_x}{L}, \frac{2\pi l_y}{L}) | -\frac{L}{2} < l_x \leq \frac{L}{2}, -\frac{L}{2} < l_y \leq \frac{L}{2}, l_x,\, l_y \text{ are integer}\}. \tag{2.11}$$

$\mathcal{B}_L$ is the finite set of distinct, allowed $\vec{k}$-vectors in the first Brillouin zone of a finite square lattice $L \times L$ with periodic boundary conditions as illustrated in Figure 2.1.

The Hamiltonian of the extended Hubbard Model can now be written in momentum space as

$$\hat{H} = \sum_{\vec{k}\in\mathcal{B}_\mathcal{L}} (\epsilon_{\vec{k}} - \mu) d^+_{\vec{k}\sigma} d_{\vec{k}\sigma} + \sum_{\substack{\vec{k},\vec{k}',\vec{q}\in\mathcal{B}_L; \\ \sigma,\sigma'=\uparrow\downarrow}} \frac{1}{2N} V(\vec{q}) d^+_{\vec{k}+\vec{q},\sigma} d^+_{\vec{k}'-\vec{q},\sigma'} d_{\vec{k}'\sigma'} d_{\vec{k}\sigma}, \tag{2.12}$$

$V(\vec{q})$ is the lattice-Fourier-transformed interaction given by

$$V(\vec{q}) = \frac{1}{N} \sum_{ij} e^{-i\vec{q}\cdot(\vec{r}_i - \vec{r}_j)} V_{ij} \tag{2.13}$$

and the interaction term describes scattering of electrons and exchange of momentum due to interaction. The band energy $\epsilon_{\vec{k}}$ is related to the hybridization terms by

$$\epsilon_{\vec{k}} = \frac{1}{N} \sum_{ij} e^{-i\vec{k}\cdot(\vec{r}_i - \vec{r}_j)} t_{ij}. \tag{2.14}$$

For example, if we include only the two non-zero hybridization terms for first and second neighbor hybridization, respectively on a 2D square lattice denoted by t_1 and t_2, the band energy is

$$\epsilon_{\vec{k}} = -2t_1(\cos(k_x) + \cos(k_y)) - 4t_2 \cos(k_x) \cdot \cos(k_y). \tag{2.15}$$

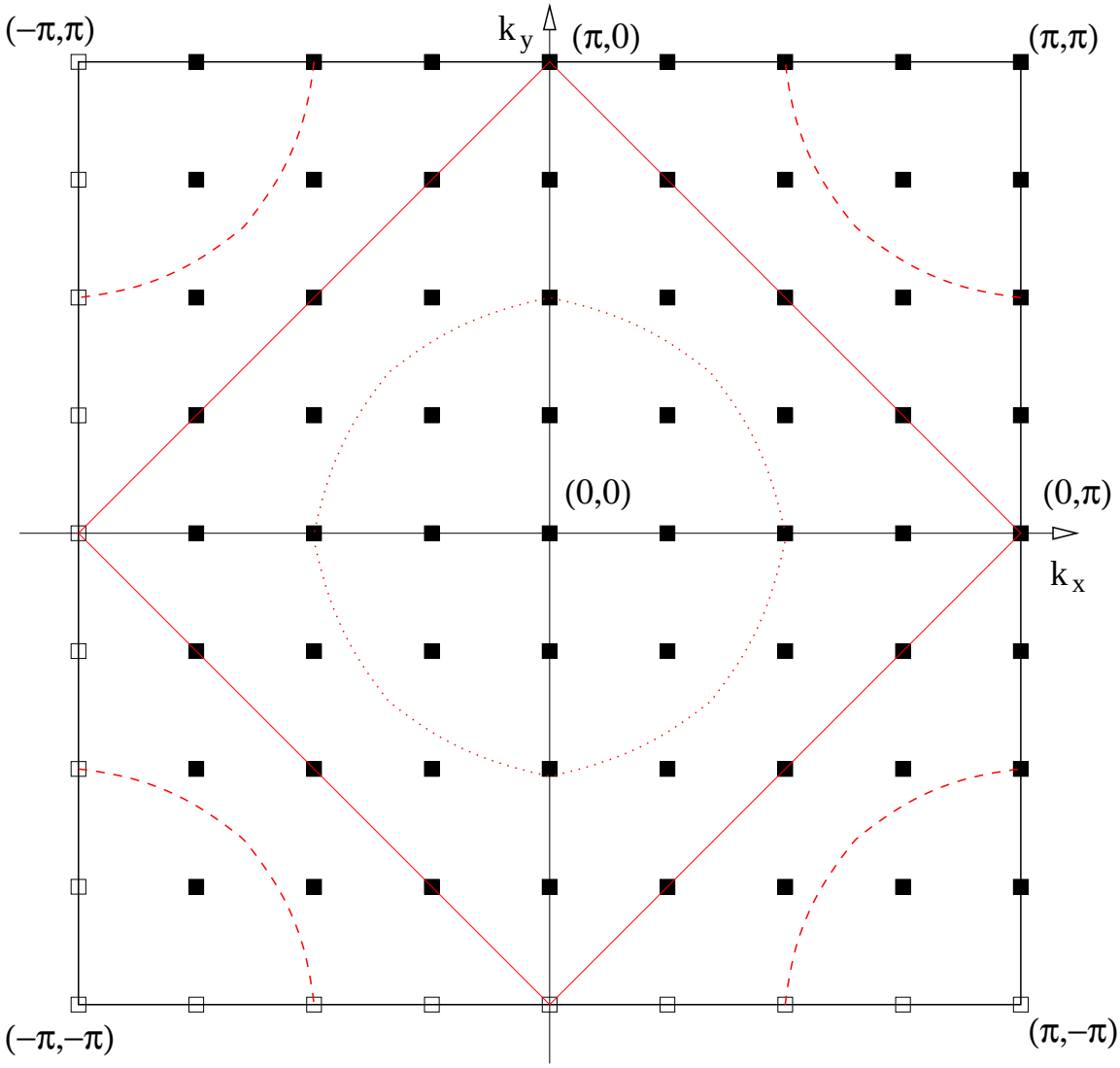

Figure 2.1: Example of conduction electron band filling in momentum space for the non-interacting electron system on a two-dimensional square lattice with first neighbor hybridization only ($t_1 \neq 0$, $t_2 = t_3 = \cdots = 0$), i.e., $\epsilon_{\vec{k}} = -2t_1(\cos k_x + \cos k_y)$. The Fermi "surface", i.e., contours of constant band energy, $\epsilon_{\vec{k}} = \mu = \text{const}$, are shown for chemical potential μ is 0, $2t_1$ and $-2t_1$, depicted by red solid-, dash- and dotted-line respectively corresponding to band filling $\rho_e = 0.50$, 0.82 and 0.18 respectively in the thermodynamic limit $N \to \infty$. Note that the ρ_e is equal to the fraction of the Brillouin zone in term of interior "volume" delimited by the Fermi surface. Also shown for illustration is the discrete grid of allowed $\vec{k}$-points for a finite lattice of size $N = 8 \times 8$, with closed square symbols denoting 64 distinguishable $\vec{k}$-points and open square symbols denoting additional $\vec{k}$-points that are indistinguishable from closed ones by $\vec{k}$-space periodicity. The full square with corners (π, π), $(-\pi, -\pi)$, $(-\pi, \pi)$ and $(\pi, -\pi)$ is the first Brillouin zone. All $\vec{k}$-vector components are given in units of $1/a$ where a is the lattice constant.

We also define $\tilde{\epsilon}_{\vec{k}}$ hereafter such that

$$\tilde{\epsilon}_{\vec{k}} \;=\; \epsilon_{\vec{k}} - \mu. \tag{2.16}$$

The band width W can be determined by $\epsilon(\vec{k})$ such that

$$W = \epsilon^{+} - \epsilon^{-}, \tag{2.17}$$

where ϵ^{+} is the maximum value of $\epsilon(\vec{k})$ and ϵ^{-} is the minimum value (The symbol W here should not be confused with the Monte Carlo weight function defined in Chapter 3). For instance, if the first neighbor hybridization term t_1 is nonzero, and the second neighbor hybridization term t_2 is limited by

$$-\frac{t_1}{2} \leq t_2 \leq \frac{t_1}{2}$$

the band width

$$W = 8t_1.$$

In the grand canonical ensemble, the average occupation number $\langle\hat{n}\rangle$ is thus defined as

$$\langle\hat{n}\rangle \;=\; \frac{1}{N}\sum_{\vec{k}\sigma}\langle d^{+}_{\vec{k}\sigma} d_{\vec{k}\sigma}\rangle = \sum_{\sigma}\langle c^{+}_{j\sigma} c_{j\sigma}\rangle \tag{2.18}$$

Here the grand canonical thermal average is defined by

$$\langle\hat{A}\rangle \;\equiv\; \frac{\mathrm{Tr}(e^{-\beta\hat{H}}\hat{A})}{\mathrm{Tr}(e^{-\beta\hat{H}})} \tag{2.19}$$

for any observable $\hat{A}$. The average occupation number $\langle\hat{n}\rangle$ is determined by the chemical potential μ and is usually expressed in terms of the so-called electron band filling, ρ_e, by

$$\langle\hat{n}\rangle = 2\rho_e \tag{2.20}$$

where ρ_e is the fraction of electron $\vec{k}$-states in the conduction band that would be occupied in the non-interacting limit of the model ($V_{ij} = 0$) for the same $\langle\hat{n}\rangle$. ρ_e ranges from 0 to 1, and the factor of 2 in Equation 2.20 is due to the spin degeneracy of each $\vec{k}$-state. Figure 2.1

gives an example of electron conduction band filling in $\vec{k}$-space on a square lattice for the non-interacting system. In the following we will use the term "band-filling" to refer to ρ_e even in model parameter regimes where a conventional band picture may not apply to describe the physics of the model.

The extended Hubbard model is characterized by spin rotation symmetry and gauge symmetry. Under spin rotation symmetry,

$$[\hat{H}, U_s(\vec{u})] = 0 \tag{2.21}$$

with the unitary operator

$$U_s(\vec{u}) = e^{i\vec{u}\cdot\vec{S}_{tot}} \tag{2.22}$$

where $\vec{u}$ is an arbitrary three-dimensional unit vector. The site spin vector operator $\vec{S}_j$ is defined as

$$\vec{S}_j \;=\; (S_j^{(x)}, S_j^{(y)}, S_j^{(z)})$$

where the components of $\vec{S}_j$ given by

$$S_j^{(\alpha)} \;=\; \sum_{\sigma,\rho=\uparrow\downarrow} \frac{1}{2}\hat{\sigma}_{\sigma\rho}^{(\alpha)} c_{j\sigma}^{+} c_{j\sigma}$$

and $\hat{\sigma}^{(\alpha)}$ denote the Pauli matrices for $\alpha = x$, y, and z. Then

$$\vec{S}_{tot} \;=\; \sum_j \vec{S}_j \tag{2.23}$$

The gauge symmetry is the property that

$$[\hat{H}, e^{i\phi\hat{N}_e}] = 0 \tag{2.24}$$

where

$$\hat{N}_e = \sum_{j\sigma} \hat{n}_{j\sigma} \tag{2.25}$$

is the total electron number operator. and ϕ is the gauge angle.

In addition, if the longer range hybridization matrix elements (beyond first neighbor) vanish, the Hubbard model on a bipartite lattice has particle-hole symmetry for a special choice of the chemical potential, namely for,

$$\Delta\mu = \mu \tag{2.26}$$

$$\tilde{\mu} = 0 \tag{2.27}$$

in Equation (2.8) and Equation (2.7) respectively, such that its Hamiltonian is unchanged under the particle-hole transformation (Appendix A). If the model is particle-hole symmetric, the system is precisely half-filled ($\langle\hat{n}\rangle = 1$), i.e., it holds one electron per lattice site on average, for all values of the V_{ij} and all allowed t_{ij} parameters in the Hamiltonian at any temperature T. The diamond shaped noninteracting half-filled Fermi surface in Figure 2.1 has a special significance, even for the interacting system, i.e., it is the locus of all $\vec{k}$-points which are invariant (i.e., mapped onto themselves) under the particle-hole transformation in $\vec{k}$-space (see Equation (A.13) and Equation (A.14) in Appendix A.2). As a consequence of particle-hole symmetry, the Green's function and spectral functions for $\vec{k}$-points on the diamond-shape Fermi surface have special symmetry properties, as derived in Appendix A and shown later in Chapters 3 and 4.

In the interacting system (with $V_{ij} \neq 0$), it is still possible to define a so-called "interacting Fermi surface" in the zero-temperature limit, $T \to 0$, provided that the system "maintains" Fermi liquid behavior, as shown by Kohn and Luttinger [25] [26] [27] [28] and described in more detail in Chapter 3 and Appendix D. In this situation, the interacting Fermi surface of the half-filled particle-hole symmetric system can be shown to be identical to the non-interacting diamond-shaped surface in Figure 2.1 due to its particle-hole invariance. We will therefore refer to this special particle-hole-invariant half-filled Fermi surface as "the Fermi surface" in all further discussions of the results for the particle-hole symmetric Hubbard model in Chapter 3 and Chapter 4 even for the interacting system $V_{ij} \neq 0$.

2.3 The Original Hubbard Model

The original Hubbard model [1][11][12] (also called the pure Hubbard model, the on-site Hubbard model or just *the* Hubbard model) is a special case of the extended Hubbard model, where only the on-site interaction is considered, i.e, Equation (2.9) becomes

$$V_{ij} = \begin{cases} U & \text{if } \vec{r}_i = \vec{r}_j \\ 0 & \text{if } \vec{r}_i \neq \vec{r}_j. \end{cases} \tag{2.28}$$

The Hamiltonian in coordinate space is thus simplified to

$$\hat{H} = -\sum_{ij\sigma} t_{ij} c^+_{i\sigma} c_{j\sigma} + \frac{U}{2} \sum_{j\sigma\rho} c^+_{j\sigma} c^+_{j\rho} c_{j\rho} c_{j\sigma} - \sum_{j\sigma} \mu c^+_{j\sigma} c_{j\sigma}. \tag{2.29}$$

from Equation (2.3), and

$$\hat{H} \;=\; -\sum_{ij,\sigma} t_{ij} c^+_{i\sigma} c_{j\sigma} + \frac{U}{2} \sum_{j} (\hat{n}_{j\uparrow} - \frac{1}{2})(\hat{n}_{j\downarrow} - \frac{1}{2}) - \sum_{j} \tilde{\mu} \hat{n}_j \tag{2.30}$$

from Equation (2.4) where as Equation (2.7)

$$\tilde{\mu} \;=\; -\frac{U}{2} + \mu.$$

The Hubbard model in momentum space can be written as

$$\hat{H} \;=\; \sum_{\vec{k}\in\mathcal{B};\sigma=\uparrow\downarrow} \tilde{\epsilon}_{\vec{k}} d^+_{\vec{k}\sigma} d_{\vec{k}\sigma} + \frac{U}{2N} \sum_{\vec{k},\vec{k}',\vec{q}\in\mathcal{B};\sigma,\rho=\uparrow\downarrow} d^+_{\vec{k}+\vec{q},\sigma} d^+_{\vec{k}'-\vec{q},\rho} d_{\vec{k}'\rho} d_{\vec{k}\sigma}. \tag{2.31}$$

If the Hubbard model has particle-hole symmetry, then from Equation (2.26), the chemical potential μ is exactly half the magnitude of the on-site repulsion U, i.e.,

$$\mu = \frac{U}{2}. \tag{2.32}$$

We will always use the term "Hubbard model" to refer to Equations (2.29), (2.30) and (2.31) in the following. The models in Equations (2.3), (2.4) and (2.12) will always be referred to as the "extended Hubbard model". The actual model calculations reported in this thesis, in Chapter 4, are all for the case of the pure Hubbard model. The extended Hubbard model has been introduced here only to develop the general formalism of our simulation method and to illustrate the generality of this formalism and the simulation method.

2.4 Hubbard Model In The Atomic and Strong-Coupling Limit

The physics of the Hubbard model in atomic and strong-coupling limit at half-filling is reasonably well understood.

The atomic limit of the Hubbard model is obtained by setting all hybridization terms $t_{ij} = 0$, and retaining only the on-site repulsion U. For a half-filled system $\langle \hat{n} \rangle = 1$, the ground state of the Hubbard model then consists of the eigenstates of all occupation number operator $\hat{n}_{j\sigma}$ with exactly one electron per lattice site. The ground state therefore has degeneracy of 2^N, where N is the number of lattice sites, since at each site j, we can choose occupation numbers so that either $n_{j\uparrow} = 1$, $n_{j\downarrow} = 0$, or $n_{j\uparrow} = 0$, $n_{j\downarrow} = 1$, corresponding to spin z-component $s_j = +\frac{1}{2}$ or $s_j = -\frac{1}{2}$, respectively. For example, both states in Figure 2.2A and Figure 2.2B are ground states. If we want to move an electron, i.e., transport charge, between different lattice sites, we need to excite the system to its first excited state where one site becomes doubly occupied, as shown in Figure 2.2C. The excitation energy gap Δ between the ground state and first excited state is therefore

$$\Delta = U. \tag{2.33}$$

Having a required finite excitation energy $\Delta > 0$ to transport charge is characteristic of an electrical insulator [29].

In the cuprate materials, the removal or addition of conduction band electrons is achieved by doping the pure insulating parent compounds with p-type or n-type substitutional dopant ions respectively. We will therefore also refer to lowering of band-filling away from $\rho_e = 1/2$ as "p-doping" or "hole doping" in the context of the Hubbard model. Likewise, we will refer to an increase above $\rho_e = 1/2$ as "n-doping" or "electron doping".

If we change the band-filling, for example by removing one electron from the half-filled ground state, as shown in Figure 2.2D, then we can move an electron between different sites without having to excite the system to a higher energy state. Therefore, doping away from half-filling has the effect of destroying the charge excitation gap. Being able to transport

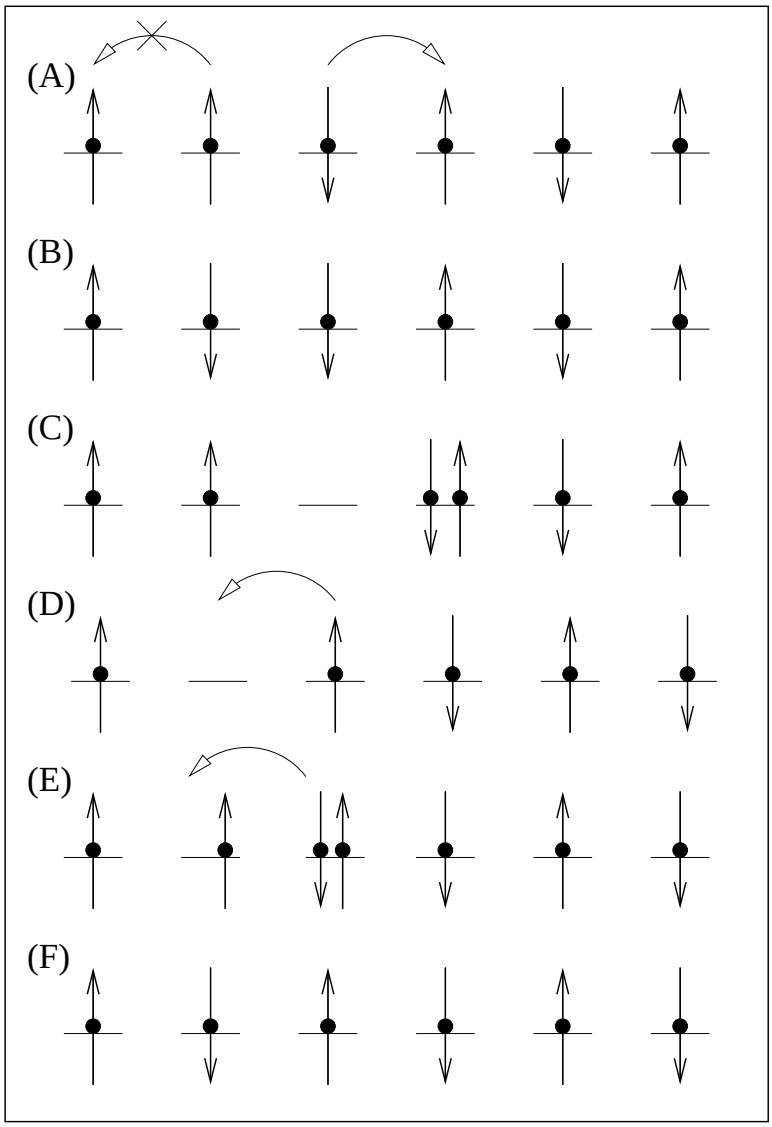

Figure 2.2: A one-dimensional Hubbard chain with 6 lattice sites is used to illustrate the basic physics of the atomic and strong-coupling limit of the Hubbard model. The same qualitative ideas apply to the higher-dimensional case. The arrows in the graph are used to illustrate the movement of an electron from one lattice site to another one. The cross sign on the arrow means that this kind of movement is not allowed. (A) and (B) are two degenerate ground states of the Hubbard model in the atomic limit. (C) is the first excitation state generated from (A). (D) is an example for under-doped (p-type) Hubbard model. Moving the electron to a non-occupied site won't affect the ground state energy. (E) is an example for over-doped (n-type) Hubbard model. Moving the electron from a double-occupied site to another single-occupied site won't affect the ground state energy. (F) is a cartoon of the antiferromagnetic ground state of the Hubbard model in the strong-coupling limit. Strictly speaking (F), the so-called Neél state, is not an exact ground state of the Heisenberg model, but rather of the corresponding Ising model, where only the $S_i^{(z)} S_j^{(z)}$ terms in Equation (2.34) are retained.

charges without having to supply a minimum excitation energy across a gap, i.e., $\Delta = 0$, is characteristic of a metal.

If we turn on a hybridization $t_{ij} \neq 0$ in the Hamiltonian, but with $U \gg |t_{ij}|$, the doping-induced extra hole in Figure 2.2(D), the doping-induced extra electron in Figure 2.2(E)), and also the excitation-induced pair of extra-electron and extra-hole in Figure 2.2 (C) become mobile and the respective degenerate manifolds of $t_{ij} = 0$ eigenstates are mixed and broadened into energy bands. These bands are referred to as the "lower Hubbard band" and the "upper Hubbard band" for the manifold of states represented by Figure 2.2(D) and Figure 2.2(E) respectively. Hubbard bands represent correlated many-body eigenstates of the Hamiltonian. They are therefore very different from, and cannot be represented by, single-electron energy bands known from conventional band theory.

Note here that only the doping-induced extra holes in the lower Hubbard band or extra electrons in the upper Hubbard band are freely mobile and contribute to electrical charge transport. The electrons in the half-filled system are basically "frozen in" by the large Mott-Hubbard gap $\Delta \sim U$. These frozen in electrons only produce a correlated insulating "spin background" in which the doping-induced carriers move. In this sense, the lower and upper Hubbard band have a certain analogy to the valence and the conducting band states of a conventional weakly correlated semiconductor (or insulator), described by conventional band theory. In this semiconductor analogy the upper Hubbard band corresponds to the energy states of a single electron, added by n-doping, to the semiconductor conduction band, and the lower Hubbard band corresponds to the energy states of a single hole, added by p-doping to the semiconductor valence band. This analogy will be made more explicit in the spin density wave electron band picture described in Section 2.5. However, the crucial difference between a conventional band semiconductor and a strongly interacting Hubbard system is that in a conventional semiconductor, the undoped insulating state consists of a valence band which is completed filled with electrons and a separate conduction band which is completely empty. By contrast, in the case of the Mott-Hubbard insulator, the undoped state comprises only

a single half-filled band, represented by its single-occupied Wannier orbitals. Thus, in the absence of the strong local Coulomb repulsion U, the half-filled system would actually be a metal, according to band theory. The insulating behavior of the half-filled Hubbard system is therefore not caused by band-filling effects, but rather by the strong local Coulomb repulsion U. This insulating behavior of a partially-filled band system constitutes a complete breakdown of the conventional band picture.

If the on-site repulsion U is much larger than the hybridization terms t_{ij}, i.e., $U \gg |t_{ij}|$, but the t_{ij} are non-zero, we have realized the so-called strong-couping limit of he Hubbard model. Because the electrons are now allowed to hop to different lattice sites, in the half-filled ground state the antiferromagnetic alignment of spin is preferred, as shown in figure 2.2F. This preferential antiferromagnetic alignment can be simply understood as a consequence of the delocalization energy gain from the t_{ij} term and of the Pauli principle. As illustrated in Figure 2.2A, for the two middle sites, the spins are anti-parallel, and therefore the spin down ($\downarrow$) electron, for example, can delocalize by hopping to the other site, occupied already by the spin up ($\uparrow$) electron, thereby lowering the total energy of the system. However, for the leftmost sites in Figure 2.2A, the electron spins are parallel, the Pauli principle prohibits delocalization between these two sites and therefore prevents a delocalization energy gain. By a more systematic second-order perturbation theory, the original Hubbard model Hamiltonian at band filling $\frac{1}{2}$ can be approximately mapped to a spin-$\frac{1}{2}$ Heisenberg model

$$H_J = \sum_{ij} J_{ij} \vec{S}_i \cdot \vec{S}_j \tag{2.34}$$

with the antiferromagnetic exchange coupling J_{ij} given by

$$J_{ij} = \frac{4t_{ij}^2}{U} \tag{2.35}$$

in terms of the original Hubbard parameters. The Hilbert space of H_J is restricted to the states with $n_j = 1$ at all sites. In the most relevant case for the cuprates,

$$t_1 \gg |t_2| \ , \ |t_3|, \cdots \tag{2.36}$$

where t_2, t_3, ... are the second, third, ... neighbor hybridization terms, we can reduce H_J to a first neighbor antiferromagnetic coupling model which has an antiferromagnetic ground state [30].

Due to the continuous nature of the group of spin rotations shown in Equation (2.21), the Mermin-Wagner Theorem [31][32][33] prevents the Hubbard or Heisenberg model from having any long-range antiferromagnetic or other long-range magnetic order at finite temperature $T > 0$. However from extensive simulational and analytical work [30][34][35], we know that the model exhibits spatially very extended, finite-range antiferromagnetic spin correlations when T becomes smaller than the first neighbor exchange

$$J_1 \cong \frac{4t_1^2}{U}. \tag{2.37}$$

For $T \ll J_1$, the correlation length ξ is known to grow exponentially with $1/T$, i.e., roughly as [30]

$$\xi \propto \exp(|\text{const}| \times J_1/T). \tag{2.38}$$

(True long-range antiferromagnetic order at finite temperature ($T > 0$) can of course develop in the real "quasi-two-dimensional" cuprate materials due to three-dimensional antiferromagnetic coupling between the CuO_2 layers which makes these material three-dimensional antiferromagnets.) The existence of strong antiferromagnetic spin correlations has also been demonstrated directly in the Hubbard model by exact quantum Monte Carlo simulations [9] (the term "exact" here means that the results of this kind of Monte Carlo simulation agree with the exact result within Monte Carlo statistical error. And the Monte Carlo statistical error can be systematically reduced by increasing Monte Carlo sample size), as well as in approximate mean-field type treatments [36].

If we dope away from half-filling, the strong-coupling expansion maps the Hubbard model onto the so-called t-J model which is a generalization of the Heisenberg model, given by

$$H_{tJ} \quad = \quad H_t + H_J + H'_J \tag{2.39}$$

where H_t is different for hole- and electron-doped model,

$$H_t = \begin{cases} \sum_{ij\sigma} t_{ij}(1-\hat{n}_{j\bar{\sigma}})c^+_{i\sigma}c_{j\sigma} & \text{hole-doped} \\ \sum_{ij\sigma} t_{ij}\hat{n}_{j\bar{\sigma}}c^+_{i\sigma}c_{j\sigma} & \text{electron-doped} \end{cases} \tag{2.40}$$

and H'_J is defined as

$$H'_J \;=\; -\sum_{ij}\frac{1}{4}J_{ij}(\hat{n}_i-1)(\hat{n}_j-1) \tag{2.41}$$

which represents an effective attractive interaction between the doping-induced hole or extra electron carriers. Again, the Hilbert space for this model is truncated to allow only the subspace whose $n_i = 0$ or 1 for the hole-doped case and $n_i = 1$ or 2 for the electron doped case. H_{tJ} describes the motion of either doping induced extra holes or doping induced extra electrons in the antiferromagnetic correlated spin background. In other words H_{tJ} describes the energy states associated with the motion of doping-induced charge carriers in the lower Hubbard band only for hole-doping, or in the upper Hubbard band only for electron doping. The higher energy "particle-hole" excitations, as shown in Figure 2.2(C), are not explicitly included in the H_{tJ} Hilbert space. Rather, they are eliminated by a perturbative procedure [9]. To order $(t_{ij})^2$ these "virtual excitations" are what give rise to the antiferromagnetic couplings J_{ij}. It is believed that the kinetic energy associated with these doping induced charge carriers is responsible for bringing about metallic-like electrical conductivity and the suppression of spatially extended antiferromagnetic spin correlations in the doped Hubbard model.

The physics of the Hubbard model in the atomic and strong-coupling limit is therefore very similar to the high-T_c cuprates, and it is believed that the Hubbard model is able to explain at least some of the phenomenology of the cuprates. However, one of the central questions, whether the two-dimensional Hubbard model or the quasi-two-dimensional extension thereof can explain high-T_c superconductivity, is still open.

2.5 Non-interacting Limit of the Hubbard Model and Hartree-Fock Mean-field Theory

In the non-interacting limit case, we set the Hubbard interaction $V_{ij} = 0$ in Equation (2.4). The exact solutions of the Hubbard model in the non-interacting limit are the common eigenstates of the occupation number operators in $\vec{k}$-space, defined as

$$\hat{m}_{\vec{k}\sigma} := d^{+}_{\vec{k}\sigma} d_{\vec{k}\sigma}. \tag{2.42}$$

At zero temperature $T = 0$, all states $(\vec{k}, \sigma)$ with band energy below chemical potential μ, such that $\epsilon_{\vec{k}\sigma} \leq \mu$, are occupied, whereas all the states above the chemical potential, such that $\epsilon_{\vec{k}\sigma} > \mu$, are empty. The total energy of the Hubbard model ground state thus is the sum of band energy $\epsilon_{\vec{k}\sigma}$ of all occupied states, given by

$$E \;=\; \sum_{\vec{k}\sigma} m_{\vec{k}\sigma} \epsilon_{\vec{k}\sigma} \tag{2.43}$$

where $m_{\vec{k}\sigma}$ denotes the eigenvalue of $\hat{m}_{\vec{k}\sigma}$, with $m_{\vec{k}\sigma} = 0$ or 1. In the thermodynamic limit, the grids in crystal momentum space become continuous, so that there is no gap for excitation across the Fermi energy. Hence, in this case, the system is metallic at any non-integer banding filling include half-filling ($\rho_e = 1/2$).

As the Hubbard interaction V_{ij} is turned on, the Hubbard model can be treated in the Hartree-Fock mean-field approximation [9][37][38], where the interaction term in Equation (2.12) is approximated by replacing the 4-fermion-operator products like $d^{+}_{\vec{k}+\vec{q},\sigma} d^{+}_{\vec{k}'-\vec{q},\sigma'} d_{\vec{k}'\sigma'} d_{\vec{k}\sigma}$ with

$$2 d^{+}_{\vec{k}+\vec{q},\sigma} d_{\vec{k}\sigma} \langle d^{+}_{\vec{k}'-\vec{q},\sigma'} d_{\vec{k}'\sigma'} \rangle + (-2) d^{+}_{\vec{k}+\vec{q},\sigma} d_{\vec{k}'\sigma'} \langle d^{+}_{\vec{k}'-\vec{q},\sigma'} d_{\vec{k}\sigma} \rangle.$$

This leads to an "effective" or "mean-field" Hamiltonian which consists only of terms with 2-fermion-operator products and which, therefore, can be diagonalized exactly by solving for the corresponding "mean-field" single-electron eigenstates. The required "mean fields", $\langle d^{+}_{\vec{k}'-\vec{q},\sigma'} d_{\vec{k}'\sigma'} \rangle$ and $\langle d^{+}_{\vec{k}'-\vec{q},\sigma'} d_{\vec{k}\sigma} \rangle$ are then calculated self-consistently by taking the thermal or ground state averages with the exact Hamiltonian replaced by the mean-field Hamiltonian.

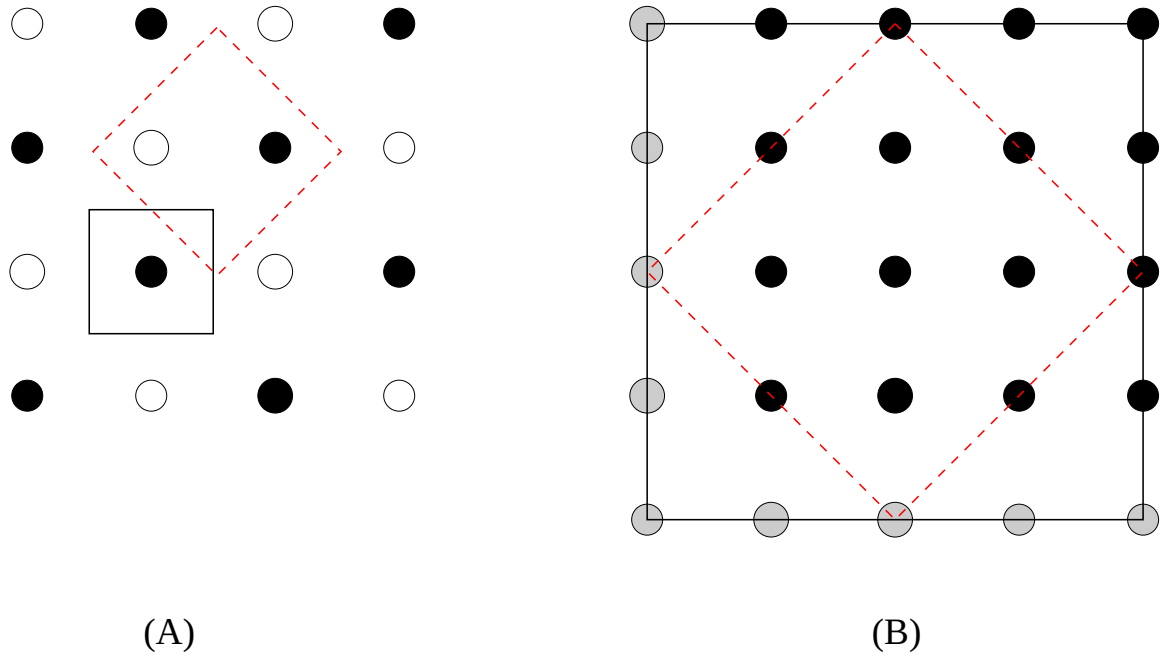

Figure 2.3: (A) A 4×4 lattice is shown with partitioning into two sublattices: sublattice A (open circles) and sublattice B (closed circles). Note that the unit cell (depicted as a solid-line square) contains one site regardless of sublattice, and the two-site unit cell (depicted as a red dashed-line diamond) contains one sublattice A and one sublattice B site. (B) The first Brillouin zone for the single-site unit cell (black solid-line square) and the two-site unit cell (red dashed-line diamond) are shown. The latter coincides the non-interacting Fermi surface of the previous one. The circles show the discrete grid of allowed $\vec{k}$-points for the 4×4 lattice with periodic boundary conditions. The black circles are a complete set of such $\vec{k}$-points, the grey circles are identical to corresponding black circles modulo a reciprocal lattice vector. The first Brillouin zone for the single-site and for the two-site unit cell are referred to as "large" Brillouin zone and "small" Brillouin zone in the following, respectively.

Without any symmetry breaking, the Hartree-Fock mean-field Hamiltonian has the same form as the non-interacting band Hamiltonian, but with a modified energy band. For the pure Hubbard model such that $V_{ij} = U\delta_{ij}$, the energy band in the absence of symmetry breaking is unchanged compared to the non-interacting limit case, except for a constant energy shift which can be absorbed into the chemical potential.

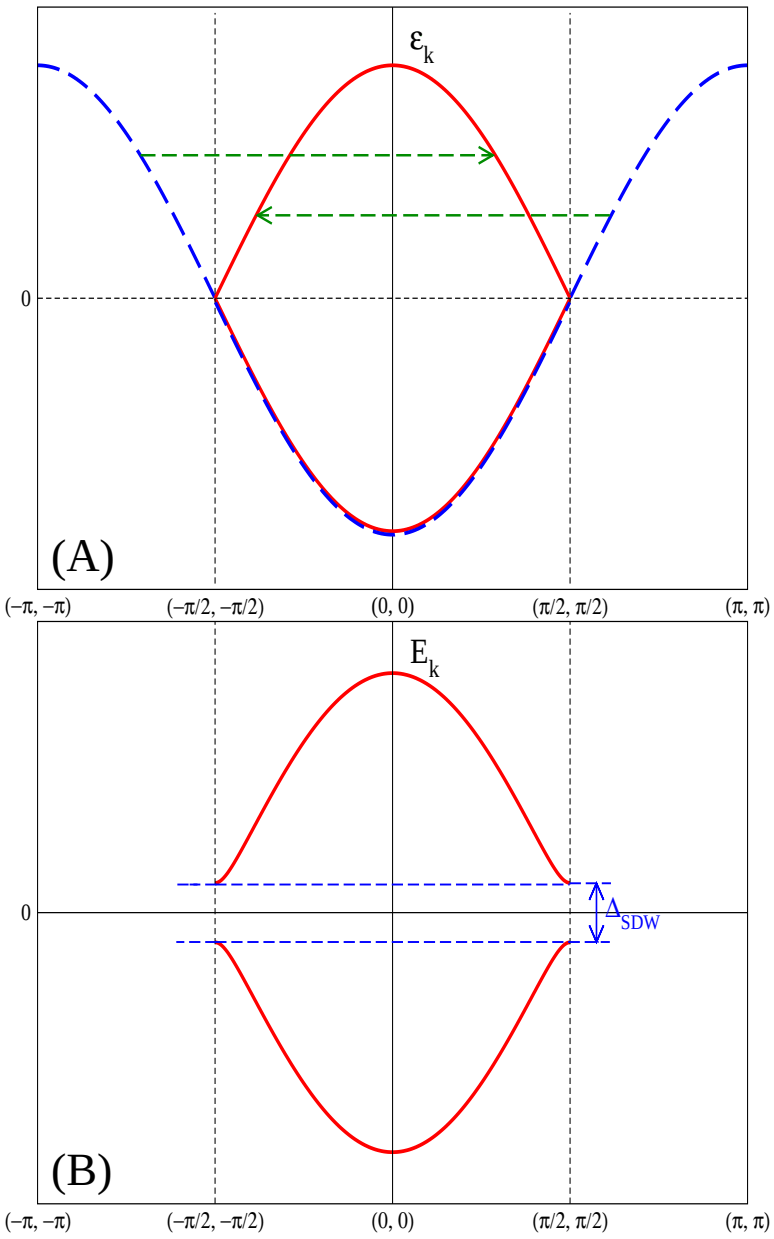

Figure 2.4: (A) The conduction band for a non-interating Hubbard model with first neighbor hybridization $t_1 \neq 0$ only ($t_2 = t_3 = 0$) is plotted along time diagonal ($k_x = k_y$) in the large first Brillouin zone (dashed blue line) and in the small first (solid red line) with "large" and "small' first Brillouin zone defined in Figure 2.3. Note that the portions of the large-zone band falling outside of the small zone are shifted back into the small zone by small-zone reciprocal lattice vectors. Therefore the single conduction band actually becomes two bands in the small-zone representation. (B) The spin density wave (SDW) electron bands for the interacting Hubbard model are treated in the Hartree-Fock approximation with antiferromagnetic symmetry breaking. The bands show a SDW gap between the upper- and lower-SDW band at the reduced first Brillouin zone boundary. The SDW band energy $E_{\vec{k}}$ has the form $E_{\vec{k}} = \pm\sqrt{\epsilon_{\vec{k}} + (\Delta_{SDW}/2)^2}$ for upper and lower SDW band respectively. At half-filling and zero temperature, the lower SDW electron band is completely filled and the upper SDW band is empty.

If antiferromagnetic symmetry breaking is allowed, the corresponding unit cell is doubled and includes two lattice sites, as shown in Figure 2.3, which also implies that the area of the corresponding (new) Brillouin zone is reduced to half the volume of the original Brillouin zone. The new Brillouin zone boundary coincides with the diamond-shaped half-filled Fermi surface shown in Figure 2.1.

The Hartree-Fock mean-field theory with antiferromagnetic symmetry breaking leads to a splitting of the original single conduction band into two sub-bands, referred to as the upper spin density wave (SDW) band and lower SDW band, as shown in Figure 2.4(A). As a result of the Coulomb interaction, a so-called spin density wave gap, Δ_{SDW}, is opened, as shown in Figure 2.4(B). The magnitude of the SDW gap can be determined self-consistently by solving the mean-field equations.

The Hartree-Fock solution with antiferromagnetic symmetry breaking implies long-range spin density wave order,

$$\langle S_j^{(z)} \rangle \quad = \quad M_0 \cdot \exp(-i\vec{Q}^* \cdot \vec{r}_j) \tag{2.44}$$

with spin density wave vector

$$\vec{Q}^* = (\pi, \pi)$$

i.e., the SDW state is therefore an antiferromagnetic state. In the Hartree-Fock approximation, the SDW antiferromagnetic order occurs below a finite transition temperature $T_{SDW} > 0$ in any dimension including $D = 1$ and $D = 2$, and therefore the Hartree-Fock approximation violates the Mermin-Wagner theorem in two dimensions and the fundamental theorem that long-range order cannot exist at finite temperature in one or two dimension.

Nevertheless, the SDW band formation again reproduces very similar "physics" as the atomic and strong coupling limit. At half-filling ($\rho_e = 1/2$), the lower SDW band is completely filled, while the upper SDW band is empty, i.e, the system is in an insulating state and it exhibits antiferromagnetic order as just discussed. Upon doping with holes into the lower SDW band or with electrons into the upper SDW band, the system becomes conducting.

Just like the Mott-Hubbard gap in the strong coupling limit, the SDW gap is a so-called "charge excitation gap" which means that it can be seen in optical absorption or other experiments where the system is perturbed by (external) electrical fields. It is interesting to note that in the strong coupling limit $U \gg |t_{ij}|$, the magnitude of the SDW gap is approximately equal to the on-site interaction U, i.e.,

$$\Delta_{SDW} \cong U$$

in the Hartree-Fock mean-field equation [39][40], which is the same value as the Mott-Hubbard gap Δ in the atomic limit. It is therefore tempting to identify the two SDW bands with the lower and upper Hubbard bands, and identify the SDW gap with the Mott-Hubbard gap.

The Hartree-Fock mean-field theory violates fundamental theorems of statistical mechanics by allowing a continuous symmetry to be broken by a long-range order state at finite temperature T even in one and two dimensions. On the other hand the Mott-Hubbard excitation gap is clearly seen in numerical solutions of the half-filled Hubbard model, even in the absence of any symmetry breaking due to, e.g., long-range antiferromagnetic order [3]. A central question of strongly correlated electron systems is therefore whether the basic physics of both the strong coupling limit and the SDW symmetry broken Hartree-Fock mean-field theory (insulator with excitation gap and antiferromagnetic spin correlation) can be reproduced by systematic, extensions of the Hartree-Fock mean-field theory. It is the main goal of this thesis work to employ a systematic self-consistent perturbative formalism to go beyond Hartree-Fock theory and to develop the algorithmic tools for actually implementing this formalism computationally.

Chapter 3

Green's Function Formalism

3.1 General Introduction

The method that we use to treat the two dimensional Hubbard model is a self-consistent diagrammatic expansion combined with a Monte Carlo summation technique. Our method employs a Baym-Kadanoff-type [41] of "self-consistent conserving approximation". The term "conserving" here refers to the fact that all the fundamental symmetries and resulting conservation laws, such as gauge symmetry and particle-number conservation, or spin rotational symmetry and total spin conservation, will be fully preserved by the approximation scheme of all levels of approximation (i.e., at all orders orders of diagrammatic expansions up to the maximum order). For example, the Ward identities [42] related to particle number and spin conservation are automatically obeyed. The Hartree-Fock approximation is the lowest order version of this more general approach.

Our Monte Carlo summation method, which will be introduced later in this chapter, is used to carry out the summations over high-dimensional momentum and frequency domains required in the high order diagram expansions. The method can be applied to finite lattices and systematically extrapolated to infinite lattice size $L \to \infty$. The important advantage of this Monte Carlo summation method is that, at any level (or so-called "order") of approximation, the computation time grows only linearly with the lattice volume $N = L \times L$, as defined in Equation 2.2.

Obviously, as a tradeoff, the drawback of the diagrammatic expansion approximation is that the solution is not exact, but can be (in principle) systematically improved by going to the next higher level of approximation. On the other hand, to date there is still no

proof that the self-consistent expansion method will converge as approximation order n_{max} approaches infinity. At large approximation order n_{max}, the total number of so-called diagram topologies, which need to be summed over, grows exponentially or super-exponentially with n_{max}. Hence our specific approach of summing by brute force over all diagram topologies, as described below, cannot be extended beyond 6th order at the very most with current computing resources. We must then resort to carrying out summations over diagram topologies along with momentum-frequency-summations by the Monte Carlo method, though this approach may substantially increase the statistical errors. In this thesis, we will develop and explore only the "partial Monte Carlo summation" approach. The "complete Monte Carlo summation" approach described above will remain for future studies.

The basic diagrammatic formalism of our approach has been fully developed in the literature, notably in the works of Feynman [37][38], Matsubara [37][38], Kohn, Luttinger [25][26][27][28], Ward [42], Baym and Kadanoff [41] and others in the 1950s and 1960s. In the following sections, we will therefore introduce the basic formal graph theoretic definitions that are required for the full computational implementation of this formalism and we will then only summarize the primary diagram expansion results required for our numerical work without any detailed derivations.

3.2 Single-Particle Green's Function

The one-particle Green's function (also called "propagator") plays a fundamental role in interacting many body physics, determining the excited states associated with creation or annihilation of one particle in a system in thermodynamic equilibrium. The one-particle Green's function is also the fundamental building block for all self-energy diagrams to be computed in our calculations. Hence, the starting point of our calculationss is the evaluation of the single-particle Green's function.

Although our formalism is described here for the two-dimensional extended Hubbard model, the formalism is much more general. It applies in all finite dimensions and can even be

extended to infinite dimension [7]. It can also be extended beyond the single-band Hubbard model to more realistic multi-band models. However, to be specific, we assume that the model that we study is defined on a square lattice, consisting of $N = L \times L$ lattice sites, with repulsive interaction V_{ij}, chemical potential μ, first and second nearest neighbor hopping, t_1 and t_2 respectively as described in the previous chapter. In the following, all energies are expressed in units of the first nearest neighbor hopping amplitude t_1, if not otherwise stated explicitly.

In momentum-imaginary-time domain, the single-particle Green's function is defined as [37] [38]

$$G(\vec{k},\tau) \;=\; -\langle T_\tau[d_{\vec{k}\sigma}(\tau)d^+_{\vec{k}\sigma}(0)]\rangle, \tag{3.1}$$

where, τ is the so-called imaginary time variable with $-\beta < \tau < \beta$, $\beta = 1/T$ for temperature T, and T_τ is the Fermion time ordering operator, and where $d_{\vec{k}\sigma}$ is the annihilation operator for an electron in a Bloch state with crystal momentum $\vec{k}$ and spin σ as defined in Equation (2.10). The notation $\langle A\rangle$ is again the grand canonical ensemble average for any operator$A$, as defined in Equation (2.19). The imaginary time evolution of any operator A is defined here by

$$A(\tau) \;=\; \exp(\hat{H}\tau)A\exp(-\hat{H}\tau). \tag{3.2}$$

In the absence of spin rotational symmetry breaking, $G(\vec{k},\tau)$ is independent of spin index σ in Equation (3.1). The Green's function in the so-called momentum-Matsubara-frequency domain is related to $G(\vec{k},\tau)$ via the Fourier series

$$G(\vec{k},\tau) \;=\; T\sum_{i\nu_m} e^{-i\nu_m\tau}G(\vec{k},i\nu_m) \tag{3.3}$$

where,

$$G(k) \;\equiv\; G(\vec{k},i\nu_m) = \int_0^\beta e^{i\nu_m\tau}G(\vec{k},\tau). \tag{3.4}$$

Here the symbol k without vector arrow is used to denote a (D+1)-dimensional momentum-Matsubara-frequency vector

$$k \equiv (\vec{k}, i\nu_m) \tag{3.5}$$

for the general case of a D-dimensional lattice, where $\vec{k}$ is the D-dimensional crystal momentum, and $i\nu_m$ is the odd Matsubara frequency, defined as

$$i\nu_m \quad = \quad (2m+1)\pi i T \tag{3.6}$$

with integer m and $i^2 = -1$. Formally, we can write

$$k \in \mathcal{K} \equiv \mathcal{B}_L \times \mathcal{M}_- \tag{3.7}$$

where $\mathcal{B}_L$ is defined in Equation (2.11) and $\mathcal{M}_-$ is the odd Matsubara frequency set defined as

$$\mathcal{M}_- \quad := \quad \{i\nu_m | \nu_m = (2m+1)\pi T, \text{m is integer}\}. \tag{3.8}$$

We will later also need even Matsubara frequencies, defined as

$$i\omega_m \quad = \quad 2m\pi i T \tag{3.9}$$

for integer m and the even Matsubara frequency set, defined as

$$\mathcal{M}_+ \quad := \quad \{i\omega_m | \omega_m = 2m\pi T, m \text{ is integer}\}. \tag{3.10}$$

The $\vec{k}$-space occupation number can be obtained directly from the Green's function as

$$\langle \hat{m}_{k\sigma} \rangle = \langle d^+_{\vec{k}\sigma} d_{\vec{k}\sigma} \rangle = \lim_{\tau \to 0^+} G(\vec{k}, -\tau). \tag{3.11}$$

The Green's function can be evaluated by the Feynman-Dyson perturbation theory [37][38]. In the momentum-Matsubara-frequency domain $(\vec{k}, i\nu_m)$, the Green's function is then given by, so-called Dyson equation,

$$G(k) \quad = \quad \frac{1}{i\nu_m - \epsilon_{\vec{k}} + \mu - \Sigma(k)} \equiv \frac{1}{G^{(0)}(k)^{-1} - \Sigma(k)} \tag{3.12}$$

where the self-energy $\Sigma(\vec{k}, i\nu_m)$ includes all interaction effects and the non-interacting single-particle Green's function is given by

$$G^{(0)}(k) \;=\; \frac{1}{i\nu_m - \epsilon_{\vec{k}} + \mu} \tag{3.13}$$

with $\epsilon_{\vec{k}}$ given by Equation (2.15) in Section 2.2 for the case of two-dimensional Hubbard model.

Since both $G(\vec{k}, \tau)$ and $\Sigma(\vec{k}, \tau)$ (the inverse-Fourier sums of $G(\vec{k}, i\nu_m)$ and $\Sigma(\vec{k}, i\nu_m)$) are real-valued, $G(\vec{k}, \tau)$, and $\Sigma(\vec{k}, \tau)$ obey the symmetry relations

$$G(\vec{k}, -i\nu_m) = G^*(\vec{k}, i\nu_m) \quad \text{and} \quad \Sigma(\vec{k}, -i\nu_m) = \Sigma^*(\vec{k}, i\nu_m). \tag{3.14}$$

Also $G(\vec{k}, \tau)$ and $\Sigma(\vec{k}, \tau)$ are invariant under all point group symmetry operations of the lattice, applied to $\vec{k}$, and they are defined to obey $\vec{k}$-space periodicity for $\vec{k}$-vectors outside $\mathcal{B}_L$, i.e.,

$$G(\vec{k} + \vec{K}, i\nu_m) = G(\vec{k}, i\nu_m) \quad \text{and} \quad \Sigma(\vec{k} + \vec{K}, i\nu_m) = \Sigma(\vec{k}, i\nu_m) \tag{3.15}$$

for reciprocal lattice vector $\vec{K}$.

3.3 Perturbation Series for Self-energy

In the Feynman-Dyson approach, the self-energy is the sum of certain perturbation expansion terms, called diagrams. Each diagram has each a representation in terms of a certain labeled, rooted graph, with an associated set of so-called Feynman rules for the calculation of the value of the diagram for given graph topology. In Figure 3.1, a few examples of first, second and third order self-energy diagrams are shown. In general, a self-energy diagram is characterized by an integer number, its order n. A graph of order n is constructed as follows:

1. Draw $2n$ internal vertices, shown as filled circular dots in Figure 3.1, and 2 external vertices, shown as open circles in Figure 3.1. Number all the vertices with an integer labelling v running from $v = 0$ to $v = 2n + 1$, with $v = 0$ and $v = 2n + 1$ reserved for the external vertices and $v = 1, 2, \cdots, 2n$ for the internal vertices;

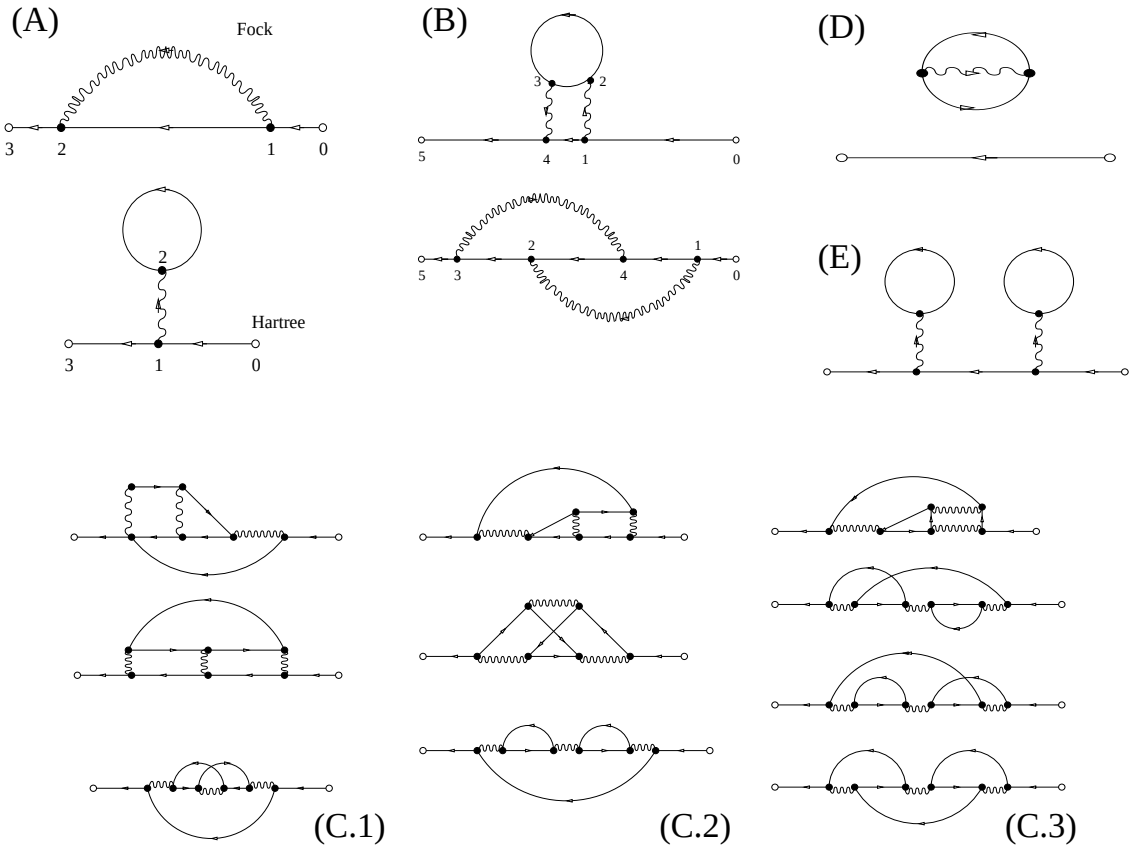

Figure 3.1: Examples of self-energy graphs, including (A) First-order irreducible self-energy graphs (Hartree and Fock); (B) Second-order irreducible self-energy graphs; (C) Third-order irreducible self-energy graphs; (D) Example of a first-order disconnected self-energy graph; and (E) Example of a second-order reducible self-energy graph.

2. Connect the internal vertices with directed wavy lines, so-called V-lines, so that each odd-numbered internal vertex v and its following even numbered vertex $v+1$ are connected by a V-line, and the V-line points from v to $v+1$;

3. Connect all vertices by directed, straight lines, so-called G-lines, in such a manner that each internal vertex has two G-lines attached, with one of the G-lines' arrow pointing towards the vertex and the other G-line's away from it. Each external vertex, $v=0$ and $v=2n+1$, should have only one G-line attached, with the G-line's arrow pointing away from $v=0$ and towards $v=2n+1$.

Every such graph (denoted by g) can be formally represented as a one-to-one mapping

$$g\colon \{0,1,\cdots,2n\} \rightarrow \{1,2,\cdots,2n+1\} \tag{3.16}$$

such that $v' \equiv g(v)$ is of the termination vertex of the G-line originating from vertex v.

Some of the graphs constructed according to these three rules will be "disconnected", meaning that they consist of disconnected pieces. An example of such a disconnected graph is shown in Figure 3.1(D). These disconnected graphs are not allowed to contribute to the self-energy $\Sigma(k)$ in the self-consistent diagram expansion method that we will be using here [41]. The subset of nth order graphs remaining after eliminating all disconnected graphs is referred to as the *set of connected graphs* of order n.

In the set of connected graphs at each order n, there will now be certain graphs, referred to as the "reducible" graphs, which have the property that they can be partitioned into two disjoint pieces by cutting only one single G-line. An example of such a reducible graph is shown in Figure 3.1(E). These reducible graphs are also not allowed to contribute to the self-energy in our self-consistent diagram expansion method [41], in order to avoid over-counting the diagrams which have already been included by using "fully dressed" interacting Green's function for each G-line. The subset of nth order graphs remaining after eliminating all disconnected and all reducible graphs is referred to as the *set of irreducible graphs* of

order n and is denoted by the symbol $\mathcal{G}_n$ in the following. Figure 3.1(A), Figure 3.1(B) and Figure 3.1(C) show all irreducible graphs g, contained in $\mathcal{G}_1$, $\mathcal{G}_2$ and $\mathcal{G}_3$ respectively.

To calculate the diagram value of a given graph, we next need to assign a momentum-Matsubara vector

$$k_j \equiv (\vec{k}_j, i\nu_{m_j}) \in \mathcal{B}_L \times \mathcal{M}_-$$

to each internal G-line numbered $j = 1, 2, \cdots, 2n-1$, where a G-line is called internal, if both its starting vertex v and ending vertex $g(v)$ are internal, i.e, if $v \in \{1, \cdots, 2n\}$ and $g(v) \in \{1, \cdots, 2n\}$. The subscript j used here to label the k-vector of G-lines in a diagram should not be confused with the lattice site label j introduced in Chapter 2 Equation (2.1). We also assign a momentum-Matusbara vector

$$q_\ell \equiv (\vec{q}, i\omega_{m_\ell}) \in \mathcal{B}_L \times \mathcal{M}_+$$

to each V-line labeled by $\ell = 1, 2, \cdots, 2n$, where $\vec{q}_l$ is again a crystal momentum and $i\omega_{m_l}$ is an even Matsubara frequency. Here, the sets $\mathcal{B}_L$, $\mathcal{M}_-$ and $\mathcal{M}_+$ are defined in Equations (2.11), (3.8) and (3.10) respectively.

For each diagram contribution to $\Sigma(k)$ with $k \equiv (\vec{k}, i\nu_m)$, we also assign the momentum-Matsubara vector

$$k_0 \equiv k_{2n} \equiv k$$

to the incoming and outgoing G-lines, labeled by $j = 0$ and $j = 2n$, respectively, with $j = 0$ originating from external vertex $v = 0$ and $j = 2n$ terminating on external vertex $v = 2n+1$.

We now impose momentum-frequency conservation at each internal vertex, i.e., require that

$$k_{j'} \;=\; k_j \pm q_\ell \tag{3.17}$$

if G-line j points toward some vertex v, j' points away from it and the $+(-)$ sign on the right-hand-side of Equation (3.17) applies if V-line number ℓ points toward (away from)

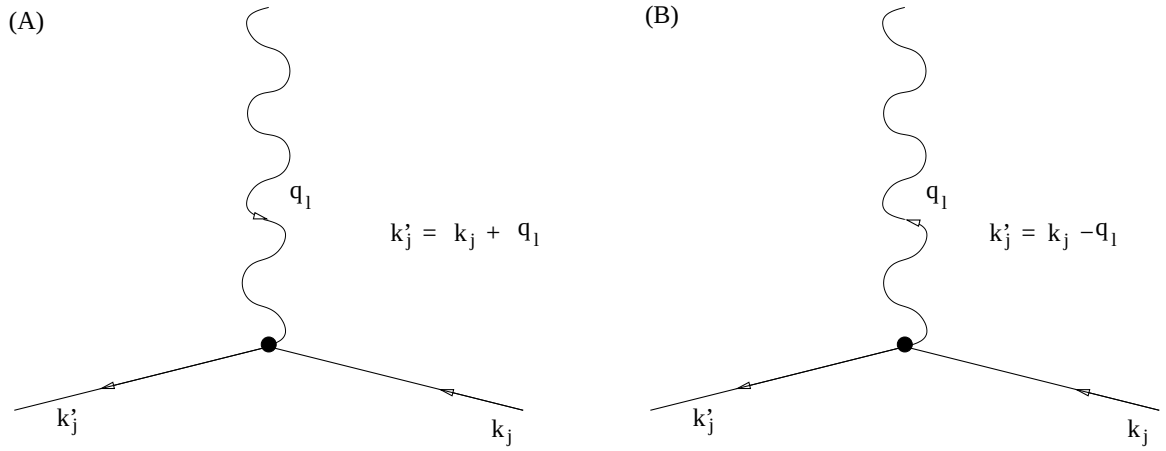

Figure 3.2: The conservation rule on each internal vertex is shown.

vertex v, as illustrated in Figure 3.2(A) and Figure 3.2(B) respectively. Given the external $k_0 \equiv k_{2n} \equiv k$ and the conservation rules (Equation (3.17)), there are thus only n internal G-lines for which k_j can be chosen independently. The k_j of the remaining $n-1$ internal G-lines and the q_l of all V-lines ($l = 1, 2, \cdots, n$) are fully determined as linear functions of $k \equiv k_0$ and of the n independent internal k_j by the conservation rules shown in Equation (3.17). We can always choose a k_j-labeling of the internal G-lines such that the independent k_j are labeled by $j = 1, 2, \cdots, n$ and the dependent k_j by $j = n+1, \cdots, 2n-1$. It is thus convenient to use a new notation and labeling for the dependent k_j by setting

$$\bar{k}_{j-n} := k_j \quad \text{for } j = n+1, \cdots, 2n-1 \tag{3.18}$$

Using this notation, the relations between the dependent and the independent momentum-Matsubara-frequency vectors, k_j, $\bar{k}_j$ and q_ℓ, can be expressed as follows:

$$\bar{k}_j = \textstyle\sum_{j'=0}^{n} \sigma_{\mathrm{G}}(j, j'; g) k_{j'} \quad \text{for } j = 1, \cdots, n-1 \tag{3.19}$$

$$q_\ell = \textstyle\sum_{j'=0}^{n} \sigma_{\mathrm{V}}(\ell, j'; g) k_{j'} \quad \text{for } \ell = 1, \cdots, n \tag{3.20}$$

where the conservation coefficients $\sigma_{\rm G}(j,j';g)$ and $\sigma_{\rm V}(j,j';g)$ depend on the graph topology (Equation (3.19) and Equation 3.20)) and they take on only the values 0, +1 and −1, according to graph theory [43].

The conservation coefficients $\sigma_{\rm G}$ and $\sigma_{\rm V}$ are generated and tabulated, at each order n, by graph theoretical algorithms, along with the topology g [44]. Note also that the assignment of the independent k_j and of the dependent $\bar{k}_j$ to the internal G-lines is not unique. However, graph theory also provides standard algorithms for choosing a unique "canonical" representative k_j-labeling from all possible k_j-labelings within the general framework of the Depth-first search (DFS) method [45].

With this preparation, we can now state the Feynman rules for the calculation of the diagram value of each nth-order graph contributing to $\Sigma(k)$:

1. With each internal G-line, labeled by k_j ($j = 1, 2, \cdots, n$) or by $\bar{k}_j$ ($j = 1, 2, \cdots, n-1$), associate a factor of $G(k_j)$ or $G(\bar{k}_j)$, respectively;

2. With each V-line labeled by q_ℓ ($\ell = 1, 2, \cdots, n$), associate a factor $(-\frac{T}{N})V(q_l)$ where the value of $V(q_\ell)$ is given by,

$$V(q_\ell) \equiv V(\vec{q}_\ell) \tag{3.21}$$

   which is independent of the Matsubara frequency $i\omega_{m_l}$ for $q_l \equiv (\vec{q}_l, i\omega_{m_l})$. The value of $V(\vec{q}_\ell)$ is given by Equation (2.13);

3. With each closed loop of internal G-lines, associate a factor of (-2);

4. In each first order diagram ($n = 1$), introduce a "convergence" factor $\exp(i\nu_m\tau)$ and take the limit $\tau \to 0^+$ after carrying out all Matsubara frequency summations according to rule 5 below.

5. Multiply together all factors listed under (1), (2), (3) and (4), then sum over all internal independent k_j-variables (for $j = 1, \cdots, n$), given the external $k \equiv k_0$. The result of this summation is this graph's contribution to self-energy $\Sigma(k)$.

Therefore, the self-energy diagram sum can be formally written as

$$\Sigma(\vec{k}, i\nu_m) = \lim_{n_{max}\to\infty} \lim_{\tau\to 0^+} \sum_{n=1}^{n_{max}} \sum_{g\in\mathcal{G}_n} (-\frac{T}{N})^n \cdot (-2)^{\Lambda_{n,g}} \sum_{k_1\cdots k_n\in\mathcal{K}} \exp(\delta_{n,1} i\nu_{m_1}\tau) \times \prod_{j=1}^{n} G(k_j) \times \prod_{j=1}^{n-1} G(\bar{k}_j) \times \prod_{\ell=1}^{n} V(q_\ell) \quad (3.22)$$

where $\mathcal{G}_n$ is the set of nth order self-energy graphs, $\Lambda_{n,g}$ is the number of closed internal G-line loops in an nth order diagram of topology g, and ν_{m_j} is the Matsubara frequency part of $k_j \equiv (\vec{k}_j, i\nu_{m_j})$. The values of dependent momentum-frequency vectors $\bar{k}_j$ and q_ℓ are calculated from the independent momenta k_j and k, using $\sigma_{\rm G}$ and $\sigma_{\rm V}$ of the specific graph g according to Equation (3.19) and Equation (3.20).

3.4 Spin-Restricted Diagram Series For The Pure Hubbard Model

For the pure Hubbard model, the subset of allowed self-energy graphs included in Equation (3.22) can be further restricted by exploiting the strictly local (on-site) form of the interaction matrix $V_{ij} = U\delta_{ij}$. Due to the locality, the spin summation over the spin variables σ and ρ in Equation (2.29) can be restricted to only those spin configurations with $\rho \neq \sigma$, i.e.,

$$\frac{U}{2} \sum_{j\sigma\rho} c^+_{j\sigma} c^+_{j\rho} c_{j\rho} c_{j\sigma} = \frac{U}{2} \sum_{j,\sigma\neq\rho} c^+_{j\sigma} c^+_{j\rho} c_{j\rho} c_{j\sigma},$$

since it is not allowed to have two electrons with same spin coordinates ($\sigma = \rho$) on the same site j, according to the Pauli principle, i.e., because $c^+_{j\sigma} c^+_{j\rho} = c_{j\sigma} c_{j\rho} = 0$ if $\sigma = \rho$. This restriction on the spin summation allows us to further reduce the set of graph topologies required in the self-energy summation Equation (3.22), as follows.

For an nth order graph $g \in \mathcal{G}_n$, we assign a spin variable σ_λ to every closed loop λ of internal G-lines where $\lambda = 1, 2, ..., \Lambda_{n,g}$. Here, a "closed loop" is defined formally as a sequence of M_λ vertices $v^{(\lambda)}_1$, $v^{(\lambda)}_2$, ..., $v^{(\lambda)}_{M_\lambda}$ such that

$$v^{(\lambda)}_{m+1} = g(v^{(\lambda)}_m) \quad m = 1, \cdots, M_\lambda \quad (3.23)$$

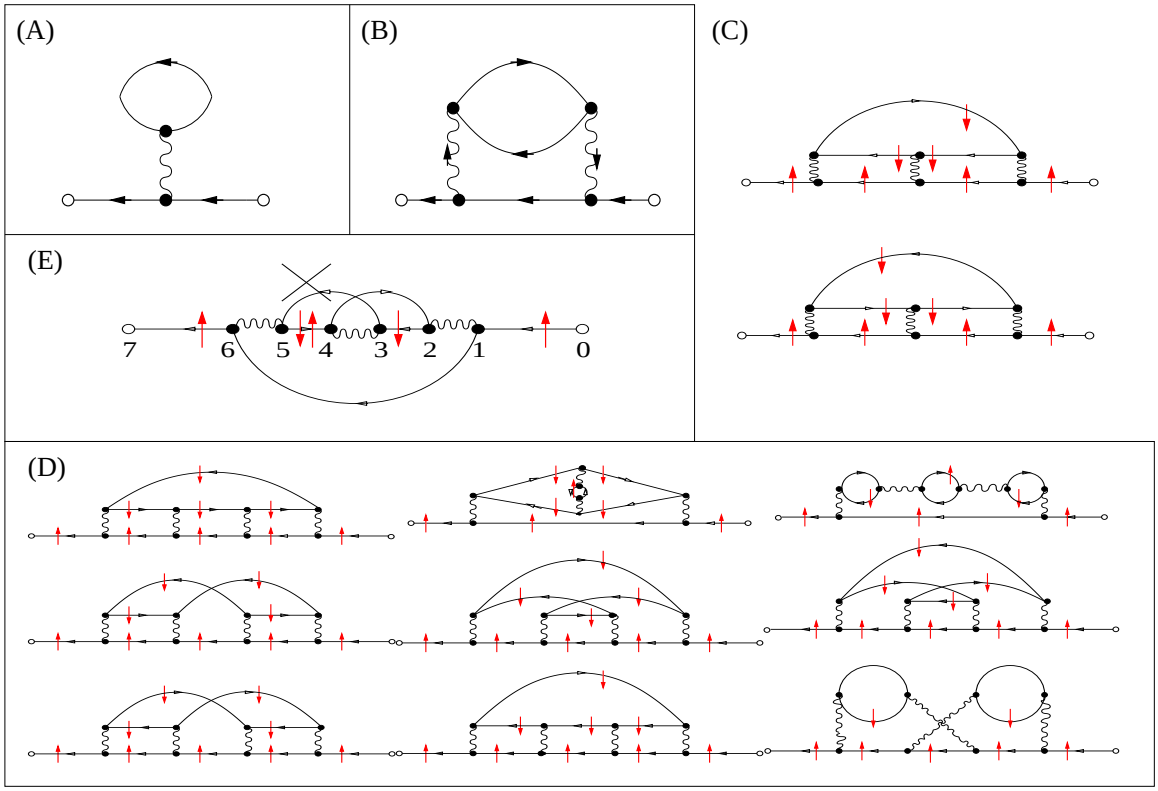

Figure 3.3: (A) First-order up-down irreducible self-energy graph. (B) Second-order up-down irreducible self-energy graph. (C) Third-order up-down irreducible self-energy graphs. (D) Fourth-order up-down irreducible self-energy graphs. (E) A third-order irreducible self-energy graph that doesn't obey the up-down self-energy graph rule. Here we denote a G-line, which originated from vertex "a" and points to vertex "b", as (a, b). The self-energy graph shown here contains an internal G-line loop, denoted as $\lambda = 1$, including vertex "2", "3", "5" and "4", and G-line (2,3), (3,5), (5,3) and (4,2). If the base loop is assigned with an upward spin, then the G-lines in loop $\lambda = 1$ should be assigned with a downward spin. Albeit, since the vertex "3" and "4" are connected by a V-line, thus G-line (2,3) and (5,4) must be assigned with spin variable with different directions. The up-down rule is thus violated in this irreducible third-order self-energy graph.

with

$$v^{(\lambda)}_{M_\lambda+1} = v^{(\lambda)}_1 \tag{3.24}$$

In graphical terms, these M_λ vertices are connected by G-lines which indeed form a closed loop.

Also we assign a spin variable σ_0 to the graph's "base loop", defined as *that* sequence of (M_0+1) vertices $v^{(0)}_1$, ..., $v^0_{M_0+1}$ for which Equation (3.23) holds but with

$$v^{(0)} \equiv 0 \quad \text{and} \quad v^{(0)}_{M_0+1} = 2n+1 \tag{3.25}$$

i.e., in graphical terms the G-lines connecting these "base loop" vertices form a contiguous line from the graph's entrance vertex $v = 0$ to the exit vertex $v = 2n+1$. Note that every vertex $v = 0$, ..., $2n+1$ is a member of one unique loop $\lambda \in \{0, \cdots, \Lambda_{n,g}\}$, denoted by λ_v below.

A graph g, so labeled with loop spin variables, σ_λ $(\lambda = 0, \cdots, \Lambda_{n,g})$, is said to "obey the up-down rule", if a set of values of either $\sigma_\lambda = \uparrow$ or $\sigma_\lambda = \downarrow$ can be chosen for each loop spin, such that the two end-point vertices v and $v' = v+1$ of every interaction line (with v odd) belong to different loops, with opposite loop spin, i.e,

$$\sigma_{\lambda_{v'}} \neq \sigma_{\lambda_v} \quad \text{for all odd } v,\ v' = v+1 \tag{3.26}$$

The subset of nth order irreducible graphs $g \in \mathcal{G}_n$, which obey the up-down rule is denoted by $\mathcal{G}^{\uparrow\downarrow}_n$ in the following.

We call the self-energy Feynman diagrams that conform to the up-down rule the *up-down self-energy diagrams*. In the first order self-energy diagrams (Figure 3.1A), only the Hartree diagram obeys the up-down rule. Figure 3.3(A), (B), (C) and (D) show all the first, second, third and fourth order up-down self-energy diagrams.

For the Hubbard model, we can either use the unrestricted self-energy diagram sum Equation (3.22) to calculate the self-energy, or use an equivalent up-down self-energy diagram sum. The difference is that in the unrestricted self-energy diagram sum, each closed loop

sum contributes a factor (-2), whereas each closed loop in an up-down self-energy diagram contributes (-1). Hence, for the Hubbard model, where $V(q) \equiv U$, Equation 3.22 can be written as an up-down diagram sum like this:

$$\begin{aligned}\Sigma(\vec{k}, i\nu_m) &= \lim_{n_{max}\to\infty} \lim_{\tau\to 0^+} \sum_{n=1}^{n_{max}} \sum_{g\in\mathcal{G}_n^{\uparrow\downarrow}} (-\frac{T}{N})^n \cdot (-1)^{\Lambda_{n,g}} \sum_{k_1\cdots k_n\in\mathcal{K}} \exp(\delta_{n,1} i\nu_{m_1}\tau) \times \\ &\quad \prod_{i=1}^{n} G(k_i) \times \prod_{i=1}^{n-1} G(\bar{k}_j) \times U^n \end{aligned} \tag{3.27}$$

where $\mathcal{G}_n^{\uparrow\downarrow}$ is the set of nth order up-down self-energy graphs.

We have developed a simple graph analysis algorithm, to check graphs $g \in \mathcal{G}_n$ for up-down-rule compliance at any order n, and to tabulate $\mathcal{G}_n^{\uparrow\downarrow}$. The basic idea is to start by assigning, say, $\sigma_0 = \uparrow$ to the base loop then assign $\sigma_\lambda = \downarrow$ to all closed loops λ connected to the base loop by a V-line, and so on, until all loops have been assigned a σ_λ. If all loops λ can be assigned a σ_λ in this iterative manner without ever violating the up-down-rule, the graph g obeys the up-down-rule, i.e., $g \in \mathcal{G}_n^{\uparrow\downarrow}$; else $g \notin \mathcal{G}_n^{\uparrow\downarrow}$.

3.5 Finite Order Truncation and Matsubara Frequency Cut-off

A finite order truncation must be made for calculating the self-energy of the Hubbard model numerically. Hence in the numerical implementation, Equation (3.22) is altered to be

$$\begin{aligned}\Sigma(\vec{k}, i\nu_m) &= \sum_{n=1}^{n_{max}} \sum_{g\in\mathcal{G}_n} (-\frac{T}{N})^n \cdot (-2)^{\Lambda_{n,g}} \lim_{\tau\to 0^+} \sum_{k_1\cdots k_n\in\mathcal{K}} \exp(\delta_{n,1} i\nu_m^{(1)}\tau) \times \\ &\quad \prod_{i=1}^{n} G(k_i) \times \prod_{i=1}^{n-1} G(\bar{k}_j) \times \prod_{l=1}^{n} V(q_l) \end{aligned} \tag{3.28}$$

and Equation (3.27) for the pure Hubbard model is modified as

$$\begin{aligned}\Sigma(\vec{k}, i\nu_m) &= \sum_{n=1}^{n_{max}} \sum_{g\in\mathcal{G}_n^{\uparrow\downarrow}} (-\frac{T}{N})^n \cdot (-1)^{\Lambda_{n,g}} \lim_{\tau\to 0^+} \sum_{k_1\cdots k_n\in\mathcal{K}} \exp(\delta_{n,1} i\nu_m\tau) \times \\ &\quad \prod_{i=1}^{n} G(k_i) \times \prod_{i=1}^{n-1} G(\bar{k}_j) \times U^n. \end{aligned} \tag{3.29}$$

The resulting approximation is a "conserving approximation" in the sense of Baym and Kadanoff [41]. It allows for a consistent construction of a 2-particle Green's function

which does not violate any of the fundamental symmetries of the underlying Hamiltonian, as explained further in Section 3.12.

Equation (3.28) or Equation (3.29) combined with the Dyson equation (Equation 3.12) constitute the fundamental self-consistent coupled equations for $\Sigma(k)$ and $G(k)$, which we want to solve. Note that Equation (3.28) or Equation (3.29) allows us to calculate $\Sigma(k)$, given $G(k)$, whereas the Dyson Equation (3.12) allows us to calculate $G(k)$, given $\Sigma(k)$. This suggests an obvious iterative solution procedure which will be described in the next section of this chapter.

A number of investigations have been done on the higher order perturbation expansion with self-energy diagrams. Zlatić worked up to the third order self-energy diagrams for the two-dimensional Hubbard model [46]. There are twelve topogically different proper self-energy diagrams of the fourth order, which can be grouped into four sets, within which all three diagrams give the same contribution at particle-hole symmetry. These fourth-order diagrams were first used by Yamada and Yosida [47] to study the symmetric Anderson impurity model [48]. Freericks and Jarrell [49] used them for the attractive Hubbard model ($U < 0$) at finite-temperature, and Gebhard *et al* studied the infinite dimensional Hubbard model with a half-filled band up to fourth order by the diagrammatic approximation as well [50] .

Since the number of Matsubara frequencies ν_m is also infinite in Equation (3.28) and Equation (3.29), a proper cut-off on the Matsubara frequencies is required to make the numerical calculation feasible. For order $n \geq 2$, the summation over Matsubara frequencies converges absolutely, and a simple numerical summation can be performed up to a maximum frequency ν_{max}, i.e, over all $i\nu_m$ with $|\nu_m| \leq \nu_{max}$. This so-called Matsubara cut-off must be chosen large enough so that the results are independent of ν_{max} to within the desired numerical accuracy. Typically, for the physically relevant parameter regime studied here, one can use

$$\nu_{max} \quad > \quad \alpha \times W$$

where W is the bandwidth described in Equation (2.17) and α is some constant factor of order 2 to 8. In the calculation presented in Chapter 4, we used $\alpha = 8$ to achieve a numerical accuracy of the Matsubara frequency sums of 99.5% or better. To avoid violations of any fundamental symmetries, the Matsubara cut-off is actually enforced by setting:

$$G(\vec{k}, i\nu_m) = \begin{cases} 0 & \text{if } |\nu_m| > \nu_{max} \\ (i\nu_m - \epsilon_{\vec{k}} + \mu - \Sigma(\vec{k}, i\nu_m))^{-1} & \text{otherwise} \end{cases}$$

in the numerical summation of Equation (3.28) or Equation (3.29).

For the first order contribution, $n = 1$, in Equation (3.28) or Equation (3.29), the foregoing Matsubara cut-off scheme cannot be used, because the $i\nu_m$-summation is only conditionally convergent. The summation must first be carried out to infinite $|i\nu_m|$, with a convergence factor $\exp(i\nu_m\tau)$ and $\tau > 0$, and *then* the limit $\tau \to 0^+$ must be taken. This requires some special numerical summation methods which will now be described. From Equation (3.28), the first-order contribution, $\Sigma^{(1)}(k) \equiv \Sigma^{(1)}(\vec{k})$, is independent of Matsubara frequency $i\nu_m$ for $k \equiv (\vec{k}, i\nu_m)$ and given by

$$\Sigma^{(1)}(\vec{k}) \;=\; \lim_{\tau\to 0^+} \sum_{g\in\mathcal{G}_1} (-\frac{T}{N})(-2)^{\Lambda_{1,g}} \sum_{k_1} \exp(i\nu_{m_1}\tau) G(k_1) V(q_1). \tag{3.30}$$

According to the definition of the Fourier transformation of Green's functions between the imaginary time and Matsubara frequency domains, Equation (3.3), the Matsubara frequency sum in Equation (3.30) is related to the Green's function in the imaginary time domain, namely

$$\lim_{\tau\to 0^+} T \sum_{i\nu_{m_1}\in\mathcal{M}_-} \exp(i\nu_m\tau) G(\vec{k}_1, i\nu_{m_1}) \;=\; \lim_{\tau\to 0^+} G(\vec{k}, -\tau). \tag{3.31}$$

The $i\nu_m$ sum is conditionally convergent because

$$G(k) = \frac{1}{i\nu_m} + \mathcal{O}(\frac{1}{i\nu_m})^2 \quad \text{for } |i\nu_m| \to \infty \tag{3.32}$$

due to the jump discontinuity of $G(\vec{k}, \tau)$ at $\tau = 0$:

$$G(\vec{k}, \tau \to 0^+) - G(\vec{k}, \tau \to 0^-) = -\langle [d_{\vec{k}\sigma} d\vec{k}\sigma^+ + d^+_{\vec{k}\sigma} d_{\vec{k}\sigma}]_+ \rangle = -1.$$

In order to calculate this $i\nu_m$ sum, we choose a "reference" Green's function

$$G_R(k) := \frac{1}{i\nu_m - E_{\vec{k}}} \tag{3.33}$$

where

$$E_{\vec{k}} := \lim_{i\nu_m \to \infty} (\epsilon_{\vec{k}} - \mu + \Sigma(\vec{k}, i\nu_m)) = \epsilon_{\vec{k}} - \mu + \Sigma^{(1)}(\vec{k}). \tag{3.34}$$

$G_R(k)$ cancels the $1/i\nu_m$-tail of $G(k)$, that is the difference, $\Delta G(k)$, between $G(k)$ and $G_R(k)$,

$$\Delta G(k) := G(k) - G_R(k) = \mathcal{O}(\frac{1}{i\nu_m})^3 \quad \text{for } |i\nu_m| \to \infty, \tag{3.35}$$

and we can carry out the $i\nu_m$-sum over $\Delta G(k)$ with a finite cut-off ν_{max} and with τ set to $\tau = 0$. We can also carry out the $i\nu_m$-sum over the reference Green's function $G_R(k)$ analytically by contour integral method, taking $\nu_{max} \to \infty$ and then $\tau \to 0^+$, i.e.,

$$\begin{aligned} \lim_{\tau \to 0^+} G(\vec{k}, -\tau) &= \lim_{\tau \to 0^+} \Delta G(\vec{k}, -\tau) + \lim_{\tau \to 0^+} G_R(\vec{k}, \tau) \\ &\cong T \sum_{\substack{i\nu_m \\ |\nu_m| \le \nu_{max}}} \Delta G(\vec{k}, i\nu_m) + \frac{1}{e^{E_{\vec{k}}/T} + 1}. \end{aligned} \tag{3.36}$$

This result is then used to evaluate $\Sigma^{(1)}(\vec{k})$ according to Equation (3.30).

3.6 Iterative Self-consistency Algorithm

The implementation of the self-consistency iteration starts from an initial guess for the self-energy denoted by $\tilde{\Sigma}^{(0)}(k)$. Normally, one would set $\tilde{\Sigma}^{(0)}(k) \equiv 0$ unless a better initial guess is known, for example from a previous calculation of $\Sigma(k)$ with slightly different parameters, such as temperature. Successive iterative approximations to $G(k)$ and $\Sigma(k)$ could be calculated by

$$\begin{cases} G^{(p)}(k) &= [i\nu_m - \epsilon_{\vec{k}} + \mu - \tilde{\Sigma}^{(p-1)}(k)]^{-1} \\ \tilde{\Sigma}^{(p)}(k) &= \Sigma([G^{(p)}], k) \end{cases}$$

where $p = 1, 2, \cdots, I$ is the iteration number and I is the maximum number of iterations. Here $\Sigma([G^{(p)}], k)$ denotes the self-energy treated as a *functional* of an arbitrary complex-valued function $G^{(p)}(k')$ defined on the domain $\mathcal{K} \ni k'$. That is, $\Sigma([G^{(p)}], k)$ is the right-hand

side expression of Equation (3.28) or Equation (3.29), respectively, with the internal Green's function factors $G(k_j)$ and $G(\bar{k}_j)$ replaced by any $G^{(p)}(k_j)$ and $G^{(p)}(\bar{k}_j)$, respectively. If, after p iterations, with $p \leq I$, $G^{(p)}(k)$ is "sufficiently close" to $G^{(p-1)}(k)$ and $\Sigma([G^{(p)}], k)$ is "sufficiently close" to $\Sigma([G^{(p-1)}], k)$, then the iteration has converged, and we accept $G^{(p)}(k)$ and $\tilde{\Sigma}^{(p)}(k)$ as the solutions for the Green's function $G(k)$ and the self-energy $\Sigma(k)$. The precise meaning of "sufficiently close", i.e., our convergence criterion, will be described later on in Appendix C.3.

However, it frequently happens that the foregoing simple iteration scheme runs into a limit-cycle, i.e., it never converges. Rather, in successive iteration steps p, $\tilde{\Sigma}^{(p)}(k)$ and $\tilde{G}^{(p)}(k)$ oscillate back and forth between, say, two different limiting values, no matter how large p is. This problem can often be avoided by using a so-called feedback iteration method, which damps out such limit-cycle oscillations. The feedback method is described by the following iteration scheme, for $p = 1, 2, \cdots, I$:

$$\begin{cases} G^{(p)}(k) &= [i\nu_m - \epsilon_{\vec{k}} + \mu - \tilde{\Sigma}^{(p)}(k)]^{-1} \\ \tilde{\Sigma}^{(p)}(k) &= (1-f)\Sigma([G^{(p)}], k) + f\tilde{\Sigma}^{(p-1)}(k) \end{cases} \tag{3.37}$$

where, the feedback parameter f is usually chosen in the range $0 < f < 1$.

The procedure to calculate the self-energy with the self-consistent algorithm is then summarized by

1. input $\tilde{\Sigma}^{(0)}(k)$ as initialization; $\tilde{\Sigma}^{(0)}(k)$ can be set as zero unless a better initial guess is available;

2. start self-consisent iteration loop with iteration number $p = 1$;

3. (in loop) calculate the next Green's function approximant $G^{(p)}(k)$ from the latest self-energy approximate $\tilde{\Sigma}^{(p-1)}(k)$ using the Dyson equation (Equation 3.12);

4. (in loop) calculate the self-energy functional $\Sigma([G^{(p)}], k)$ for the latest Green's function approximant, $G^{(p)}(k)$, using self-energy diagram expansion Equation (3.28) or Equation (3.29);

5. (in loop) compute the "self-consistency iteration difference" (as defined in Equation (C.5) and Equation (C.6) in Appendix C.3), to determine whether the self-consistency iteration has converged or not. If it is converged, then stop the the self-consistency iteration, and use $\Sigma([G^{(p)}], k)$ as the self-energy solution $\Sigma(k)$ and exit; else goto Step 6;

6. (in loop) calculate self-energy $\tilde{\Sigma}^{(p)}(k)$ from $\tilde{\Sigma}^{(p-1)}(k)$ and $\Sigma([G^{(p)}])(k)$ according to Equation 3.37, advance the iteration number p by $+1$, and goto Step 3.

This algorithm can be directly implemented is this form if the diagram summation $\Sigma([G^{(p)}], k)$ can be done, exactly by brute force summation over all orders $n \leq n_{max}$, $g \in \mathcal{G}_n$ or $\mathcal{G}_n^{\uparrow\downarrow}$ and all $(k_1, \cdots, k_n)$, see Equation (3.28) or (3.29). However, if the higher order ($n \geq 2$) diagrams are evaluated by Monte Carlo sampling techniques, additional modifications are necessary to deal with the Monte Carlo errors. This will be described in the next section.

3.7 Monte Carlo Summation Technique

According to Section 3.5, to evaluate the first order diagrams, $\Sigma^{(1)}(k)$, the computation effort is linear in the total number of all individual $k \equiv (\vec{k}, i\nu_m)$. And thus we can always sum over k for $\Sigma^{(1)}(k)$ by brute force. The sum of all higher order ($n \geq 2$) contributions, denoted as $\Sigma_>(k)$, and defined as

$$\Sigma_>(k) = \Sigma(k) - \Sigma^{(1)}(k), \tag{3.38}$$

requires summations over very large, high-dimensional (k_j-) domains. Therefore we use a Monte Carlo summation technique to calculate the higher-order contributions, $\Sigma_>(k)$, to the self-energy $\Sigma(k)$.

The basic idea for Monte Carlo summation is quite straightfoward. Suppose that we need to calculate Y as the sum of function $F(x)$ over some discrete summation domain $\mathcal{S}$ of N_s distinct objects $x \in \mathcal{S}$. By choosing an appropriate weight function $W(x)$, we can write this

as

$$\begin{aligned} Y &= \sum_{x\in\mathcal{S}} F(x) \\ &= \Omega \sum_{x\in\mathcal{S}} S(x)\cdot P(x) \end{aligned} \tag{3.39}$$

where Ω, the score function $S(x)$ and the probability distribution $P(x)$ are defined as

$$\Omega = \sum_{x\in\mathcal{S}} W(x) \tag{3.40}$$

$$S(x) = \frac{F(x)}{W(x)} \tag{3.41}$$

$$P(x) = \frac{W(x)}{\Omega} \tag{3.42}$$

respectively. The weight function $W(x)$ must obey

$$W(x) > 0 \quad \text{if } F(x) \neq 0 \tag{3.43}$$

$$W(x) \geq 0 \quad \text{for all } x \in \mathcal{S} \tag{3.44}$$

and the sum of weight function over domain $\mathcal{S}$ must be finite. Otherwise, the choice of $W(x)$ is arbitrary. One can show that the Monte Carlo statistical sampling error is minimized by choosing

$$W(x) = \text{constant} \times |F(x)|$$

However, for reasons explained later, we will use a different choice for $W(x)$ for our diagram summation problem.

Note that Y can therefore be thought of as the statistical mean of $\Omega \cdot S(x)$, averaged with the probability distribution $P(x)$. Therefore, by the central limit theorem, if enough random sample points $x^{(m)}$ from $\mathcal{S}$ are chosen, distributed according to $P(x)$, then

$$Y \cong \frac{\Omega}{M} \sum_{m=1}^{M} S(x^{(m)})$$

where $[x^{(m)}]$ $(m = 1, \cdots, M)$ is a random sample drawn from the summation domain $\mathcal{S}$ according to the probability $P(x)$ and M is the size of that sample. The index m used here

to label the Monte Carlo sample point $x^{(m)}$ is not to be confused with integer index m for the Matsubara frequency defined in Equation (3.6).

3.8 Calculation of Self-Energy By Monte Carlo Summation

The foregoing Monte Carlo summation technique is applied to the calculation of the high order ($n \geq 2$) self-energy contribution, $\Sigma_>(k)$, as defined in Equation (3.38). According to Equation(3.22) for the extended Hubbard model,

$$\Sigma_>(k) \;=\; \sum_{n=2}^{n_{max}} \Sigma^{(n)}(k) \tag{3.45}$$

where, $\Sigma^{(n)}(k)$ is given by

$$\Sigma^{(n)}(k) \;=\; \sum_{k_1 \cdots k_n \in \mathcal{K}} F(k; k_1, \cdots, k_n, n, g) \tag{3.46}$$

and

$$F(k; k_1, \cdots, k_n, n, g) \;=\; \sum_{g \in \mathcal{G}_n} (-\frac{T}{N})^n (-2)^{\Lambda_{n,g}} \prod_{j=1}^{n} G(k_j) \prod_{j=1}^{n-1} G(\bar{k}_j) \prod_{\ell=1}^{n} V(q_\ell) \tag{3.47}$$

where $k \equiv (\vec{k}, i\nu_m)$ is the momentum-Matsubara-frequency vector assigned to external G-lines.

We will perform a separate Monte Carlo summation for the self-energy contribution, $\Sigma^{(n)}(k)$ at each order n ($2 \leq n \leq n_{max}$). The summation domain $\mathcal{S}$ and the summation objects x for calculating $\Sigma^{(n)}(k)$ are given by

$$\mathcal{S}^{(n)} \;=\; \{x = (k_1, \cdots, k_n) \mid k_1 \in \mathcal{K}, \cdots, k_n \in \mathcal{K}\},$$

where $\mathcal{K}$ is defined in Equation (3.7), and the weight function $W^{(n)}(k_1, \cdots, k_n)$ for $\Sigma^{(n)}(k)$ is then chosen as

$$W^{(n)}(k_1, \cdots, k_n) \;=\; \prod_{j=1}^{n} |G(k_j)|. \tag{3.48}$$

The score function $S^{(n)}(k; k_1, \cdots, k_n)$ for $\Sigma^{(n)}(k)$ is then

$$S^{(n)}(k; k_1, \cdots, k_n) \;=\; \sum_{g \in \mathcal{G}_n} \frac{F(k; k_1, \cdots, k_n, n, g)}{\prod_j^n |G(k_j)|} \tag{3.49}$$

Note that the sum over diagram topologies $g \in \mathcal{G}_n$ is carried out by brute force in evaluating $S^{(n)}$, not by Monte Carlo, in order to reduce the statistical errors. Note also that the score function depends on the momentum-Matsubara-frequency k associated with the external G-line. For each order n, $\Sigma^{(n)}(\vec{k}, i\nu_m)$ can be calculated as

$$\begin{aligned} \Sigma^{(n)}(\vec{k}, i\nu_m) &= \sum_{k_1 \in \mathcal{K}} \cdots \sum_{k_n \in \mathcal{K}} S(k; k_1, \cdots, k_n) \prod_{j=1}^{n} |G(k_j)| \\ &\approx \frac{\Omega^{(n)}}{M} \sum_{m=1}^{M} S(k; k_1^{(m)}, \cdots, k_n^{(m)}) \end{aligned} \tag{3.50}$$

where

$$\Omega^{(n)} := \sum_{k_1 \in \mathcal{K}} \cdots \sum_{k_n \in \mathcal{K}} W^{(n)}(k_1, \cdots, k_n) = (\sum_{k \in \mathcal{K}} |G(k)|)^n = (\Omega^{(1)})^n \tag{3.51}$$

and M is the Monte-Carlo sample size of configurations $x^{(m)} \equiv (k_1^{(m)}, \cdots, k_n^{(m)})$ that have been generated according to probability

$$P^{(n)}(k_1, \cdots, k_n) = \frac{W^{(n)}(k_1, \cdots, k_n)}{\Omega^{(n)}}. \tag{3.52}$$

Perfect sampling [51] is a Monte Carlo sampling algorithm that produces, in a finite number of calculation steps, sample points $x^{(m)}$, which are statistically independent of each other and distributed *exactly* according to the desired "target" probability $P(x)$. Our probability functions $P^{(n)}(k_1, \cdots, k_n)$ from Equation (3.52) and (3.48) have the advantage that they allow for a very efficient (and trivial) perfect sampling Monte Carlo algorithm. Since Equation (3.52) can be also written as

$$P^{(n)}(k_1, \cdots, k_n) = \prod_{j=1}^{n} P^{(1)}(k_j), \tag{3.53}$$

and k_j $(j = 1, \cdots, n)$ and $k_{j'}$ $(j' = 1, \cdots, n)$ are statistically independent for $j \neq j'$, we can draw the sample of each k_j, statistically independently, from the distribution $P^{(1)}(k_j)$, defined as

$$P^{(1)}(k_j) = \frac{|G(k_j)|}{\Omega^{(1)}} \tag{3.54}$$

Therefore, a perfect sampling for the n-vector variable $(k_1, \cdots, k_n)$ can be achieved as follows:

1. Introduce a one-to-one integer labeling of all elements of $\mathcal{K}$, denoted with a single integer κ, $\tilde{k}(\kappa) \in \mathcal{K}$, so that

$$\tilde{k}(\kappa) \neq \tilde{k}(\kappa') \quad \text{if } \kappa \neq \kappa' \tag{3.55}$$

and the index κ ranges from 1 to K, where K is the total number of elements in set $\mathcal{K}$, which is finite due to the cut-off $|i\nu_m| \leq \nu_{max}$ of the Matsubara frequency;

2. Define

$$Q(\kappa) := \sum_{\kappa'=1}^{\kappa} |G(\tilde{k}(\kappa'))| \tag{3.56}$$

for $\kappa = 0, \cdots, K$. Thus, at the boundaries, $\kappa = 0$ and $\kappa = K$, respectively:

$$Q(0) = 0 \tag{3.57}$$

$$Q(K) = \sum_{k \in \mathcal{K}} |G(k)| = \Omega^{(1)} \tag{3.58}$$

3. To draw n independent k_j-sample points $k_1, \cdots, k_n$, generate n independent uniform random numbers u_j $(j = 1, \cdots, n)$, with $u_j \in (0, 1]$, uniformly distributed over $(0, 1]$ (i.e., $0 < u_j \leq 1$). Find *that* $\kappa_j \in \{1, \cdots, K\}$ for each $j = \{1, \cdots, n\}$ for which

$$Q(\kappa_j - 1) < u_j \times \Omega^{(1)} \leq Q(\kappa_j). \tag{3.59}$$

Then choose $(k_1, \cdots, k_n) = (\tilde{k}(\kappa_1), \cdots, \tilde{k}(\kappa_n))$.

Note that the weight sums $Q(\kappa)$ divide the interval $(0, \Omega^{(1)}]$ into K subintervals $(Q(\kappa - 1), Q(\kappa)]$ (for $\kappa = 1, \cdots, K$) and the probability that $u\Omega^{(1)}$ falls into $(Q(\kappa - 1), Q(\kappa)]$, for a uniformly random $u \in (0, 1]$, is exactly equal to $P^{(1)}(\tilde{k}(\kappa))$. Therefore each random k_j drawn in this manner is distributed according to $P^{(1)}(k_j)$, and is statistically independent of any other $k_{j'}$ $(j \neq j')$ or any previously drawn $k_{j'}$, if the random numbers u_j are generated statistically independently. Therefore each sample point $(k_1^{(m)}, \cdots, k_n^{(m)})$ with $m = 1 \cdots M$ generated like this is distributed according to $P^{(n)}(k_1, \cdots, k_n)$, and the sample points $(k_1^{(m)}, \cdots, k_n^{(m)})$ will be statistically independent.

The perfect sampling algorithm can be straightforwardly parallelized simply by distributing the sample generation and score evaluation over multiple processors. The great advantage of perfect sampling compared to the conventional Markov chain sampling [52] is that each new sample configuration $(k_1^{(m)}, \cdots, k_n^{(m)})$ is statistically completely independent of any previously generated sample configuration. The sample configurations can therefore be generated in a completely independent manner, in parallel, on multiple processors, with linear speedup.

In order to estimate the Monte Carlo statistical error, R repetitions of independent Monte Carlo estimations are performed in every self-consistency iteration step. The detailed calculation of $G(k)$ and $\Sigma(k)$ procedure in each self-consistent iteration step, say the p-th iteration, is described below. Here we will use $\tilde{\Sigma}_r^{(p)}(k)$ to denote the r-th repetition of the estimation of self-energy in p-th self-consistency iteration, and use $\tilde{\Sigma}_r^{(n,p)}(k)$ to denote the r-th repetition of the estimation of nth-order contribution of self-energy in the p-th self-consistency iteration.

1. Set $\tilde{\Sigma}_r^{(p)}(k) \equiv 0$ for $p = 0$, unless a better initial guess for $\tilde{\Sigma}_r^{(0)}(k)$ is available.

2. Start loop with iteration number $p = 1$.

3. Given R independent Monte Carlo estimations of self-energy $\Sigma(k)$, denoted as $\tilde{\Sigma}_r^{(p-1)}(k)$ $(r = 1, \cdots, R)$ from last self-consistency iteration step if $p \geq 2$, or the guessed initial value $\tilde{\Sigma}_r^{(0)}(k)$, if $p = 1$: use these $\tilde{\Sigma}_r^{(p-1)}(k)$ to calculate R independent estimations of $\tilde{G}_r^{(p)}(k)$ by

$$\tilde{G}_r^{(p)}(k) = [i\nu_m - \epsilon_{\vec{k}} + \mu - \tilde{\Sigma}_r^{[p-1]}(k)]^{-1}. \tag{3.60}$$

4. Calculate the average of these R estimations $\tilde{G}_r^{(p)}(k)$ for $G(k)$ as

$$\bar{G}^{(p)}(k) = \frac{1}{R} \sum_{r=1}^{R} \tilde{G}_r^{(p)}(k). \tag{3.61}$$

For all n from 2 to n_{max}, use this $\bar{G}^{(p)}(k)$ to construct the Monte Carlo weight functions $W^{(n,p)}(k_1, \cdots, k_n)$ at orders $n = 1, \cdots, n_{max}$, given by

$$W^{(n,p)}(k_1, \cdots, k_n) = \prod_{j=1}^{n} |\bar{G}^{(p)}(k_j)| \quad \text{for all } r = 1, \cdots, R. \tag{3.62}$$

5. Do R independent Monte Carlo simulations at each order n ($n = 2, \cdots, n_{max}$) to calculate $\tilde{\Sigma}_r^{(n,p)}(k)$ from $\tilde{G}_r^{(p)}(k)$ for the present self-consistency iteration step, using $W^{(n,p)}(k_1, \cdots, k_n)$ as the Monte Carlo weight function as described in Section 3.7 and earlier part of this section. Also calculate $\tilde{\Sigma}^{(1,p)}(k)$ by brute force summation from $\bar{G}(k)$ as described in Section 3.5 (notice there is no subscription r here since the first-order contribution is calculated directly from the averaged Green's function).

6. Calculate the next sample of R new diagram estimates for the self-energy by summing $\tilde{\Sigma}^{(1,p)}(k)$ and $\tilde{\Sigma}_r^{(n,p)}(k)$ to get

$$\hat{\Sigma}_r^{(p)}(k) = \tilde{\Sigma}^{(1,p)}(k) + \sum_{n=2}^{n_{max}} \tilde{\Sigma}_r^{(n,p)}(k). \tag{3.63}$$

7. Calculate the average over the samples of the R self-energy estimates, i.e.,

$$\bar{\Sigma}^{(p)}(k) = \frac{1}{R} \sum_{r=1}^{R} \hat{\Sigma}_r^{(p)}(k). \tag{3.64}$$

8. Calculate the Monte Carlo error of the samples of R self-energy estimates, for both $\hat{\Sigma}_r^{(p)}(k)$ and for $\tilde{\Sigma}_r^{(n,p)}(k)$ with $n = 2, \cdots, n_{max}$, by Equation (C.4) described in Appendix C.2, and use $\bar{\Sigma}^{(p)}(k)$ to check the convergence difference between $\bar{\Sigma}^{(p)}(k)$ and the self-energy $\bar{\Sigma}^{(p-1)}(k)$ calculated in last self-consistency iteration step. If the convergence criterion is met, accept $\bar{\Sigma}^{(p)}(k)$ as the self-energy solution $\Sigma(k)$ and stop the iteration; Else, use the feedback Equation (3.37) to generate the R samples of self-energy estimations,

$$\tilde{\Sigma}_r^{(p)}(k) = (1 - f)\hat{\Sigma}_r^{(p)}(k) + f\tilde{\Sigma}_r^{(p-1)}(k), \tag{3.65}$$

for the next iteration. Advance the iteration number p by +1 and go to Step 3.

3.9 Spectral Function of Single-Particle Green's Function

The spectral weight function $A(\vec{k},\omega)$ can be observed by angle-resolved photoemission (ARPES) [53], the angle-resolved inverse photoemission and tunneling experiments [54], so that the theoretical calculation can be compared with the experimental data.

The Green's function in the Matsubara frequency domain $G(\vec{k},i\nu_m)$, as well as the self-energy $\Sigma(k)$ can be analytically continued into the complex plane

$$i\nu_m \rightarrow z = \omega \pm i\eta$$

with real ω and with $\eta > 0$, i.e., excluding the real axis, leading to the complex frequency Green's function $G(\vec{k},z)$. The analytical continuation allows the Green's function in the Matsubara frequency domain to be related to that in the real frequency domain [37]. The real-frequency (ω) behavior of $G(\vec{k},z)$ can be expressed in terms of a real-valued function of the real frequency.

$$G''(\vec{k},\omega) \;=\; \lim_{\eta\rightarrow 0}\frac{1}{2i}[G(\vec{k},\omega-i\eta)-G(\vec{k},\omega+i\eta)] \tag{3.66}$$

The function $G''(\vec{k},\omega)$ is sometimes referred to as the *absorptive part* of the Green's function. The inverse of this relationship can be represented in the integral form with

$$G(\vec{k},z) \;=\; \int_{-\infty}^{\infty}\frac{d\omega}{\pi}\frac{G''(\vec{k},\omega)}{z-\omega} \tag{3.67}$$

It is customary to express G'' and G in terms of the spectral function $A(\vec{k},\omega)$ defined as

$$A(\vec{k},\omega) \;:=\; \frac{G''(\vec{k},\omega)}{\pi} \tag{3.68}$$

Therefore, $G(\vec{k},i\nu_m)$ is related to $A(\vec{k},\omega)$ by

$$G(\vec{k},i\nu_m) = \int_{-\infty}^{\infty} d\omega \frac{A(\vec{k},\omega)}{i\nu_m-\omega} \tag{3.69}$$

The integral moments of the spectral function are given by

$$\mu_m \;:=\; \int_{-\infty}^{\infty} d\omega\omega^m A(\vec{k},\omega) \tag{3.70}$$

The zeroth order integral moment μ_0 is exactly equal to zero, i.e.,

$$\mu_0 = 0 \tag{3.71}$$

which is general to all single band models. For the pure Hubbard model, the first- and second-order integral moments, μ_1 and μ_2 respectively, are known to obey [3]

$$\mu_1 = \epsilon_{\vec{k}} - \mu + \langle\hat{n}\rangle/2 \tag{3.72}$$

$$\mu_2 = (\epsilon_{\vec{k}} - \mu)^2 + U \times (\epsilon_{\vec{k}} - \mu) + \frac{1}{2}U^2\langle\hat{n}\rangle. \tag{3.73}$$

The simplest way to calculate $G''(\vec{k},\omega)$ or $A(\vec{k},\omega)$ from $G(\vec{k},i\nu_m)$ is to analytically continue $G(\vec{k},i\nu_m)$ to $G(\vec{k},z)$ and insert it into Equation (3.66) to obtain $G''(\vec{k},\omega)$. But this method is not applicable to the situation where $G(\vec{k},i\nu_m)$ is computed by a numerical method, and thus an analytical formula for $G(\vec{k},z)$ doesn't exist. Therefore, an integral equation solver algorithm for Equation (3.69) is required. But due to the incompleteness and noise of the Green's function, $G(k)$, data in the numerical solution, the standard integral equation solution method meets great difficulties due to numerical instability. The most widely used technique to solve this problem is the maximum entropy method (MEM) [55], which selects the most likely candidate solution for $A(\vec{k},\omega)$ that is consistent with the input $G(\vec{k},i\nu_m)$ data. The spectral weight function is treated as a probability function with an entropy function $S[A]$. The "best" solution is then that spectral weight $A(\vec{k},\omega)$ which maximizes $S[A]$. Appendix B.1 provides a more detailed introduction to the maximum entropy method.

The absorptive part $G''(\vec{k},\omega)$ of the Green's function can be related to a mathematically equivalent object, the reactive part $G'(\vec{k},\omega)$ of the Green's function, defined by

$$G'(\vec{k},\omega) = \frac{1}{2}[G(\vec{k},\omega + i0^+) + G(\vec{k},\omega - i0^-)].$$

According to the Kramers-Kronig relations [38],

$$G'(\omega) = \mathcal{P}\int \frac{d\tilde{\omega}}{\pi}\frac{G''(\vec{k},\tilde{\omega})}{\omega - \tilde{\omega}} \tag{3.74}$$

and

$$G''(\omega) = -\mathcal{P}\int \frac{d\tilde{\omega}}{\pi}\frac{G'(\vec{k},\tilde{\omega})}{\omega-\tilde{\omega}} \tag{3.75}$$

where $\mathcal{P}\int$ denotes the principle value integral.

Just like the Green's function, the higher order contribution to the self-energy, $\Sigma_>(\vec{k}, i\nu_m)$, can be analytically continued and expressed in terms of a reactive part $\Sigma'_>(\vec{k},\omega)$ and absorptive part $\Sigma''_>(\vec{k},\omega)$. The spectral function $\Sigma''_>(\vec{k},\omega)$ can be calculated from $G''(\vec{k},\omega)$ and $G'(\vec{k},\omega)$ as shown below. $\Sigma''_>(\vec{k},\omega)$ can also be calculated from $\Sigma(\vec{k}, i\nu_m)$ by the maximum entropy method. The first method is more reliable [56]. The analytically continued Green's function can be written as

$$\begin{aligned}\lim_{\eta\to 0} G(\vec{k},\omega+i\eta) &= G'(\vec{k},\omega)+iG''(\vec{k},\omega)\\ &= \frac{1}{(\omega+i0^+)-\epsilon_{\vec{k}}-\Sigma(\vec{k},\omega+i0^+)}.\end{aligned}$$

From Equation (3.12), the high-order partial self-energy $\Sigma_>(\vec{k}, i\nu_m)$ can be written as the function of of $E_{\vec{k}}$ and $G(\vec{k}, z)$.

$$\Sigma_>(\vec{k},z) = z - E_{\vec{k}} - \frac{1}{G(\vec{k},z)}$$

where

$$E_{\vec{k}} = \epsilon_{\vec{k}} - \mu + \Sigma^{(1)}(\vec{k}) \tag{3.76}$$

and the first order self-energy $\Sigma^{(1)}(\vec{k})$, Equation (3.30), is independent of Matsubara frequency.

So the real frequency self-energy $\Sigma(\vec{k},\omega+i0^+)$ can be calculated from G' and G'' as

$$\Sigma(\vec{k},\omega+i0^+) = \Sigma'_>(\vec{k},\omega)+\mathrm{i}\Sigma''_>(\vec{k},\omega)+\Sigma^{(1)}(\vec{k}) \tag{3.77}$$

$$\Sigma'_>(\vec{k},\omega) = \frac{G'(\vec{k},\omega)}{G'(\vec{k},\omega)^2+G''(\vec{k},\omega)^2}+\omega-E_{\vec{k}} \tag{3.78}$$

$$\Sigma''_>(\vec{k},\omega) = \frac{G'(\vec{k},\omega)}{G'(\vec{k},\omega)^2+G''(\vec{k},\omega)^2}, \tag{3.79}$$

after $G''(\vec{k},\omega) = \pi \cdot A(\vec{k},\omega)$ has been obtained by the maximum entropy method from $G(\vec{k},i\nu_m)$ via Equation (3.69) and $G'(\vec{k},\omega)$ has been calculated from $G''(\vec{k},\omega)$ by Equation (3.75).

The density of states (DOS) also provides important information about the excitation spectrum. It is defined as

$$D(\omega) = \frac{1}{N}\sum_{\vec{k}} A(\vec{k},\omega). \tag{3.80}$$

$D(\omega)$ can also be obtained from the imaginary frequency function $\tilde{D}(i\nu_m)$ defined as

$$\tilde{D}(\mathrm{i}\nu_m) = \frac{1}{N\cdot\pi}\sum_{\vec{k}} G(\vec{k},i\nu_m),$$

by analytical continuation $i\nu_m \to z = \omega + i\eta$, such that

$$D(\omega) = \frac{1}{2i}[\tilde{D}(\omega - i0^+) - \tilde{D}(\omega + i0^-)]. \tag{3.81}$$

For non-interacting electrons, the density states $D(\omega)$ is

$$D(\omega) = \frac{1}{N}\sum_{\vec{k}} \delta(\omega - \epsilon_{\vec{k}} + \mu) \equiv D^{(0)}(\omega - \mu). \tag{3.82}$$

The functions $-G''(\vec{k},\omega)$, $A(\vec{k},\omega)$, $D(\omega)$ and $-\Sigma''(\vec{k},\omega)$ are all positive semi-definite, i.e,

$$-G''(\vec{k},\omega) \geq 0, \quad -\Sigma''(\vec{k},\omega) \geq 0, \quad A(\vec{k},\omega) \geq 0$$
$$\text{and} \qquad D(\omega) \geq 0 \qquad \text{for all } \omega\ . \tag{3.83}$$

Both in the atomic limit ($t_{ij} = 0$) and in the non-interacting limit ($V_{ij} = 0$), the Hubbard model can be solved exactly as indicated in Chapter 2, and $A(\vec{k},\omega)$ can be calculated exactly in either limit.

The spectral weight function $A(\vec{k},\omega)$ of the Hubbard model at half-filing and $T \to 0$ in the atomic limit is composed of two equivalent delta functions located at $\omega_+ = U/2$ and $\omega_- = -U/2$, regardless the momentum $\vec{k}$, corresponding to the lower and upper Hubbard band excitations described in Chapter 2, i.e,

$$A(\vec{k},\omega) = \frac{1}{2}[\delta(\omega - \frac{U}{2}) + \delta(\omega + \frac{U}{2})], \tag{3.84}$$

indicating an energy excitation gap $\Delta = \omega_+ - \omega_- = U$, consistent with the properties of the Hubbard model in the atomic limit, discussed in Section 2.4.

If the Hubbard model is in the non-interacting limit, the spectral weight function $A(\vec{k}, \omega)$ is a single delta function localized at the band energy measured from the chemical potential μ, $\omega = E_{\vec{k}} = \epsilon_{\vec{k}} - \mu$, i.e,

$$A(\vec{k}, \omega) = \delta(\omega - \epsilon_{\vec{k}} + \mu). \tag{3.85}$$

In the particle-hole symmetry case, this is also true at $T > 0$, since $\mu = 0$ in temperature-independence. For $T \to 0$ and momenta $\vec{k}$ on the Fermi surface, the delta-function-peak of $A(\vec{k}, \omega)$ will be exactly at $\omega = 0$.

Figure 3.4 provides a conceptual view of $A(\vec{k}, \omega)$ for the Hubbard model in the atomic limit and non-interacting limit.

3.10 Self-energy and Green's Function of Particle-hole Symmetric Hubbard Model

When the Hubbard model is particle-hole symmetric as described in Section 2.2 and Appendix A, the self-energy $\Sigma(k)$, the Green's function $G(k)$ and the corresponding spectral function $A(\vec{k}, \omega)$ all obey additional symmetry relations due to the particle-hole symmetry, namely,

$$\mathrm{Re}\Sigma_>(\vec{k}, i\nu_m) = -\mathrm{Re}\Sigma_>(\vec{k} + \vec{K}, i\nu_m) \tag{3.86}$$

$$\mathrm{Im}\Sigma_>(\vec{k}, i\nu_m) = \mathrm{Im}\Sigma_>(\vec{k} + \vec{K}, i\nu_m) \tag{3.87}$$

for self-energy $\Sigma(k)$;

$$\mathrm{Re}G(\vec{k}, i\nu_m) = -\mathrm{Re}G(\vec{k} + \vec{K}, i\nu_m) \tag{3.88}$$

$$\mathrm{Im}G(\vec{k}, i\nu_m)) = \mathrm{Im}G(\vec{k} + \vec{K}, i\nu_m) \tag{3.89}$$

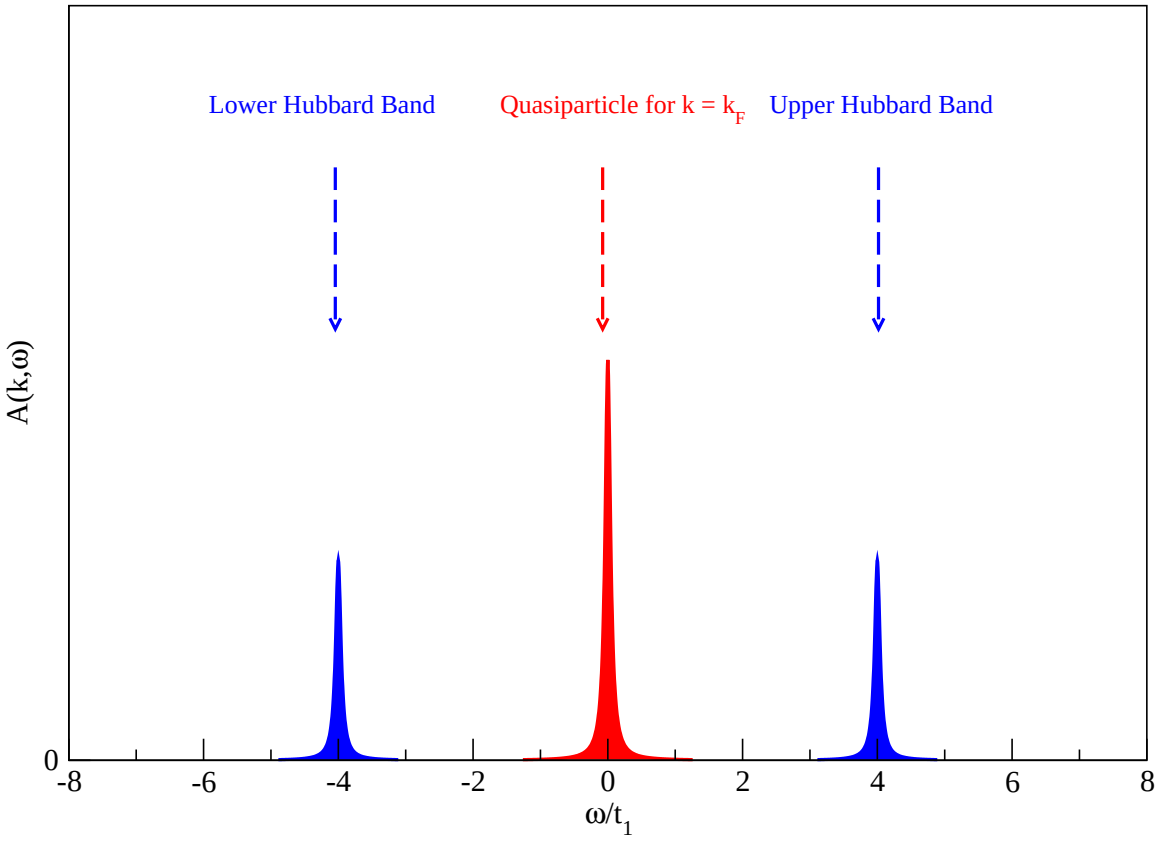

Figure 3.4: The spectral weight function $A(\vec{k},\omega)$ of the Hubbard model with on-site repulsion $U = 8t_1$, in the atomic limit and non-interacting limit, are illustrated in color blue and red, respectively. The spectral weight function $A(\vec{k},\omega)$ for the non-interacting limit is for the special case that $\vec{k}$ is on the Fermi surface ($\vec{k} = \vec{k}_F$). The spectral weight $A(\vec{k},\omega)$ in the atomic limit is the same for all $\vec{k}$ in the Brillouin zone.

for the Green's function $G(k)$, where $\vec{K}$ is a reciprocal lattice vector, i.e, $\vec{K} = (\pi, \pi)$. The corresponding spectral weight $A(\vec{k}, \omega)$ then thus holds the relation as

$$A(\vec{k}, \omega) = A(\vec{k} + \vec{K}, -\omega) \tag{3.90}$$

in the particle-hole symmetry.

As a consequence, for the momenta on the particle-hole symmetric Fermi surface (e.g. the diamond-shape $\vec{k}$-surface for Hubbard model of 2D square lattice shown in Figure (2.1)), denoted by $\vec{k}_F$,

$$\mathrm{Re}\Sigma_>(\vec{k}_F, i\nu_m) = \mathrm{Re}G(\vec{k}_F, i\nu_m) = 0 \tag{3.91}$$

and $A(\vec{k}_F, \omega)$ and $D(\omega)$ are symmetric to $\omega = 0$:

$$A(\vec{k}_F, -\omega) = A(\vec{k}_F, \omega) \quad , \quad D(-\omega) = D(\omega). \tag{3.92}$$

For the special case of the pure Hubbard model, the first order contribution $\Sigma^{(1)}(k)$ is exactly equal to the chemical potential μ, such that

$$\Sigma^{(1)}(k) = \mu = \frac{U}{2} \tag{3.93}$$

according to Equation (2.32). As a consequence, $\Sigma^{(1)}(k)$ exactly cancels the chemical potential μ in the so-called "first order quasi-particle energy" $E_{\vec{k}}$, i.e,

$$E_{\vec{k}} = \epsilon_{\vec{k}} \tag{3.94}$$

at particle-hole symmetry.

3.11 Spin Susceptibility

The spin susceptibility is essential to understand the magnetism of the extended or pure Hubbard model, especially its antiferromagnetic properties, by describing the correlation between the spin operators S_j^α which is defined in Equation (2.23), i.e.,

$$S_j^{(\alpha)} \quad = \quad \sum_{\sigma,\rho=\uparrow\downarrow} \frac{1}{2} \hat{\sigma}_{\sigma\rho}^{(\alpha)} c_{j\sigma}^+ c_{j\sigma}.$$

The index α is used here to denote a variety of spin-related operators, including x, y, z, $+$ and $-$, defined at lattice site j and $\hat{\sigma}^{(\alpha)}_{\sigma\rho}$ are the corresponding Pauli matrices, namely

$$\alpha = \text{“}z\text{”} \quad S^{(z)}_j := \frac{1}{2}(\hat{n}_{j\uparrow} - \hat{n}_{j\downarrow}) \tag{3.95}$$

$$\alpha = \text{“}+\text{”} \quad S^{(+)}_j := \frac{1}{\sqrt{2}} c^+_{j\uparrow} c_{j\downarrow} \tag{3.96}$$

$$\alpha = \text{“}-\text{”} \quad S^{(-)}_j := \frac{1}{\sqrt{2}} c^+_{j\downarrow} c_{j\uparrow} \tag{3.97}$$

$$\alpha = \text{“}x\text{”} \quad S^{(x)}_j := \frac{1}{2}(c^+_{j\uparrow} c_{j\downarrow} + c^+_{j\downarrow} c_{j\uparrow}) \tag{3.98}$$

$$\alpha = \text{“}y\text{”} \quad S^{(y)}_j := \frac{1}{2i}(c^+_{j\uparrow} c_{j\downarrow} - c^+_{j\downarrow} c_{j\uparrow}) \tag{3.99}$$

and the relationship among $S^{(\pm)}_j$, $S^{(x)}_j$ and $S^{(y)}_j$ is

$$S^{(\pm)}_j = \frac{1}{\sqrt{2}}(S^{(x)}_j \pm i S^{(y)}_j). \tag{3.100}$$

The spin susceptibility $\chi^{\alpha\alpha'}(\vec{Q}, i\omega_m)$ is then defined as

$$\chi^{(\alpha\alpha')}(\vec{Q}, i\omega_m) = \frac{1}{N} \sum_{j,j'} \int_0^\beta d\tau e^{-i\vec{Q}\cdot(\vec{r}_j - \vec{r}_{j'}) + i\omega_m \tau} C^{(\alpha\alpha')}(j, j', \tau) \tag{3.101}$$

where $\vec{Q} \in \mathcal{B}$ for an $L \times L$ lattice, and $C^{(\alpha\alpha')}$ is given by

$$C^{(\alpha\alpha')}(j, j', \tau) = \langle S^{(\alpha)}_j(\tau) S^{(\alpha')}_{j'}(0) \rangle. \tag{3.102}$$

Also, we define a momentum-Matsubara-frequency vector

$$Q \equiv (\vec{Q}, i\omega_m) \in \mathcal{B}_L \times \mathcal{M}_+. \tag{3.103}$$

If the Hamiltonian has spin rotational symmetry and there is no spontaneous breaking of that symmetry, the following symmetry properties hold

$$\chi^{(xx)}(\vec{Q}, i\omega_m) = \chi^{(yy)}(\vec{Q}, i\omega_m) = \chi^{(zz)}(\vec{Q}, i\omega_m) \tag{3.104}$$

$$\chi^{(\alpha\alpha')}(\vec{Q}, i\omega_m) = 0 \text{ if } \alpha \neq \alpha' \text{ and } \alpha, \alpha' = x, y, z. \tag{3.105}$$

Also, according to Equation (3.100),

$$\chi^{(+-)}(Q) = \chi^{(zz)}(Q) \tag{3.106}$$

It is an important feature of the Baym-Kadanoff-type conserving approximations that the approximations fully preserve these symmetry properties [41].

The spin susceptibility can be represented in terms of the creation and annihilation operators in the momentum space, $d^{+}_{\vec{k}\sigma}$ and $d_{\vec{k}\sigma}$

$$\begin{aligned}\chi^{(\alpha\alpha')}(\vec{Q}, i\omega_m) &= \int_0^\beta d\tau e^{i\Omega\tau} \sum_{k,k'} \sum_{\sigma\sigma'\rho\rho'} f_\alpha(\sigma,\sigma') f_{\alpha'}(\rho,\rho') \cdot \\ &\quad \langle d^{+}_{\vec{k}+\vec{Q}\sigma}(\tau) d_{\vec{k}\sigma'}(\tau) d^{+}_{\vec{k}'-\vec{Q}\rho}(0) d_{\vec{k}'\rho'}(0)\rangle \end{aligned} \tag{3.107}$$

where $f_\alpha(\sigma,\sigma')$ is related to the Pauli matrices, such that

$$\alpha = \text{“}z\text{”} \quad f_z(\sigma,\sigma') = \begin{cases} \frac{1}{2} & \text{if } \sigma = \sigma' = \uparrow \\ -\frac{1}{2} & \text{if } \sigma = \sigma' = \downarrow \\ 0 & \text{if otherwise} \end{cases} \tag{3.108}$$

$$\alpha = \text{“}+\text{”} \quad f_+(\sigma,\sigma') = \begin{cases} 1 & \text{if } \sigma = \uparrow,\ \sigma' = \downarrow \\ 0 & \text{if otherwise} \end{cases} \tag{3.109}$$

$$\alpha = \text{“}-\text{”} \quad f_-(\sigma,\sigma') = \begin{cases} 1 & \text{if } \sigma = \downarrow,\ \sigma' = \uparrow \\ 0 & \text{if otherwise.} \end{cases} \tag{3.110}$$

The spin susceptibility $\chi^{\alpha\alpha'}(\vec{Q}, i\omega_m = 0)$ is basically just the second derivative of the free energy (aside from some constant pre-factor) with respect to an external applied spatially sinusoidal magnetic field with wave vector $\vec{Q}$, and the amplitude $\vec{h}$, i.e,

$$\vec{h}_j = \vec{h}\cos(\vec{Q}\cdot\vec{r}_j), \tag{3.111}$$

acting on the local spins with a coupled Hamiltonian of the form

$$\hat{H}_{tot} = \hat{H} + \hat{H}_{\vec{h}} = \hat{H} + \sum_j \vec{h}_j \cdot \vec{S}_j \tag{3.112}$$

where $\hat{H}$ is the original Hamiltonian in the absence of the magnetic field $\vec{h}_j$.

3.12 Two Particle Vertex Diagram and Calculation of Spin Susceptibility

We employ the Feynman-Dyson approach to evaluate the spin susceptibility $\chi^{(\alpha\alpha')}(\vec{Q}, i\omega_m)$ as the sum of a certain class of diagrams, referred to as two-particle vertex diagrams. Similar

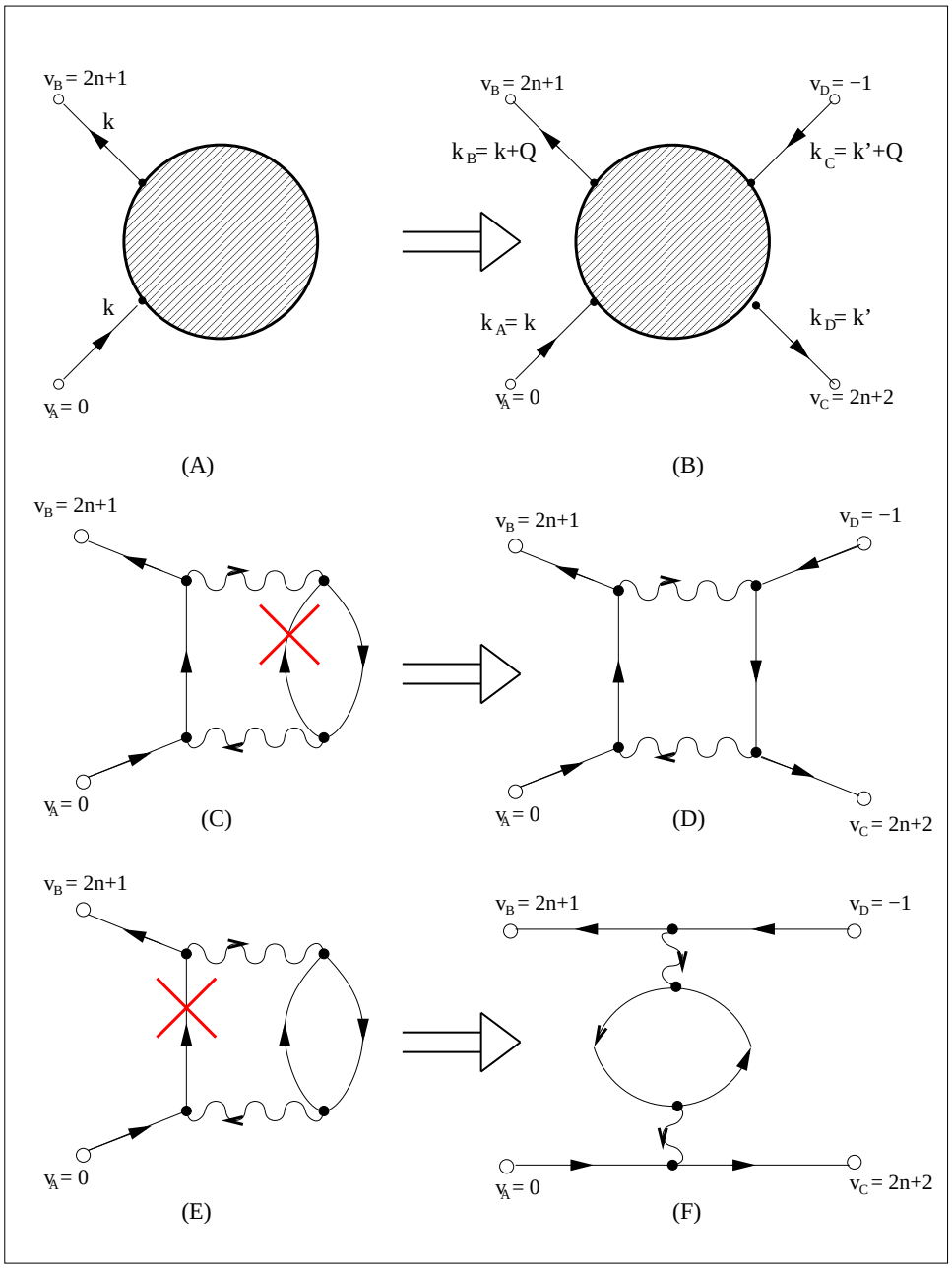

Figure 3.5: It is illustrated how the vertex diagram (B) can be generated from (A) self-energy diagram. The shaded circle in both (A) and (B) is to denote the internal topology (including internal G-lines, V-lines, and internal vertices except the vertices) of the single-particle self-energy diagram and two-particle vertex diagram respectively. The open circles are to denote the external vertices; and the close circles are to denote the internal vertices. Two examples are given to describe how different second-order vertex graphs are generated from a second-order self-energy graph. (C) One internal G-line in the second-order self-energy graph, which belongs to an internal G-line loop, is cut to generate (D) a second-order exchange vertex diagram. (E) One of the internal G-line that is in the base loop, of the same self-energy graph as (C), is cut to generate (F) a second-order direct vertex diagram.

to the self-energy diagrams, each nth-order vertex diagram contains n V-lines connecting $2n$ internal vertices labeled by $v = 1, 2, \cdots, 2n$. However, unlike the self-energy graphs, each two-particle vertex graph has four external vertices, two of them with in-going G-lines and two with out-going G-lines attached as shown in Figure 3.5(B). The two external vertices with in-going G-lines are labeled with $v_A = 0$ and $v_D = -1$, and the two external vertices with out-going G-lines are labeled with $v_B = 2n+1$ and $v_C = 2n+2$. As a consequence, each two-particle vertex diagram has only $2n-2$ internal G-lines, instead of the $2n-1$ internal G-lines of an n-th order self-energy diagram. Each vertex graph g can therefore be formally represented by a one-to-one mapping of v-sets:

$$g : \{-1, 0, 1, \cdots, 2n\} \rightarrow \{1, \cdots, 2n, 2n+1, 2n+2\} \tag{3.113}$$

such that, again, $v' \equiv g(v)$ is the label of the termination vertex of the G-line that originates from vertex v.

An important subset of vertex diagrams are the so-called irreducible vertex diagrams. They can be constructed directly from the irreducible self-energy graphs. Assume an nth-order irreducible self-energy graph with external vertices labeled as $v_A = 0$ and $v_B = 2n+1$ as shown in Figure 3.5(A). An irreducible vertex graphs g is then generated from this irreducible self-energy graph by cutting an arbitrary internal G-line of this self-energy graph into two G-lines, and linking these new two G-lines to the two additional external vertices $v_C = 2n+2$ and $v_D = -1$ respectively, as illustrated in Figure 3.5(C)-(F).

Depending on the G-line in the self-energy diagram that is cut, the irreducible vertex graphs can be further classified into two subsets, *direct graphs* and *exchange graphs*. If the internal G-line cut in the self-energy graph is in a closed loop of G-lines, then the generated irreducible two-particle vertex graph is called an exchange vertex graph as shown in Figure 3.5(C) and Figure 3.5(D). On the other hand, if the G-line, which is cut, belongs to the base loop of the self-energy graph, the newly generated irreducible vertex graph is a direct vertex graph as illustrated by Figure 3.5(E) and Figure 3.5(F). Topologically, in a direct vertex graph, a contiguous G-line path connecting vertex v_D to v_B can be found , and

another contiguous G-line path can be found connecting external vertex v_A to v_C. By contrast, in the exchange irreducible vertex graph, one cannot find such two contiguous G-line paths between v_D and v_B and between v_A and v_C respectively; rather v_D is connected to v_C and v_A to v_B in an exchange diagram.

Just as for evaluating self-energy diagrams, in order to calculate the value of a vertex diagram, we need to assign momentum-Matsubara-frequency vectors to all the internal G-lines and V-lines, such that each internal G-line numbered j is associated with a k_j for $j = 1, \cdots, 2n-2$, and each V-line ℓ is associated with q_ℓ as $\ell = 1, \cdots, n$. The momentum-Matsubara-frequency vectors, k_A, k_B, k_C and k_D respectively, that are assigned to the 4 external G-lines, labeled by $j \equiv -1$,0,$2n+1$ and $2n+2$ respectively, can be expressed in terms of only 3 independent external momentum-Matsubara-frequency vectors denoted by $k \equiv (\vec{k}, i\nu_m)$, $k' \equiv (\vec{k}', i\nu'_m)$ and $Q \equiv (\vec{Q}, i\omega_m)$ as follows:

$$k_A \equiv k_0 = k \tag{3.114}$$

$$k_B \equiv k_{2n+1} = k + Q \tag{3.115}$$

$$k_C \equiv k_{2n+2} = k' + Q \tag{3.116}$$

$$k_D \equiv k_{-1} = k' \tag{3.117}$$

as illustrated in Figure 3.5(B). And it is, again due to the momentum-frequency conservation, required that the sum of in-going k's must be equal to the sum of out-going k.

$$k_A + k_C = k_B + k_D. \tag{3.118}$$

On each internal vertex, the momentum-frequency conservation is imposed by Equation (3.17) as illustrated by Figure 3.2. Therefore, among the $2n-2$ G-lines, only for $n-1$ of them can we choose the momentum-Matsubara-frequency vector k independently. We can always choose a k-labeling of the internal G-lines such that the independent k_j are labeled by $j = 1, 2, \cdots, n-1$, and the dependent k_j as $j = n, n+1, \cdots, 2n-2$. And for convenience, we introduce a new notation $\bar{k}_j$ for dependent k_j in a manner that

$$\bar{k}_{j-n+1} := k_j \quad \text{for } j = n-1, \cdots, 2n-2 \tag{3.119}$$

Using this notation, the relations between independent and dependent internal momentum-Matsubara-frequency vectors can be expressed as

$$\bar{k}_j = \sum_{j'=-1}^{n-1} \sigma_G(j, j'; g) k_{j'} \quad \text{for } j = 1, \cdots, n-1 \tag{3.120}$$

$$q_\ell = \sum_{j'=-2}^{n-1} \sigma_V(\ell, j'; g) k_{j'} \quad \text{for } \ell = 1, \cdots, n-1 \tag{3.121}$$

where $k_{-2} = k_{2n+2} = k_C$ for a clear notation, and the conservation coefficients $\sigma_G(j, j'; g_v)$ and $\sigma_V(j, j'; g_v)$ are determined again by the vertex graph's topology g and take on values as 1, -1 and 0 only.

From this point, we will only discuss the direct vertex diagrams because they are the only diagrams that are required to calculate the spin susceptibility, which we are interested in. The exchange vertex diagrams are needed by the calculation of density susceptibility that won't be discussed in this thesis. The generalization of the following formalism to include exchange graphs, when needed, is straightforward. We will denote the set of nth-order irreducible direct two-particle vertex graphs as $\mathcal{V}_n$ in the following.

The Feynman rules for the calculation of the vertex diagram value of each nth-order irreducible direct vertex graph in $\mathcal{V}_n$ are described as the following:

1. With each G-line labeled by k_j ($j = 1, 2, \cdots, n-1$) or by $\bar{k}_j$ ($j = 1, 2, \cdots, n-1$), associate a factor of $G(k_j)$ or $G(\bar{k}_j)$, respectively, where $G(k_j)$ or $G(\bar{k}_j)$ is obtained from self-energy $\Sigma(k_j)$ or $\Sigma(\bar{k}_j)$ calculated by the approach described in Section 3.7.

2. With each V-line labeled by q_ℓ ($\ell = 1, 2, \cdots, n$), associate a factor $(-\frac{T}{N})V(q_l)$ where the value of $V(q_l)$ is given by

$$V(q_l) \equiv V(\vec{q}_l) \tag{3.122}$$

   and is independent of the Matsubara frequency $i\omega_{m_l}$ for $q_l \equiv (\vec{q}_l, i\omega_{m_l})$.

3. With each closed loop of internal G-lines, associate a factor of (-2). The total number of closed internal G-line loops in an nth-order vertex graph g is again denoted by $\Lambda_{n,g}$.

4. Multiply together all factors listed under (1), (2) and (3), and by another overall factor $(-N/T)$; then sum over all internal independent k_j-variables (for $j = 1, \cdots, n$), given the external $k \equiv k_0$. The result of this summation is this vertex graph's contribution to $\Gamma_{irr}(k, k', Q)$.

Hence, the value of the sum of all irreducible direct vertex diagrams, the so-called direct irreducible vertex function, is given by

$$\begin{aligned}\Gamma_{irr}(k,k';Q) &= \sum_{n=1}^{n_{max}}(-\frac{T}{N})^{n-1}\sum_{g\in\mathcal{V}_n}(-2)^{\Lambda_{n,g}}\sum_{k_1\in\mathcal{K}}\cdots\sum_{k_{n-1}\in\mathcal{K}}\prod_{j=1}^{n-1}G(k_j)\times \\ &\quad \prod_{j=1}^{n-1}G(\bar{k}_j)\prod_{\ell=1}^{n}V(q_\ell) \qquad (3.123)\end{aligned}$$

with a finite truncation of expansion order at the same n_{max} that was used for the self-energy diagram sum.

The above procedure to construct the two-particle vertex diagram ensures the two-particle Green's function, and hence the resulting spin susceptibility, to obey all the symmetry and conservation laws of the underlying Hamiltonian.

For the pure Hubbard model, the direct irreducible vertex graphs, $\mathcal{V}_n$, can be further restricted by the strict local form of the interaction matrix $V_{ij} = U\delta_{ij}$. The resulting reduced set of allowed irreducible direct vertex graphs is said to obey the *up-down vertex graph rule*. The up-down vertex graph rule is similar to the up-down rule for self-energy graph, which is discussed in Section 3.4. The only difference between the up-down self-energy graph rule and the up-down vertex graph rule is that in each direct vertex graph, besides $\Lambda_{n,g}$ closed internal G-line loops (indexed by λ as $\lambda = 1, \cdots, \Lambda_{n,g}$), there are two base loops. Again, we label the sequence of vertices that are in G-line loop λ as $v_1^{(\lambda)}, v_2^{(\lambda)}, \cdots, v_{M_\lambda}^{(\lambda)}$. The two base loops labeled by $\lambda = 0$ and $\lambda = -1$ in a direct irreducible vertex graph must obey Equation (3.23) and

$$v_1^{(0)} = 0 \equiv v_A \quad \text{and} \quad v_{M_0+1}^{(0)} = 2n+2 \equiv v_C \qquad (3.124)$$

$$v_1^{(-1)} = -1 \equiv v_D \quad \text{and} \quad v_{M_{-1}+1}^{(-1)} = 2n+1 \equiv v_B. \qquad (3.125)$$

The irreducible direct vertex graphs that obey the up-down vertex graph rule are called up-down irreducible direct graphs, and the set of the nth-order up-down irreducible direct graphs is denoted as $\mathcal{V}_n^{(\uparrow\downarrow)}$. Similar to the up-down self-energy diagram, the sum of spin variables for each internal G-line loop now contributes a factor (-1) to the value of the vertex diagram. The sum of all irreducible direct diagrams $\Gamma_{irr}(k,k';Q)$ can be written as sum of all irreducible direct up-down diagrams, such that

$$\begin{aligned}\Gamma_{irr}(k,k';Q) &= \sum_{n=1}^{n_{max}}(-\frac{T}{N})^{n-1}\sum_{g\in\mathcal{V}_n^{(\uparrow\downarrow)}}(-1)^{\Lambda n,g}\sum_{k_1\in\mathcal{K}}\cdots\sum_{k_{n-1}\in\mathcal{K}} \\ &\prod_{j=1}^{n-1}G(k_j)\prod_{j=1}^{n-1}G(\bar{k}_j)\prod_{\ell=1}^{n}V(q_\ell). \end{aligned} \tag{3.126}$$

The Monte Carlo summation is only applied to the calculation of high-order vertex diagrams with with order $n \geq 3$, while the first- and second-order irreducible vertex diagram contributions to $\Gamma_{irr}(k)$ are calculated by brute force. We employ an analogous perfect sampling Monte Carlo summation method as described in Section 3.8, and set the Monte Carlo weight function $W^{(n)}(k_1,\cdots,k_{n-1})$ as

$$W^{(n)}(k_1,\cdots,k_{n-1}) = \prod_{j=1}^{n-1}|G(k_j)| \tag{3.127}$$

for nth-order vertex diagrams. The Monte Carlo summation of the nth order contribution to $\Gamma_{irr}(k)$, denoted by $\Gamma_{irr}^{(n)}(k)$, proceeds by the perfect sampling method, described in Section 3.7.

We need to evaluate the sum of the reducible direct vertex diagrams, the so-called reducible direct vertex function, which is required to calculate spin susceptibility [41]. This reducible direct vertex function, denoted by $\Gamma_{red}(k,k',Q)$, can be calculated from $\Gamma_{irr}(k,k';Q)$ by using the Bethe-Salpeter equations [37][38][57]

$$\begin{aligned}\Gamma_{red}(k,k',Q) &= \Gamma_{irr}(k,k',Q) + \\ &\sum_{k_1}\Gamma_{irr}(k,k_1,Q)G(k_1+Q)G(k_1)(-\frac{T}{N})\times\Gamma_{red}(k_1,k',Q). \end{aligned} \tag{3.128}$$

For convenience, we introduce a matrix notation for Equation (3.128). We treat k and k' as the matrix indices and thus denote the value of the irreducible and reducible direct vertex functions for given Q as a matrix $\hat{\Gamma}_{irr}(Q)$ and a matrix $\hat{\Gamma}_{red}(Q)$, respectively.

Then, Equation (3.128) can be written as

$$\hat{\Gamma}_{red}(Q) = \hat{\Gamma}_{irr}(Q) + \hat{\Gamma}_{irr}(Q)\hat{G}_{\Gamma}(Q)\hat{\Gamma}_{red}(Q) \tag{3.129}$$

where matrix $\hat{G}_{\Gamma}(Q)$ is defined to have matrix elements

$$G_{\Gamma}(k, k', Q) = (-\frac{T}{N})\delta_{k,k'}G(k+Q)G(k). \tag{3.130}$$

Hence, $\hat{\Gamma}_{red}(Q)$ is solved by the following equations,

$$\hat{\Gamma}_{red}(Q) = \frac{1}{\hat{1} - \hat{\Gamma}_{irr}(Q)\hat{G}_{\Gamma}(Q)} \cdot \hat{\Gamma}_{irr}(Q) \tag{3.131}$$

where $\hat{1}$ is a unit matrix.

The spin susceptibility $\chi^{(zz)}(Q)$ can be expressed in a matrix representation [37][38][57] as

$$\chi^{(zz)}(Q) \;\; = \;\; \chi_0^{(zz)}(Q) + \chi_{vc}^{(zz)}(Q) \tag{3.132}$$

where $\chi_0^{(zz)}(Q)$ is the leading loop term, given by

$$\chi_0^{(zz)}(Q) = \hat{u}^{+}\hat{G}_{\Gamma}(Q)\hat{u}, \tag{3.133}$$

$\chi_{vc}^{(zz)}(Q)$ is the so-called "vertex correction" term to $\chi^{(zz)}(Q)$ and given by

$$\chi_{vc}^{(zz)}(Q) = \hat{u}^{+}\hat{G}_{\Gamma}(Q)\hat{\Gamma}_{red}(Q)\hat{G}_{\Gamma}(Q)\hat{u}, \tag{3.134}$$

and $\hat{u}$ is a column vector, defined to have vector elements

$$u(k) = 1, \tag{3.135}$$

and row vector $\hat{u}^{+}$ is the transpose of the column vector $\hat{u}$.

Combining Equation (3.131), (3.132), (3.133) and (3.134), we have the final solution to the spin susceptibility $\chi^{(zz)}(Q)$, i.e.,

$$\chi^{(zz)}(Q) = \hat{u}^{+}\hat{G}_{\Gamma}(Q)\frac{1}{\hat{1} - \hat{\Gamma}_{irr}(Q)\hat{G}_{\Gamma}(Q)}\hat{u}. \tag{3.136}$$

In a numerical calculation, the CPU time required for inverting a matrix $\hat{K}$ is much more than the CPU time required for solving a set of linear equations, i.e, $\hat{y} = \hat{K}\hat{x}$, where $\hat{x}$ and $\hat{y}$ are column vectors. Therefore, in order to solve for the spin susceptibility in Equation (3.136), we solve the linear equations instead of doing the matrix inversion to $\frac{1}{\hat{1}-\hat{\Gamma}_{red}(Q)\hat{G}_{\Gamma}(Q)}$. Here, we construct matrix $\hat{K}$, such that

$$\hat{K} = \hat{1} - \hat{\Gamma}_{red}(Q)\hat{G}_{\Gamma}(Q). \tag{3.137}$$

To calculate the column vector

$$\hat{w} = (\hat{K})^{-1}\hat{u} \tag{3.138}$$

is equivalent to solving the linear equations

$$\hat{K}\hat{w} = \hat{u}. \tag{3.139}$$

Therefore, in implementation, we calculate Equation (3.136) by first constructing matrix $\hat{K}$, then solving Equation (3.139) for $\hat{w}$, and finally calculate $\chi^{(zz)}(Q)$ by

$$\chi^{(zz)}(Q) = \hat{u}^{+}\hat{G}_{\Gamma}(Q)\hat{w}. \tag{3.140}$$

Chapter 4

Results

In order to look for the Mott-Hubbard gap and the antiferromagnetism of the two-dimensional Hubbard model at half-filling, we performed simulations on finite systems with periodic boundary conditions for inverse temperature $\beta = 1/k_B T$ up to $\beta = 20/t_1$ and on-site repulsion interaction U up to $U = 12t_1$, and unless otherwise stated the chemical potential $\mu = U/2$ to maintain particle-hole symmetry. We use the particle-hole symmetry of the Hubbard model to test our code, the convergence to self-consistency, and the Monte Carlo algorithm, and also to simplify the analysis of the data. The single-particle spectral weight $A(\vec{k}, \omega)$ is inferred from high-quality Monte Carlo summation data by the maximum entropy method (MEM). It should be noted that t_1 in physical units is typically of the order of a few tenths of an eV for the Hubbard model applied to cuprates. For example, t_1 of around 0.2 to 0.3 eV has been estimated for La_2CuO_4 based on electronic structure data, corresponding to about 2200 to 3300 K in temperature units. Hence our simulations reach down to $T = 1/(k_B\beta)$ around 150 to 260 K in physical units for $\beta = 20/t_1$. For all results below we use t_1 as a unit of energy and frequency, i.e., we set $t_1 = 1$ and $\hbar = 1$.

In our Monte Carlo simulation, we use a powerful pseudo-random number generator developed by Makoto Matsumoto and Takuji Nishimura [58]. This generator features an extremely long period and 623-dimensional equidistribution up to 32 bits accuracy.

4.1 Convergence of Self-consistent Algorithm and Monte Carlo Sampling

We utilized the self-consistent diagrammatic expansion method combined with Monte Carlo summation technique to calculate the self-energy. The self-consistent calculation is expected

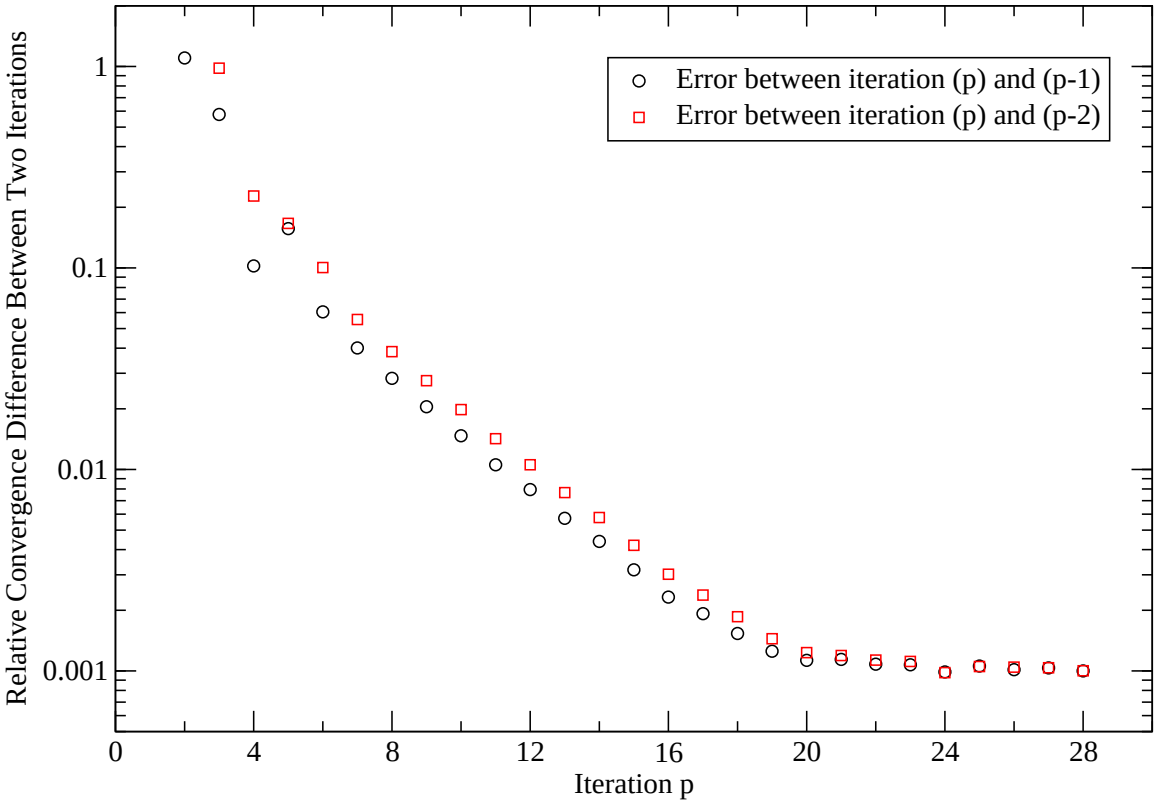

Figure 4.1: Self-consistent iteration difference of the self-energy $\Sigma(k)$ between two adjacent iterations and two second nearest iterations . The data are for a second order calculation ($n_{max} = 2$) performed on a 4×4 lattice, at $T = 1.0t_1$, $U = 8.0t_1$ and $\mu = U/2$. The Monte Carlo (relative) error is comparable to but smaller than the (relative) convergence difference.

to converge in weak and intermediate coupling. In our test, the self-consistent algorithm converges with the coupling at least as high as $U = 12t_1$. The self-consistent convergence difference and Monte Carlo error, defined as Equation C.5 and C.6 in Appendix C.3 and Equation C.4 and C.2 in Appendix C respectively, exist simultaneously during the self-consistent iteration.

Figure 4.1 shows a typical convergence process. A criteria for judging whether the self-consistency iteration has converged or not is to compare the convergence difference between two adjacent iterations with that between two second nearest iterations. Upon convergence, the above two iteration differences should be close to each other, and the magnitudes should be comparable to the Monte Carlo statistical error.

The Monte Carlo error is determined by the Monte Carlo sampling size, and sets the upper limit for the precision of the self-consistent iteration (i.e, a lower limit for the lowest achievable convergence difference).

The simulations were performed on an IBM p655 High Performance Computer, usually with 32 or 64 processors. The codes are parallelized by the parallelization scheme introduced in Section 3.8. For instance, to calculate the Green's function and self-energy of the Hubbard model on a 4×4 lattice with 140 discrete Matsubara frequencies, for one self-consistency iteration, the CPU time is 12,800 single-processor seconds (i.e, it takes 400 seconds to finish one self-consistency iteration on 32 processors). The total number of self-consistency iterations required to reach convergence is different for various model configurations including lattice size L, temperature T and on-site interaction U.

In our Monte Carlo simulation, we set the relative self-consistency convergence difference as 10^{-3}. And we controlled the relative Monte Carlo statistical error to be less and equal to the convergence difference by choosing the proper Monte Carlo sample size. For example, we usually chose the Monte Carlo sample size as 1% of the original problem size for second order approximation, i.e., $M \approx |\mathcal{K}|^2/100$.

Order	Number of Diagram	
	irreducible	up-down irreducible
1	2	1
2	2	1
3	10	2
4	82	9
5	898	54
6	12081	390

Table 4.1: Number of irreducible single-particle self-energy diagrams (column 2) and irreducible diagrams that conforms to the spin-up-down rule (column 3) defined in Section 3.4

We also compared the results obtained by brute force calculation and the Monte Carlo calculation for the Hubbard model on a 4×4 lattice at $T = 1.0t_1$. The difference between these two solutions is indistinguishable to within the self-consistency iteration difference, i.e, the Monte Carlo calculation is able to reach the same convergence criterion as the brute force does, though a few more self-consistency iterative steps are required by the Monte-Carlo-summation-based code.

4.2 Self-Energy

The diagrammatic expansion approach relies on the creation of irreducible self-energy diagrams. Using graph theoretic methods [44] the whole set of irreducible single- and two particle diagrams were generated up to sixth order. From these diagrams, we selected all diagrams, which obey the up-down rule, for Hubbard model self-energy. Table 4.2 shows the number of all irreducible diagrams from second order to sixth order. The highest order (n_{max}) calculation that we have actually carried out is fourth order due to the current limitations of our computational resources.

In order to check our two diagram expansion computer codes, based on Equation (3.22) or Equation (3.27), the self-energy is generated by brute force summation for the general

irreducible self-energy diagrams series, Equation (3.22), compared with those generated for up-down irreducible self-energy diagrams series, Equation (3.27). The results generated by the two methods matches exactly, showing that the computer codes based on the set of irreducible self-energy diagrams and the code based on the up-down irreducible self-energy diagrams are consistent.

Figure 4.2 and Figure 4.3 show the self-energy of the second order approximation on a 4×4 lattice with $U = 8t_1$ at half-filling. The self-energy on the Fermi surface, $\Sigma(\pi/2, \pi/2, i\nu_m)$, has the real part very close to $U/2 = 4t_1$. From previous discussion (Equation 3.93 in Section 3.10), the first-order contribution $\Sigma^{(1)}(k)$ should be exactly equal to $U/2 = 4t_1$ in this case. Combined with Equation (3.91), the real part of $\Sigma(\pi/2, \pi/2, i\nu_m)$ should also be exactly equal to $U/2 = 4t_1$. As shown in Figure 4.2A, the real part of $\Sigma(\pi/2, \pi/2, i\nu_m)$ equals $U/2$ to within an absolute error of about $5 \times 10^{-3}t_1$, which can be ignored when compared with either $4t_1$ or this self-energy's imaginary part. The real part of $\Sigma(\vec{k}, i\nu_m)$, if $\vec{k}$ is off the Fermi surface, is symmetric to the real part of $\Sigma(\vec{k}+\vec{K}, i\nu_m)$ (with $\vec{K} = (\pi, \pi)$) about $4t_1$, as illustrated in Figure 4.3, and required by particle-hole symmetry, as discussed in Section 3.10 Equation (3.86).

The imaginary part of the self-energies of different momenta $\vec{k}$ differ from each other insignificantly. The maximum magnitude of $\mathrm{Im}\Sigma(\vec{k}, i\nu_m)$ is much larger than the corresponding $\mathrm{Re}\Sigma_>(\vec{k}, i\nu_m)$, i.e., the imaginary part dominates the value of the Green's function at low Matsubara frequency and low temperature, according to Equation (3.12). Another observation is that at low temperature $T = 0.05t_1$ and $T = 0.10t_1$, the imaginary part of the self-energies seems to be on a same curve, in both cases to be on and off the Fermi surface.

With the decreasing temperature, the imaginary part of the self-energy has a more noticeable change in the low Matsubara frequency range than the real part.

The sum of all the third order self-energy diagrams' contribution, $n = 3$, shown in Figure 4.4 and Figure 4.5, are zero to within the Monte Carlo errors, which conforms to what has been proven in Appendix A.3 that, at particle-hole symmetry, the contribution of

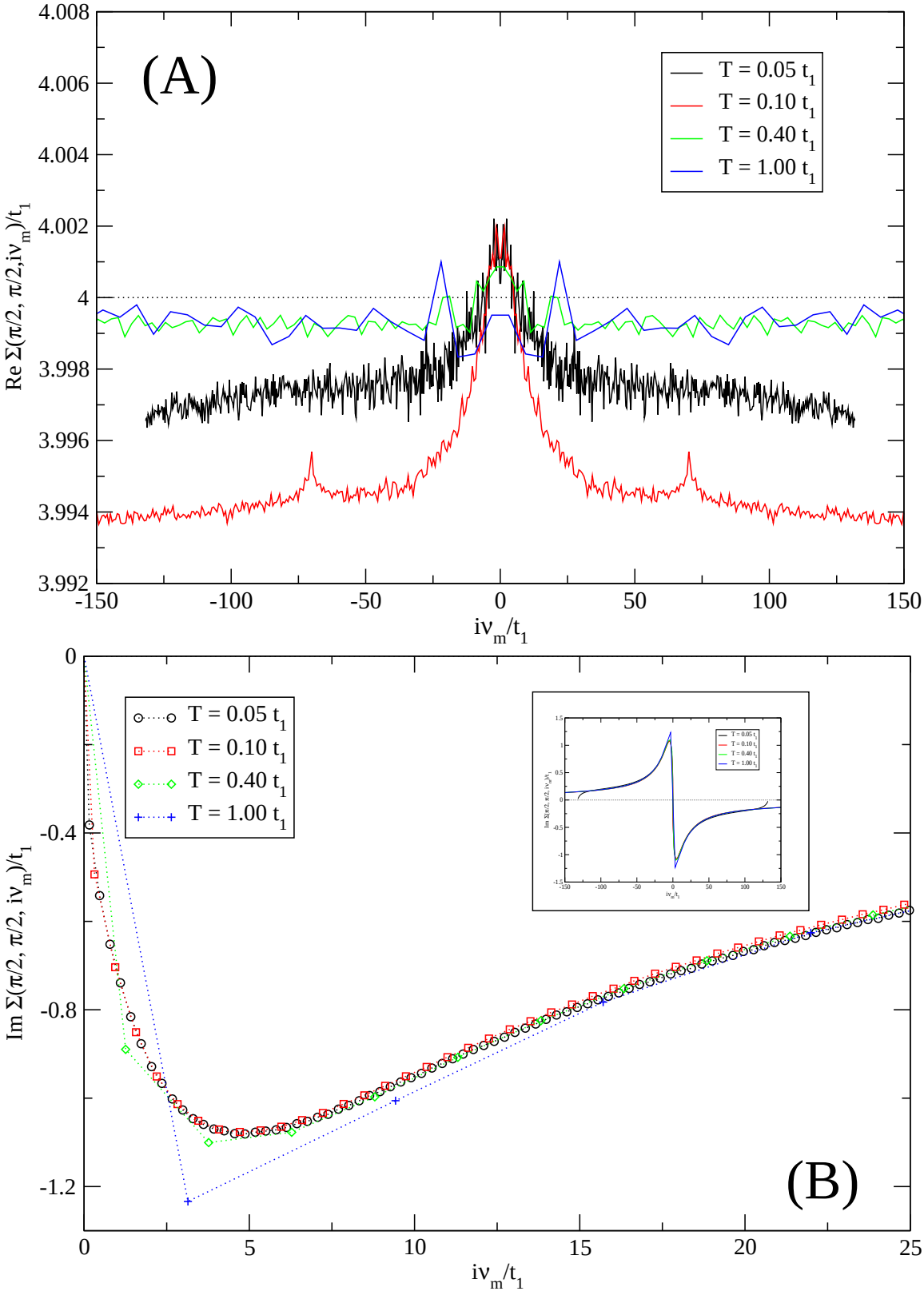

Figure 4.2: Self-energy of momentum $\vec{k}$, which is on the Fermi surface ($\vec{k} = (\pi/2, \pi/2)$), of the Hubbard model on a 4×4 lattice with $U = 8t_1$ at half-filling by second-order approximation. (A) shows the real part of $\Sigma(\vec{k}, i\nu_m)$, (B) presents the imaginary part of self-energy at low Matsubara frequency. The inset of (B) is the imaginary part in a large range of Matsubara frequencies .

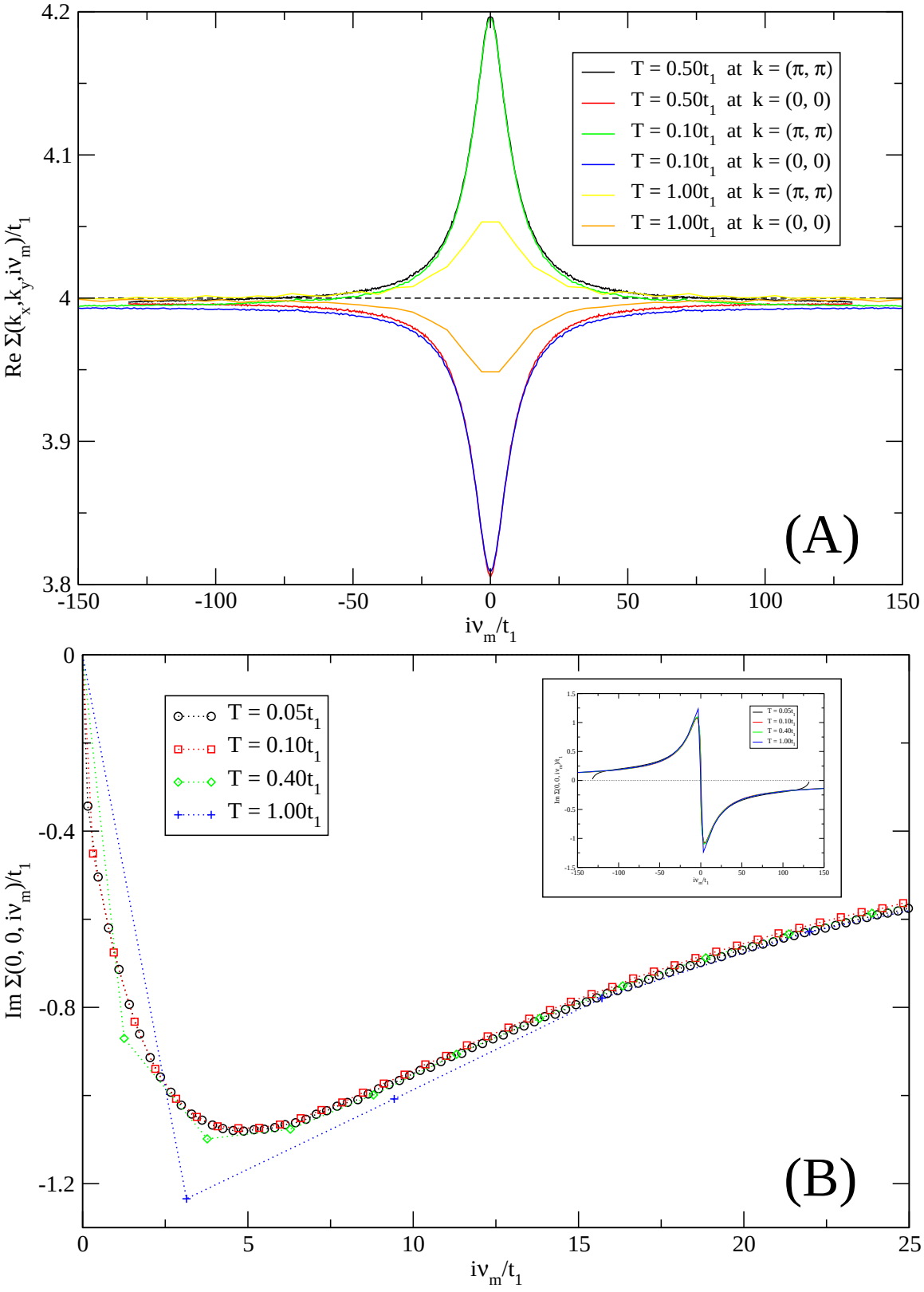

Figure 4.3: Self-energy of momentum $\vec{k}$, which is off the Fermi surface, of the Hubbard model on a 4×4 lattice with $U = 8t_1$ at half-filling by second-order approximation. (A) shows the real part of $\Sigma(\vec{k}, i\nu_m)$, (B) presents the imaginary part of self-energy at low Matsubara frequency. The inset of (B) is the imaginary part in a large range of Matsubara frequencies .

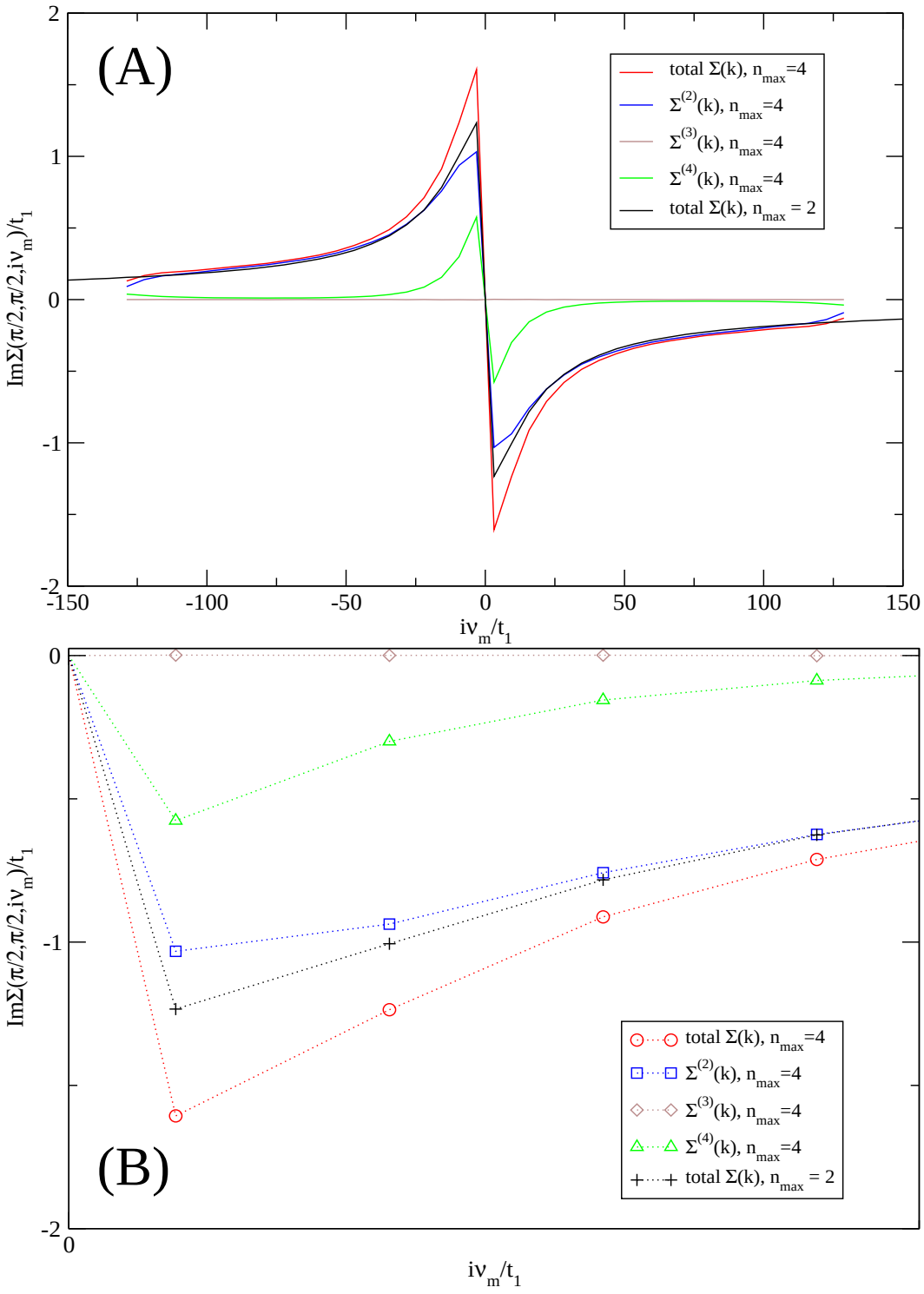

Figure 4.4: The imaginary part of self-energy $\mathrm{Im}\Sigma(k)$, where $\vec{k} = (\pi/2, \pi/2)$ is on the Fermi surface, calculated by the fourth-order approximation (denoted as "total $\Sigma(k)$, $n_{max} = 4$") is compared with the imaginary part of the self-energy calculate by the second-order approximation (denoted as "total $\Sigma(k)$, $n_{max} = 2$") on a 4×4 square lattice with $U = 8t_1$ and $\mu = 4t_1$, at $T = 1.0t_1$ and demonstrated in (A) large range of Matsubara frequency and (B) low Matsubara frequency range respectively. The imaginary part of the contributions of second-, third- and fourth-order self-energy diagrams at the fourth-order approximation, i.e, $\Sigma^{(2)}(k)$, $\Sigma^{(3}(k)$ and $\Sigma^{(4)}(k)$ for $n_{max} = 4$, respectively, are also shown in (A) and (B).

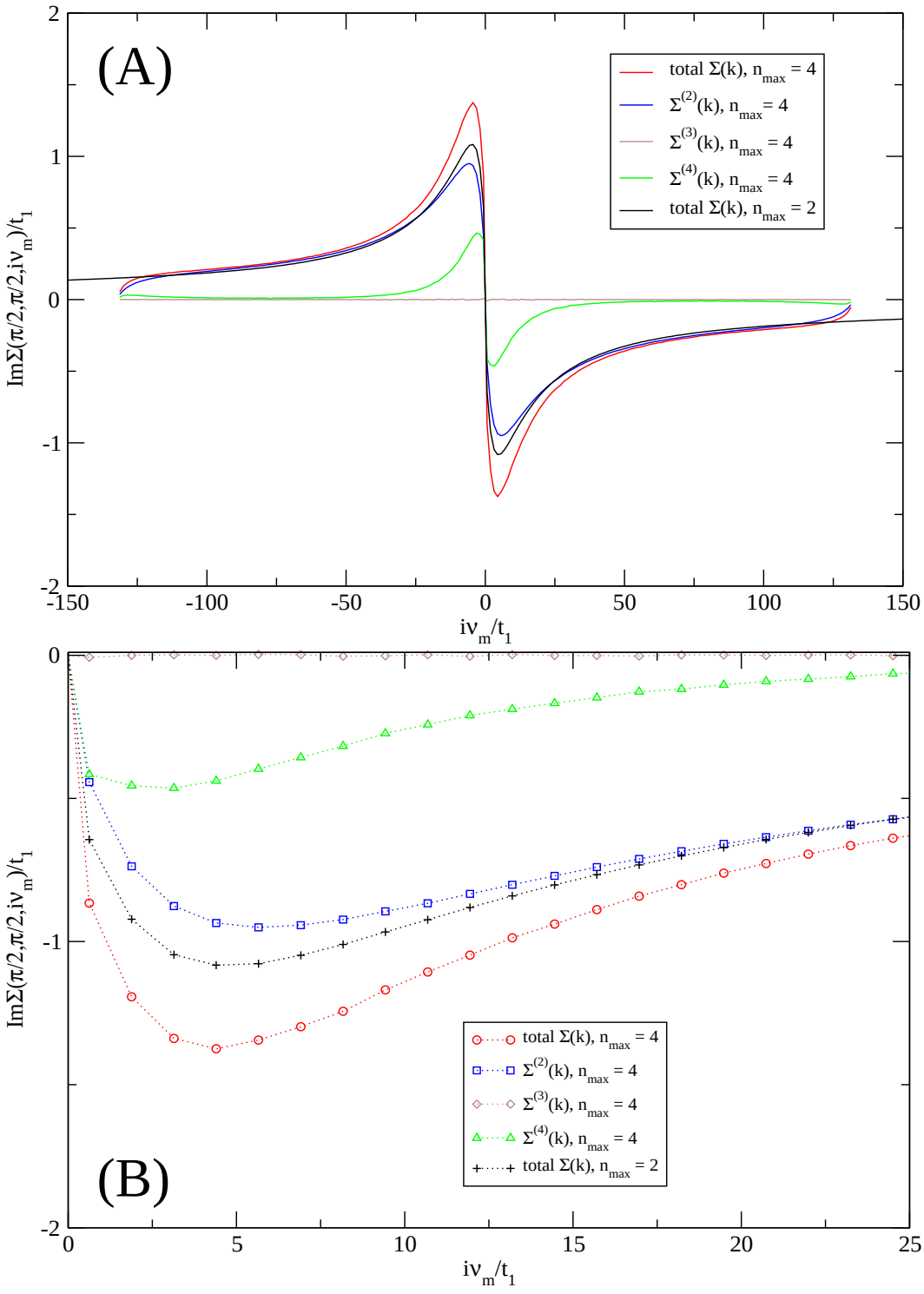

Figure 4.5: The imaginary part of self-energy $\mathrm{Im}\Sigma(k)$, where $\vec{k} = (\pi/2, \pi/2)$ is on the Fermi surface, calculated by the fourth-order approximation (denoted as "total $\Sigma(k)$, $n_{max} = 4$") is compared with the imaginary part of the self-energy calculate by the second-order approximation (denoted as "total $\Sigma(k)$, $n_{max} = 2$") on a 4×4 square lattice with $U = 8t_1$ and $\mu = 4t_1$, at $T = 0.2t_1$ and demonstrated in (A) large range of Matsubara frequency and (B) low Matsubara frequency range respectively. The imaginary part of the contributions of second-, third- and fourth-order self-energy diagrams at the fourth-order approximation, i.e, $\Sigma^{(2)}(k)$, $\Sigma^{(3}(k)$ and $\Sigma^{(4)}(k)$ for $n_{max} = 4$, respectively, are also shown in (A) and (B).

any odd order expansion terms to the self-energy are zero. The contribution of each individual diagram of the third order to the imaginary part of the self-energy differs only in sign and magnitude. All the third-order irreducible diagrams are proportional to each other, and add up to zero, which is also seen by Zlatić [46]. The third order contribution does not vanish after the first few self-energy iterations, i.e., iteration to self-consistency is necessary for the sum of the sum of the third order diagrams to disappear, as required by particle-hole symmetry. The value of the third-order diagram sum is not zero when calculated with the bare Green's function (G^0), but it diminishes to zero in a few (usually 2 to 3) iterations. This illustrates one of the fundamental properties of the "conserving" approximation [41]: self-consistency is a necessary requirement to preserve the symmetry of the Hamiltonian.

At intermediate and strong coupling, the fourth order self-energy diagrams are expected to significantly contribute to the self-energy, especially in the low Matsubara frequency range. Even at an intermediate temperature, for example, $T = 1.0t_1$ and $U = 8t_1$ shown in Figure 4.4, the contribution of the fourth order diagrams is not negligible as ν_m varies from -20 to 20. This can affect the low imaginary frequency Green's function on the Fermi surface substantially. We thus expect that the fourth order contribution to the self-energy can have a very large effect on the spectral weight function at low temperature.

Our results also show that at a variety of temperatures and if the other conditions are kept the same, the imaginary part of the self-energy $\Sigma(\vec{k}, i\nu_m)$ differs only at the low Matsubara frequencies, whereas the high-frequency's behaviors are indistinguishable. The real part of the self-energy is composed of $\mathrm{Re}\Sigma^{(1)}$, a constant to all temperatures at particle-hole symmetry, and $\mathrm{Re}\Sigma_>$ whose maximum magnitude is much smaller than the corresponding imaginary part. With varying temperature, the real part also has an unnoticeable change over all Matsubara frequencies.

The contributions from each of the self-energy diagrams, at both second order and fourth order, to the self-energy are all of comparable magnitude. Therefore, our decision to perform a brute force summation over all diagram topologies $g \in \mathcal{G}_n$ at each order in the Monte Carlo

summation is justified, because this brute force summation over all $g \in \mathcal{G}_n$ substantially reduces statistical error.

Another set of tests was done on the Hubbard system with a larger on-site interaction $U = 12t_1$, at half-filling again, i.e., with $\mu = U/2$. Some related results are shown in Figure 4.6. According to Figure 4.6B, the shape of the imaginary part of self-energies at $U = 12t_1$ is similar to those with $U = 8t_1$. The difference of the maximum magnitude of self-energies of half-filled Hubbard model system on same size of lattice is almost proportional to the ratio of the on-site repulsion. For the second order approximation, the Matsubara frequency related to the maximum value of self-energy with $U = 12t_1$, when ν_m is positive, is larger than that of the self-energy with $U = 8t_1$, indicating that a higher order expansion is essential for larger on-site repulsion.

4.3 Green's Function

The self-energy determines the behavior of the Green's function via the Dyson Equation [37] by Equation (3.12).

When the Matsubara frequency $i\nu_m$ approaches to infinity, the value of the Green's function is dominated by $1/(i\nu_m)$, Equation (3.31), that the Green's function at large $i\nu_m$ becomes $\vec{k}$-independent and cannot be distinguished by different momentum $\vec{k}$. This can be found at a variety of temperatures, both on and off Fermi surface, shown in Figure 4.7, Figure 4.8 and Figure 4.9.

At low frequency, the value of the Green's function is determined by both the quasiparticle band energy $E_{\vec{k}}$ and the higher order self-energy $\Sigma_>(\vec{k}, i\nu_m)$. The behavior of the Green's functions is substantially different if they are on or off the Fermi surface. On the Fermi surface, by definition, $E_{\vec{k}_F}$ is zero, both the imaginary part of $\Sigma_>(\vec{k}_F, i\nu_m)$ and $i\nu_m$ determines the value of $G(\vec{k}_F, i\nu_m)$ in the low-Matsubara-frequency range via the Dyson equation (Equation (3.12)). At a low temperature, ν_m is comparable to or even much smaller than $\mathrm{Im}\Sigma_>(\vec{k}_F, i\nu_m)$. Thus in this situation, the Green's function presents the characteristic of the

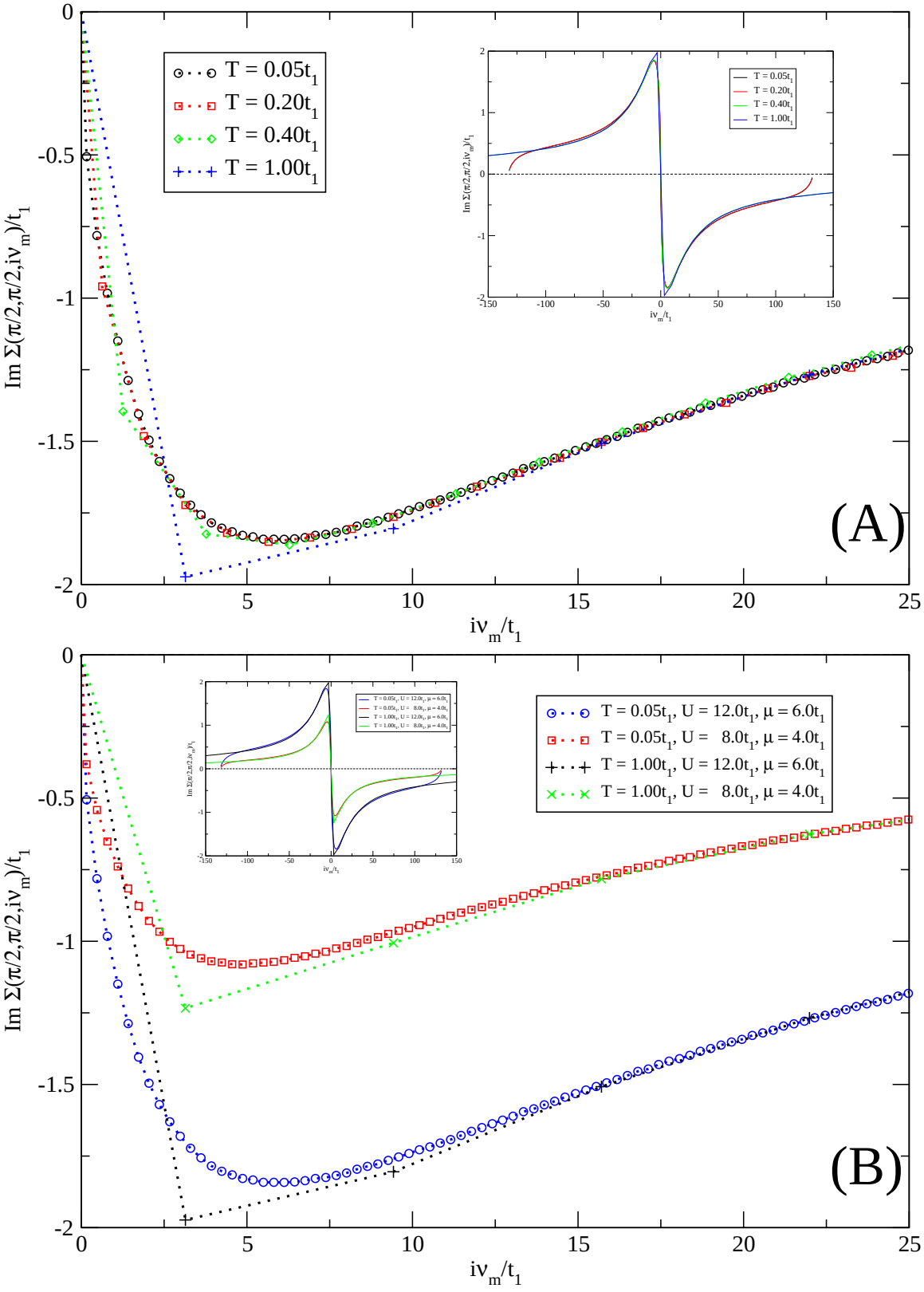

Figure 4.6: Second-order approximation on a 4×4 square lattice with $U = 12t_1$, $\mu = 6t_1$ at a variety of temperatures, (A) showing the imaginary part of the self-energy on Fermi surface with $\vec{k} = \pi/2, \pi/2$, and (B) are compared with self-energies on a same square lattice with $U = 8t_1$ and $\mu = 4t_1$.

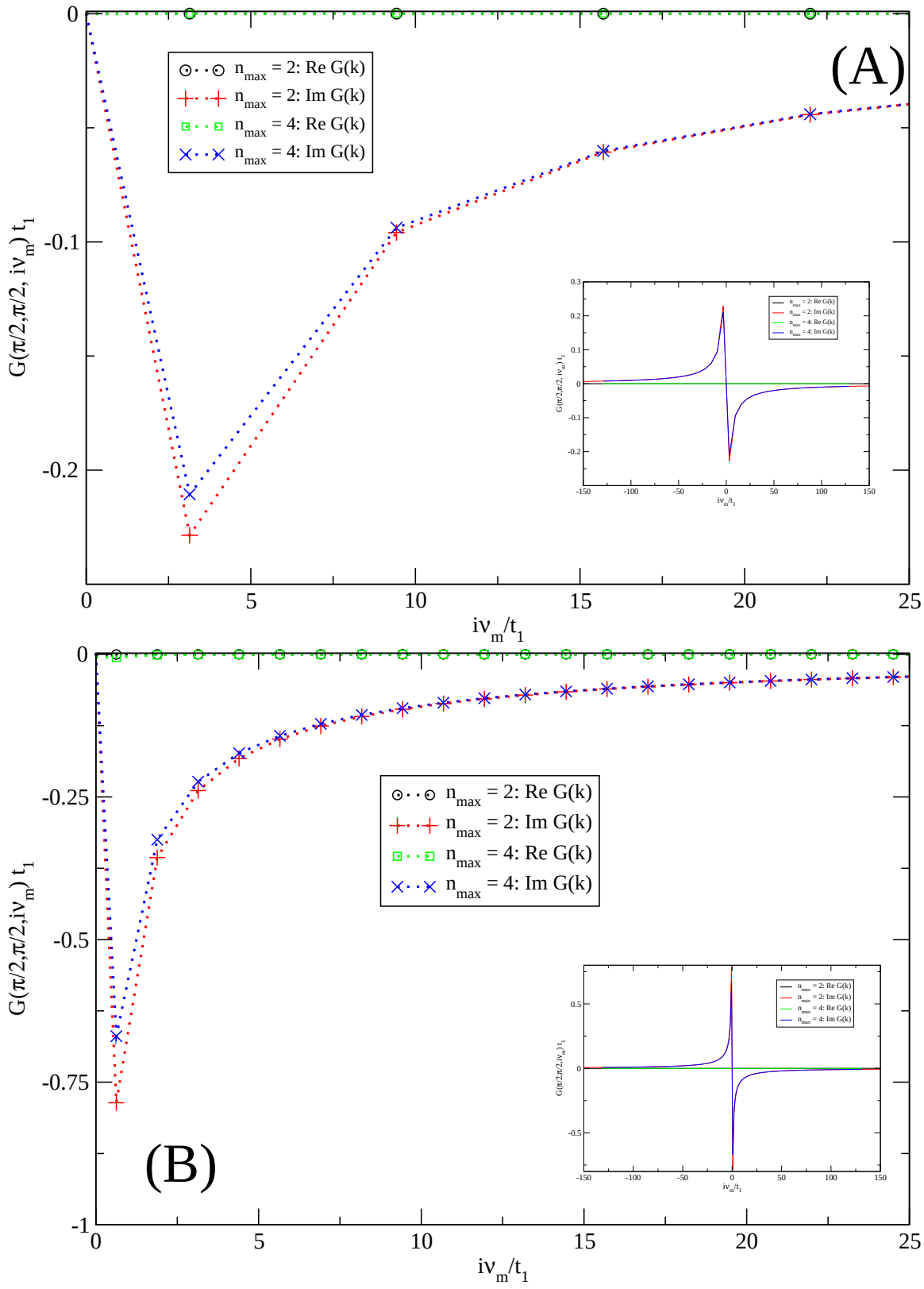

Figure 4.7: Green's function $G(\vec{k}, i\nu_m)$ [in units of t_1^{-1}] on the Fermi surface ($\vec{k} = (\pi/2, \pi/2)$ on 4×4 square lattice with $U = 8t_1$ and $\mu = 4t_1$ calculated by both second- and fourth-order approximation at (A) $T = 1.0t_1$ and (B) $T = 0.2t_1$. In the insets of both (A) and (B) give the corresponding Green's function in large range of $i\nu_m$.

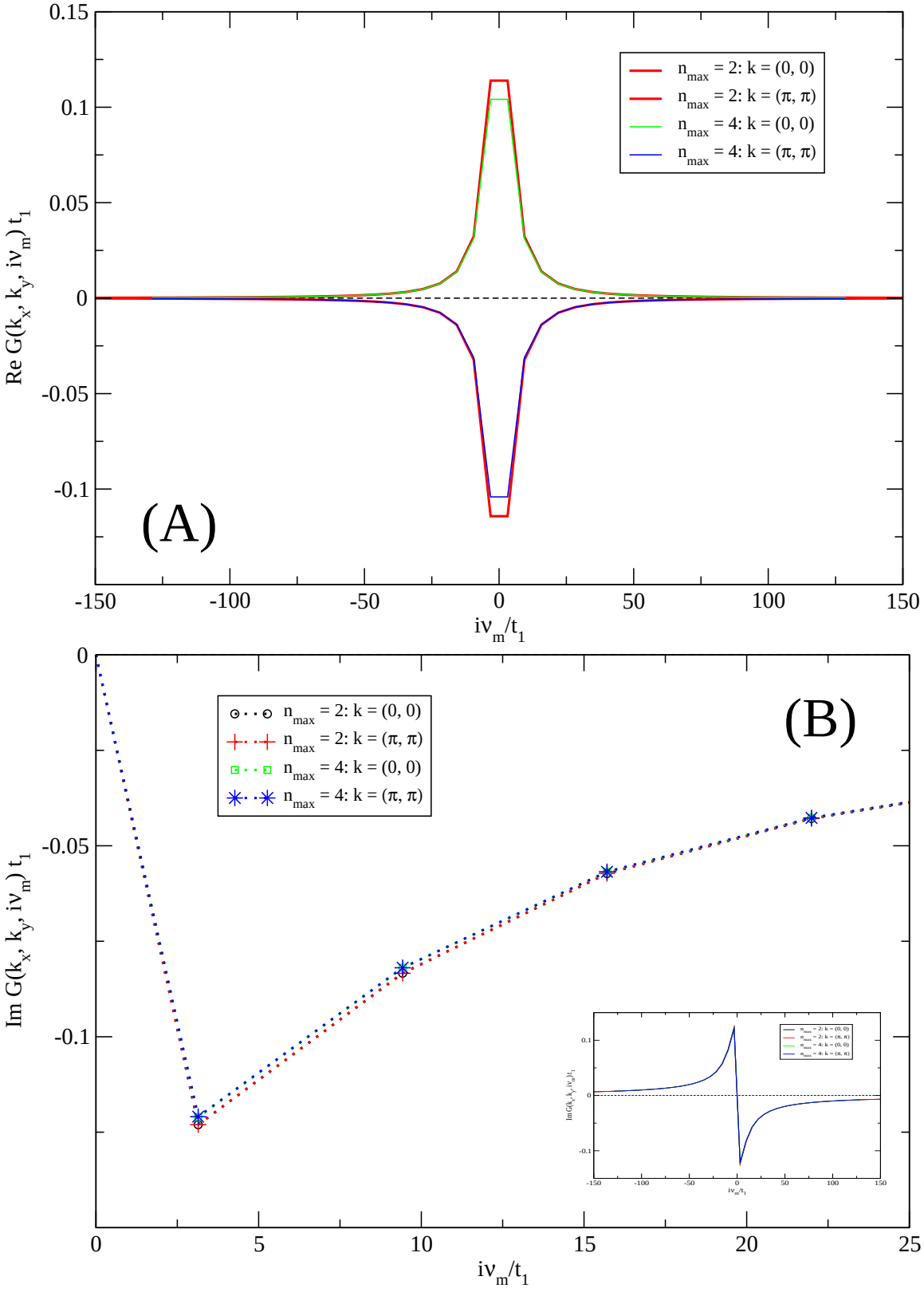

Figure 4.8: Green's function $G(\vec{k}, i\nu_m)$ [in units of t_1^{-1}] off the Fermi surface ($\vec{k} = (0,0)$ and $\vec{k} = (\pi, \pi)$ on 4×4 square lattice with $U = 8t_1$ and $\mu = 4t_1$ calculated by both second- and fourth-order approximation at $T = 1.0t_1$ with (A) real part and (B) imaginary part shown individually. The inset of (B) shows the imaginary part of Green's function in a large range of $i\nu_m$.

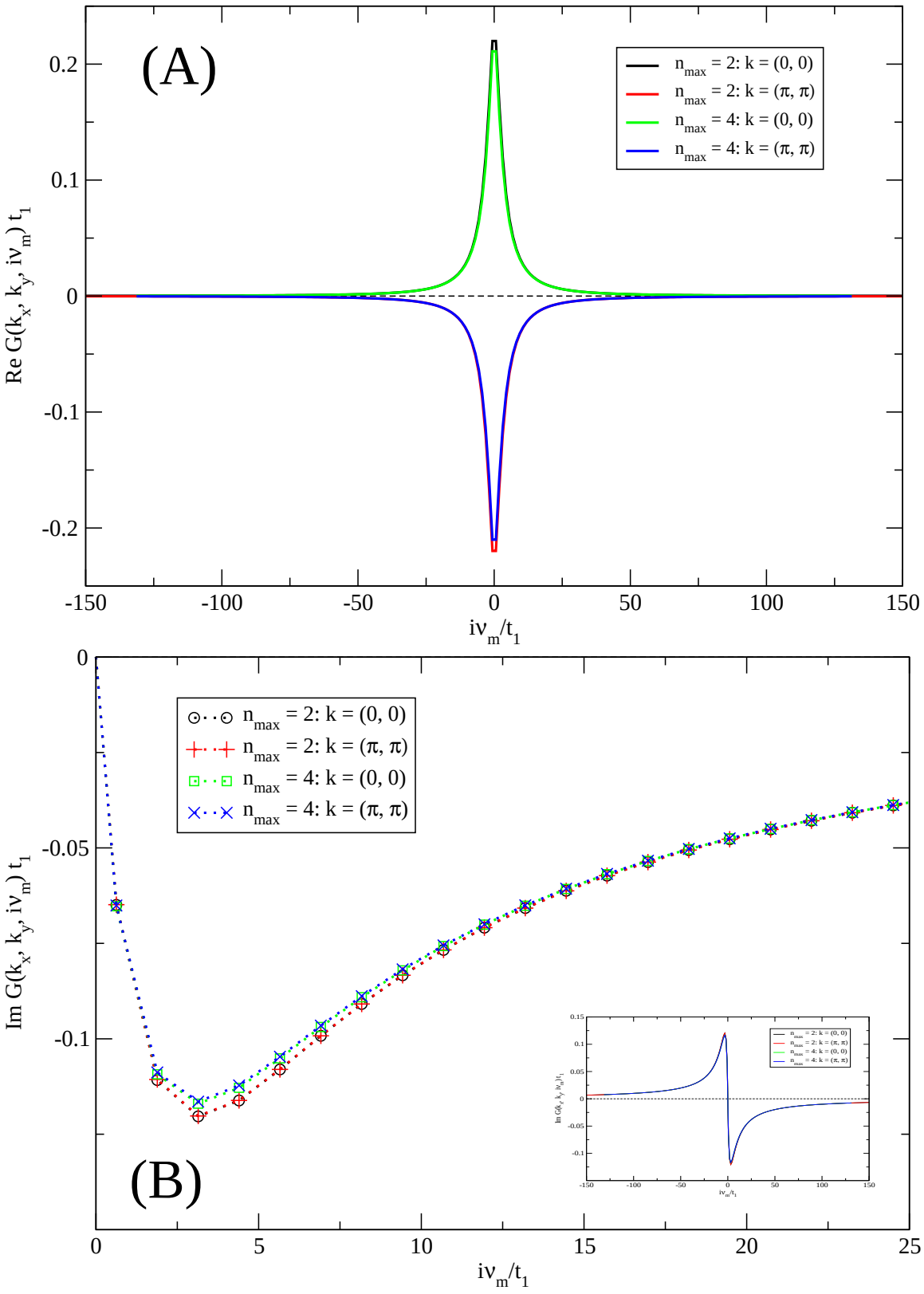

Figure 4.9: Green's function $G(\vec{k}, i\nu_m)$ [in units of t_1^{-1}] off the Fermi surface ($\vec{k} = (0,0)$ and $\vec{k} = (\pi, \pi)$ on 4×4 square lattice with $U = 8t_1$ and $\mu = 4t_1$ calculated by both second- and fourth-order approximation at $T = 0.2t_1$ with (A) real part and (B) imaginary part shown individually. The inset of (B) shows the imaginary part of Green's function in a large range of $i\mu_m$.

self-energy. By contrast, off the Fermi surface, if $i\nu_m$ is very small, both nonzero $E_{\vec{k}}$, as defined in Equation (3.34) and $\Sigma_>(\vec{k}, i\nu_m)$ determine the value of Green's function. The results demonstrated in the earlier part of this section indicate that the magnitude of $\Sigma_>(\vec{k}, i\nu_m)$ is much smaller than $E_{\vec{k}}$. Therefore, the difference between the non-interacting and interacting Green's function at momenta off the Fermi surface are very small. Figure 4.8(B) and 4.9(B) illustrate this behavior of the off-Fermi surface Green's function.

Figure 4.7 shows the Green's function on the Fermi surface at a variety of temperatures computed by both second- and fourth-order approximation. At high temperature case ($T = 1.0t_1$), the Green's function values calculated by different orders of approximation do not differ from each other too much. In contrast, at relatively lower temperature ($T = 0.2t_1$), the first, second and fourth approximation causes noticeable differences of the corresponding Green's function on Fermi surface, because the magnitude of the lowest Matsubara frequencies is much smaller than those of the corresponding self-energies, hence the self-energy dominates. The difference caused by orders of approximation are obvious. For example, the maximum value is more suppressed in the higher order approximation due to the larger self-energies on the Fermi surface correspondingly. Off the Fermi surface, for example, Figure 4.8 and Figure 4.9, one can observe that the difference between various order of approximations is unrecognized.

At low temperature, for the particle-hole symmetric Hubbard model, the temperature dependence of the imaginary frequency Green's function $G(\vec{k}, i\nu_m)$ is significant if momentum $\vec{k}$ is on the Fermi surface, but is weak if momentum $\vec{k}$ is off the Fermi surface. The Dyson equation, Equation (3.12), shows that

$$G(k) = [i\nu_m - \epsilon_{\vec{k}} + \mu - \Sigma^{(1)}(k) - \Sigma_>(k)]^{-1}.$$

Due to the particle-hole symmetry property, $\mu = \Sigma^{(1)} = U/2$, according to Equation (3.93). Then the Green's function can be written as

$$G(k) = [i\nu_m - \epsilon_{\vec{k}} - \Sigma_>(k)]^{-1}.$$

If $\vec{k}$ is on the Fermi surface, $\epsilon_{\vec{k}} = 0$ as required. At low temperature, according to Equation (4.1), the Green's function $G(k)$ is determined by $\Sigma_>(k)$ at different temperature. On the other hand, if $\vec{k}$ is off the Fermi surface, $\epsilon_{\vec{k}} \neq 0$. If the square lattice size is finite, such as 4×4 or 8×8, $\epsilon_{\vec{k}}$ can be much larger than $\Sigma_>(k)$, and thus dominates the value of the Green's function $G(k)$ at low Matsubara frequency range. For example, for a 4×4 square lattice, if $\vec{k}$ is off the Fermi surface, $\epsilon_{\vec{k}}$ can have 4 different values, -4, -2, 2 and 4, by Equation 2.14. According to Figure 4.3, when $|i\nu_m|$ is comparable to or smaller than $|\Sigma_>(k)|$, $|\Sigma_>(k)|$ is much smaller than 2, the smallest possible value of $\epsilon_{\vec{k}}$ if $\vec{k}$ is off the Fermi surface. Therefore, if $\vec{k}$ is off the Fermi surface, the value of the Green's function $G(\vec{k}, i\nu_m)$ has small differences at different temperatures.

The particle-hole symmetry property of the Green's function is shown in these figures as well. The real part of the Green's function for two momenta differing in $\vec{K} = (\pi, \pi)$, $\vec{k} = (0, 0)$ and $\vec{k} = (\pi, \pi)$, in Figure 4.8 an Figure 4.9, are negatives of each other, i.e., they obey the particle-hole symmetric relations given by Equation (3.88) and (3.88), while the imaginary parts of the Green's function of these two momenta are exactly the same. On the Fermi surface (Figure 4.7), the real part of the Green's function is zero, as required by particle-hole symmetry Equation (3.88), since $\vec{k}_F + \vec{K} = -\vec{k}_F$ (modulo a reciprocal lattice vector) on the particle-hole symmetric Fermi surface.

As the spectral weight function is calculated from the imaginary frequency Green's function data, we expect that the order of approximation will not affect the value of spectral weight off the Fermi surface significantly, but will cause significant differences on the Fermi surface.

4.4 Single-particle Spectral Weight $A(\vec{k}, \omega)$

Let us first consider the single-particle Green's function $G(\vec{k}, i\nu_m)$ and single-particle spectral weight function $A(\vec{k}, \omega)$ in the first order approximation, $n_{max} = 1$. In this approximation ($n_{max} = 1$), $G(\vec{k}, i\nu_m)$ and $A(\vec{k}, \omega)$ are identical to the non-interacting $G(\vec{k}, i\nu_m)$ and

$A(\vec{k},\omega)$, calculated at the same electron occupancy $\langle n\rangle$. The only difference between the non-interacting and first-order approximation is a shift in the chemical potential. The chemical potential μ for the interacting system treated in the first-order approximation is

$$\mu = \mu^{(0)} + \Sigma^{(1)}, \tag{4.1}$$

where

$$\Sigma^{(1)} = \frac{1}{2}U\langle n\rangle, \tag{4.2}$$

and $\mu^{(0)}$ is the corresponding non-interacting chemical potential for same occupancy $\langle n\rangle$. Hence,

$$A(\vec{k},\omega) = \delta(\omega - E_{\vec{k}}), \tag{4.3}$$

where the quasiparticle band energy

$$E_{\vec{k}} = \epsilon_{\vec{k}} - (\mu - \Sigma^{(1)}) = \epsilon_{\vec{k}} - \mu^{(0)}. \tag{4.4}$$

In the particle-hole symmetric case, at band-filling $\rho_e = \frac{1}{2}$, the spectral function $A(\vec{k},\omega)$, with $\vec{k}_F$ on the particle-hole Fermi surface, has a delta function peak exactly at $\omega = 0$. For momentum $\vec{k}$ off the Fermi surface, the quasiparticle peak disperses with $\vec{k}$, i.e., its peak position $E_{\vec{k}}$ varies with $\vec{k}$.

For approximation orders $n_{max} \geq 2$, the imaginary-frequency single-partlce Green's functions $G(\vec{k}, i\nu_m)$ obtained from Monte Carlo summation were transformed to spectral weight functions $A(\vec{k},\omega)$ by the maximum entropy method.

Let us turn to the second order approximation, $n_{max} = 2$. The single-particle spectral weight function $A(\vec{k},\omega)$ for $\vec{k}$ on and near the Fermi surface consists of a sharp peak, which is the so-called "quasiparticle peak", and a broader peak, the so-called "incoherent side band". These interaction-broadened quasiparticle peaks evolve from the sharp $\delta(\omega - E_{\vec{k}})$ quasiparticle peak of the non-interacting system as the interaction (U) is turned on. The main effects of the interaction are to broaden the δ-function quasiparticle peaks to a finite width,

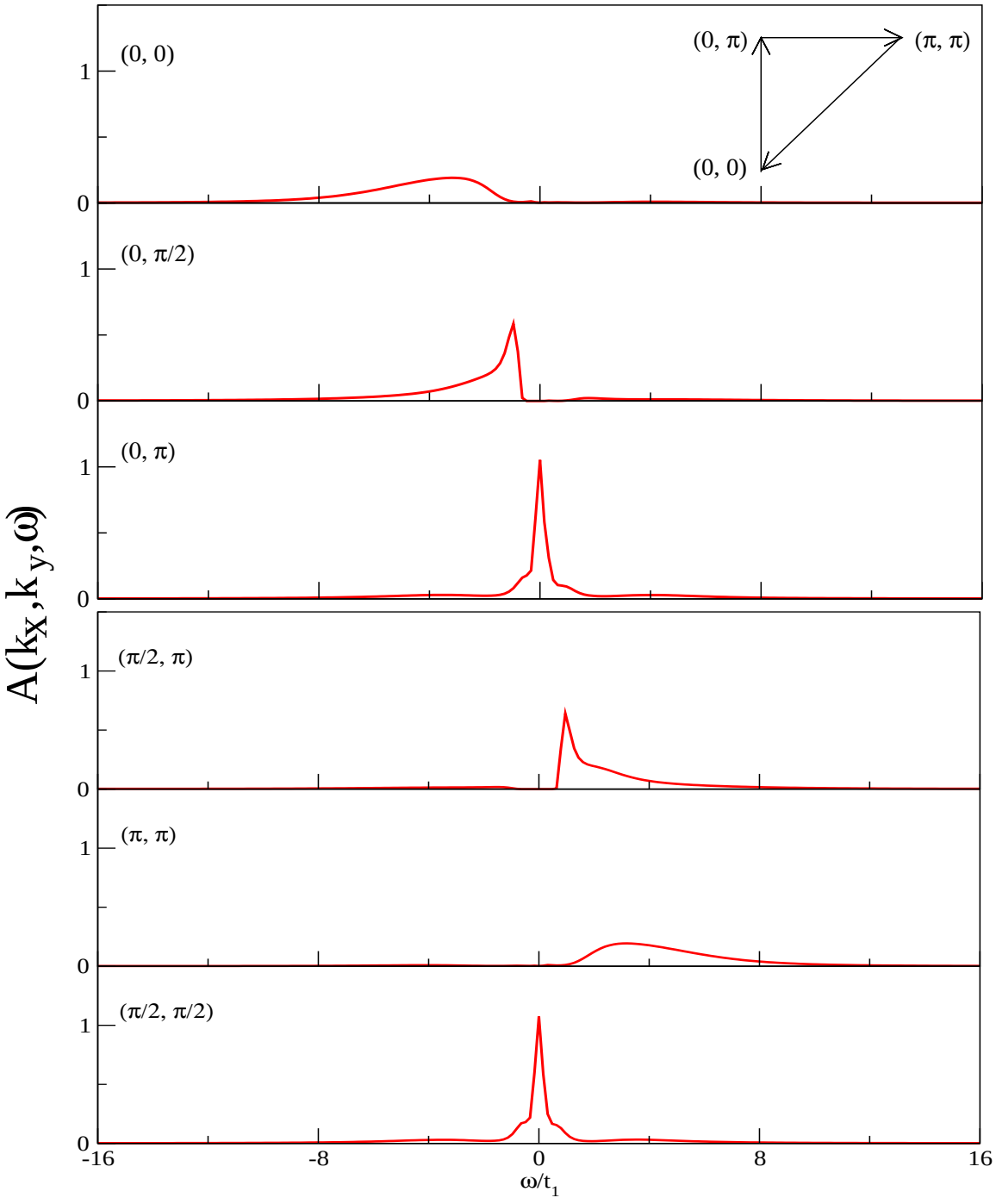

Figure 4.10: Spectral weight function $A(\vec{k},\omega)$ for a Hubbard system on a 4×4 lattice in particle-hole symmetry with t_1 and $U = 8.0t_1$ at $T = 0.05t_1$. The spectral weight function $A(\vec{k},\omega)$ is computed from the imaginary-frequency Green's function $G(k)$, which is calculated by the second order approximation. The momentum $\vec{k}$ goes through $(0,0)$,$(0,\pi/2)$,$(0,\pi)$,$(\pi/2,\pi)$,(π,π) and $(\pi/2,\pi/2)$.

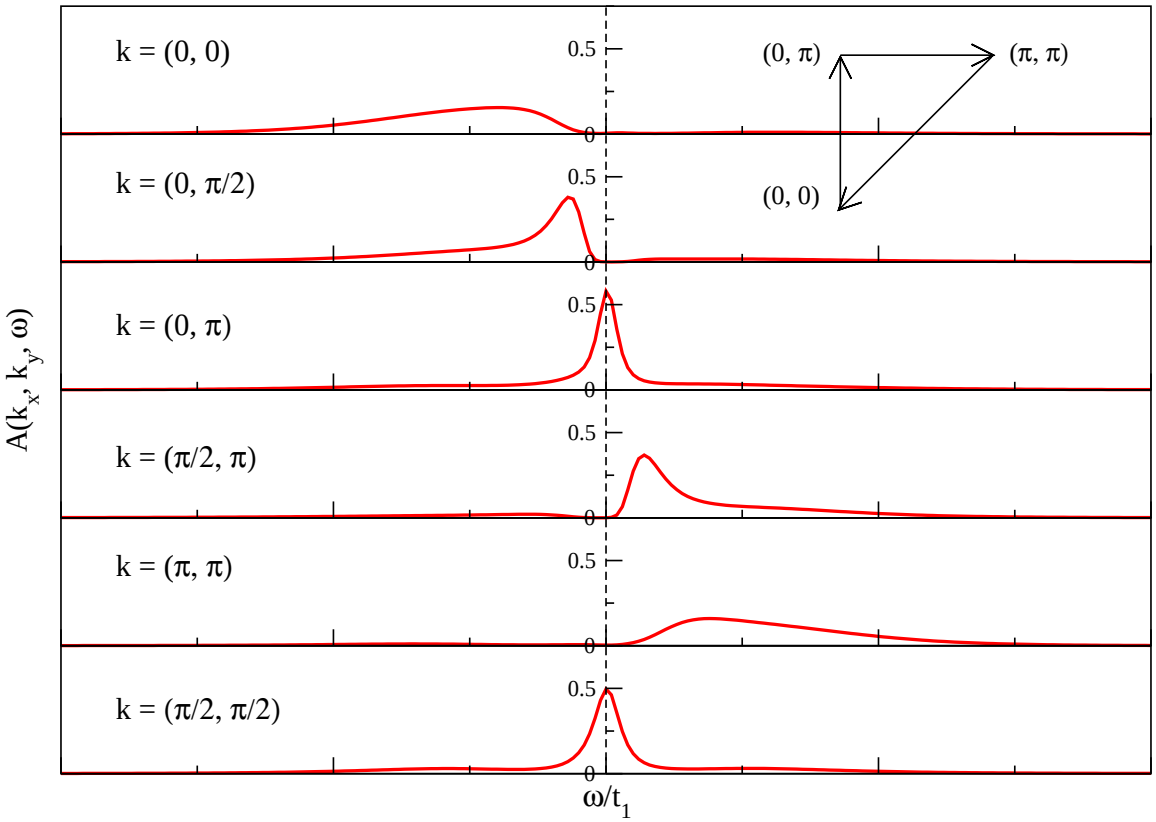

Figure 4.11: Spectral weight function $A(\vec{k},\omega)$ for the Hubbard model on a 4×4 lattice in particle-hole symmetry with t_1 and $U = 8.0t_1$ at $T = 0.2t_1$. The spectral weight function $A(\vec{k},\omega)$ is computed from the imaginary-frequency Green's function $G(k)$, which is calculated in the fourth-order diagrammatic approximation $n_{max} = 4$. The momentum $\vec{k}$ goes through $(0,0)$,$(0,\pi/2)$,$(0,\pi)$,$(\pi/2,\pi)$,(π,π) and $(\pi/2,\pi/2)$.

to reduce their (integrated) spectral weight, and "flatten" their dispersions as discussed in the next section. In addition, the interactions cause the formation of the incoherent side bands mainly at the larger energies beyond the quasiparticle peaks, i.e, for $|\omega| > |E_{\vec{k}}|$. These incoherent side bands contain the "missing" spectral weight that has been removed from the quasiparticle peaks by the interaction, so that the total sum rule, $\int d\omega A(\vec{k},\omega) = 1$ (Equation (3.71)) remains satisfied. For momenta $\vec{k}$ far from the Fermi surface and sufficiently strong interaction U, the quasiparticle peaks are so strongly broadened and/or reduced in spectral weight that they become indistinguishable from the incoherent side band(s). This can be seen in Figure 4.10 for $\vec{k} = (0,0)$ and $\vec{k} = (\pi,\pi)$. Just as in the non-interacting system and first-order approximation, in the second-order approximation, the quasiparticle peak disperses with $\vec{k}$, as will be discussed in more detail in the next section. We notice also that our numerical results for $A(\vec{k},\omega)$ obey reasonably well the particle-hole symmetry requirements, i.e.,

$$A(\vec{k}+\vec{K},\omega) = A(\vec{k},-\omega)$$

with $\vec{K} = (\pi,\pi)$ for particle-hole-transformation-related $\vec{k}$-points, $\vec{k}$ and $\vec{k}+\vec{K}$, such as $\vec{k} = (0,0)$ and $\vec{k} = (\pi,\pi)$ or $\vec{k} = (0,\pi/2)$ and $\vec{k} = (\pi/2, pi)$. This is an important check on the numerical accuracy of the Monte Carlo code and the maximum entropy method analytic continuation procedure.

Figure 4.12 compares the spectral weight functions of the Hubbard model at half-filling in the second order approximation at different temperatures. At higher temperature $T > 0.1t_1$, the quasiparticle peak and the incoherent side band for the on-Fermi-surface $\vec{k}$-vector, in Figure 4.12(A), are essentially indistinguishable due to the large width of the quasiparticle peak. However, as the temperature is lowered, the quasiparticle peak narrows. We can then see more clearly how distinct incoherent side bands develop that are clearly separated from the quasi-particle peak, as the temperature is lowered. The incoherent side bands can be clearly distinguished from the quasiparticle peak at at $T = 0.05t_1$, though the side bands are not very strong.

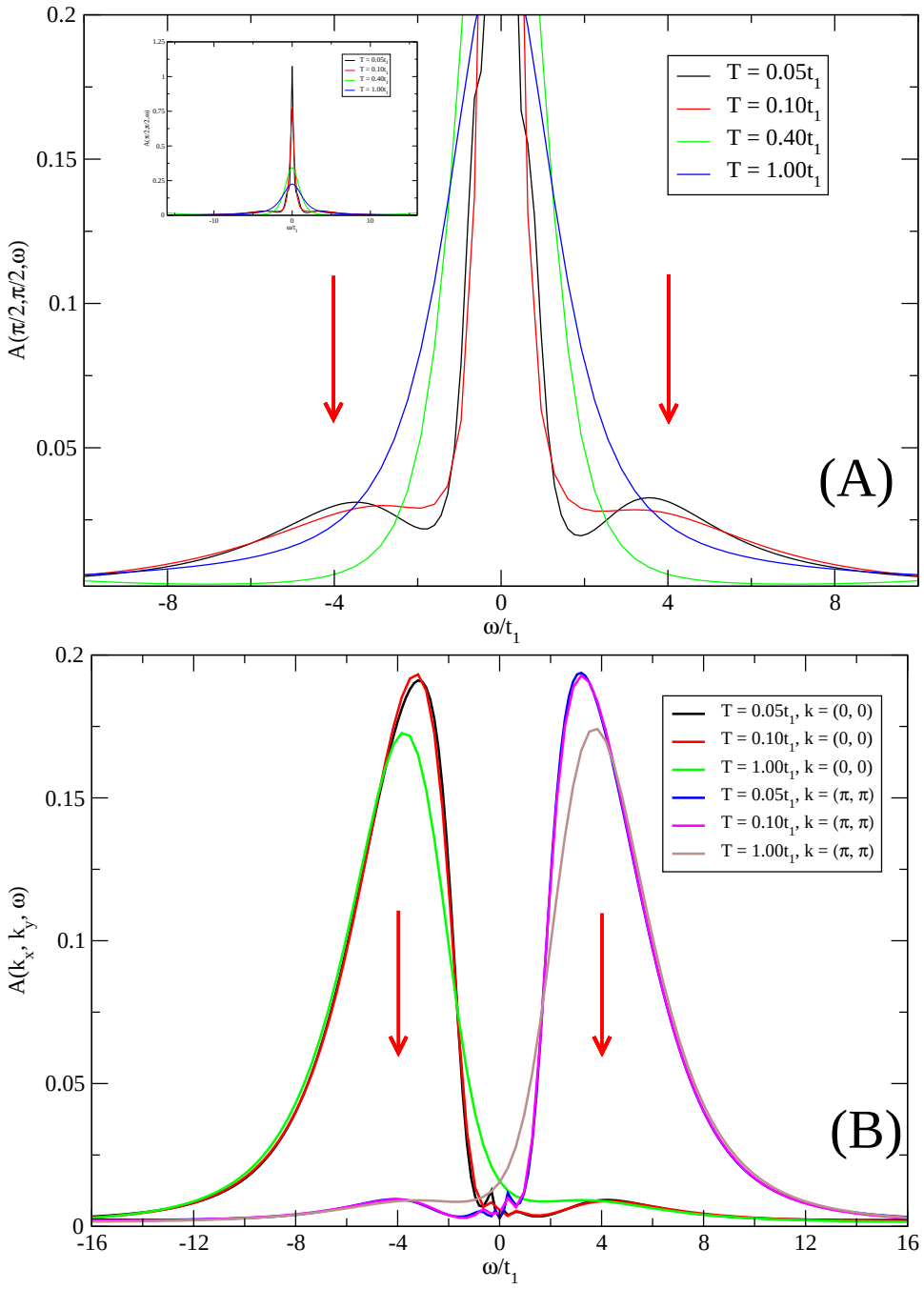

Figure 4.12: Spectral weight function $A(\vec{k},\omega)$ for a Hubbard system on a 4×4 lattice in particle-hole symmetry with t_1 and $U = 8.0t_1$ (A) on the Fermi surface ($\vec{k} = (\pi/2,\pi/2)$ (B) off the Fermi surface, calculated from imaginary frequency Green's function data computed by the second-order approximation. The inset of (A) is the spectral weight function of $\vec{k} = (\pi/2,\pi/2)$ shown in a large imaginary frequency range. The vertical red arrows indicate the positions of atomic limit Hubbard bands as shown in Figure 3.4. In (A), at $T = 0.05t_1$, the incoherence side bands can be seen around $\omega = \pm4$.

At low temperature, the spectral weight functions $A(\vec{k},\omega)$ for momentum $\vec{k}$ far from the Fermi suface show very little temperature dependence as expected from the results for $G(\vec{k},i\nu_m)$ off the Fermi surface. For example, in Figure 4.12(B), the spectral weight function $A(\vec{k},\omega)$, such that $\vec{k}=(0,0)$ or $\vec{k}=(\pi,\pi)$ at $T=0.10t_1$ is very close to spectral weight $A(\vec{k},\omega)$, with $\vec{k}=(0,0)$ or (π,π) respectively, at $T=0.05t_1$. This is because the spectral weight function is calculated from the imaginary frequency Green's function, and the imaginary-frequency Green's functions $G(\vec{k},i\nu_m)$ for $\vec{k}$, which is off the Fermi surface, have small differences at different temperatures, as we have already discussed in Section 4.3. Basically, for these far-off-Fermi-surface $\vec{k}$ vectors, the quasiparticle peak and the incoherent side band have merged at all temperatures, and cannot be clearly distinguished.

The displacement of spectral weight away from $\omega=0$ into the side bands at larger $|\omega|$ can be interpreted as the incipient development of the Mott-Hubbard gap. Note that the peak position of the side band corresponds closely to the position $\omega=\pm U/2$ of the lower and upper Hubbard band peaks in the atomic limit, as shown in Figure 3.4.

The spectral function of the Hubbard model is also affected by the orders of diagram approximation, n_{max}, used in the calculation, especially on the Fermi surface. Figure 4.13 shows the spectral function $A(\vec{k},\omega)$ of the particle-hole symmetric Hubbard model on a 4×4 lattice with $U=8t_1$. To see the significance of the fourth order diagrams' contribution, we compare the results for $A(\vec{k},\omega)$ in the second order simulation ($n_{max}=2$) and the fourth order simulation ($n_{max}=4$). For instance, at $T=0.2t_1$, the quasiparticle peak of the spectral weight function $A(\vec{k}_F,\omega)$ for on-Fermi-surface momentum $\vec{k}_F$ calculated by the fourth order approximation has less spectral weight and is somewhat broader than the quasiparticle peak of $A(\vec{k}_F,\omega)$ calculated by the second-order approximation. Otherwise, the difference of approximation orders doesn't make a dramatic change on the spectral weight function. At high temperature, such as $T=1.0t_1$, the difference is even less significant.

For momenta $\vec{k}$ far from the Fermi surface, the spectral weight function $A(\vec{k},\omega)$ is also weakly dependent on the order of approximation. The main effect of including the the fourth-

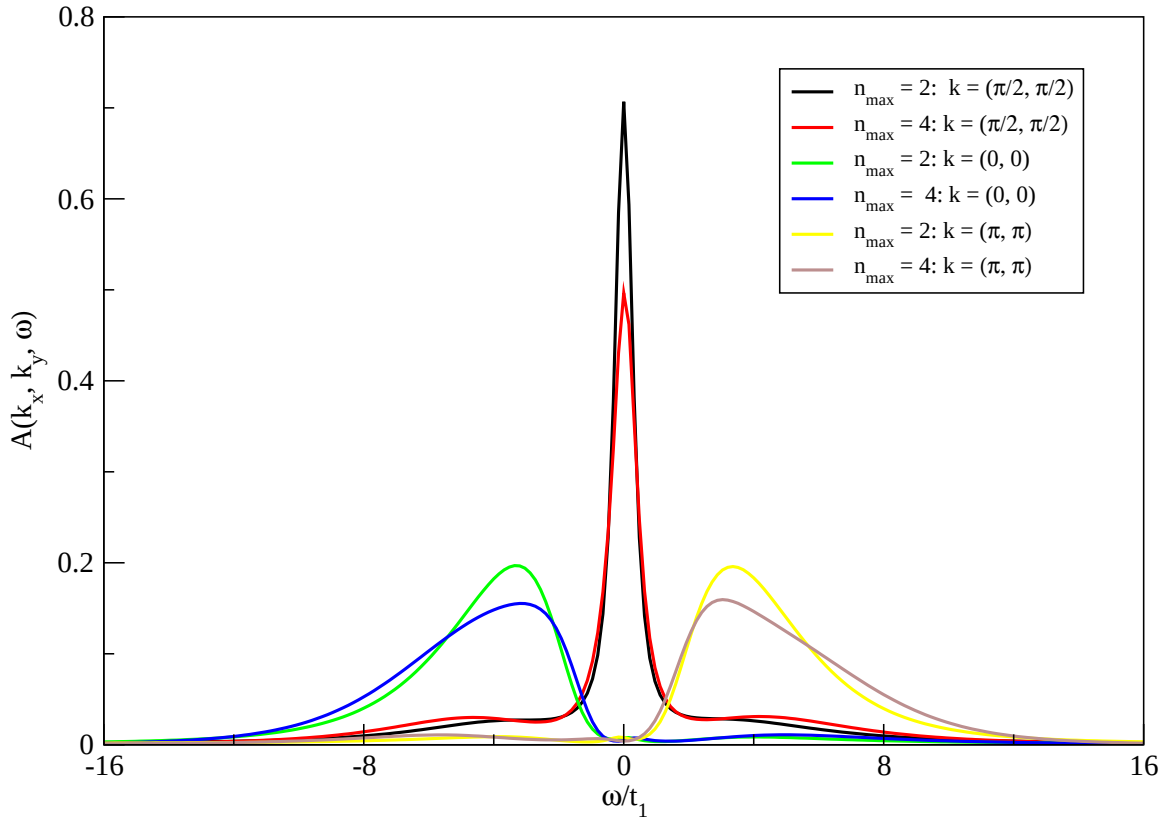

Figure 4.13: A comparsion is made between the Hubbard model's spectral weight function $A(\vec{k},\omega)$ calculated from second-order approximation data and $A(\vec{k},\omega)$ from fourth-order approximation data. The simulation is performed on a 4×4 square lattice, with on-site interaction $U = 8t_1$ and chemical potential $\mu = U/2$, at $T = 0.2t_1$.

order diagrams to the two-dimensional Hubbard model is to broaden somewhat the corresponding spectral peaks in $A(\vec{k},\omega)$.

However, it is important to notice that including the higher order ($n_{max} = 4$) diagrams does move the results in the right direction, as far as the formation of a Mott-Hubbard gap is concerned. Namely, including the fourth-order diagrams reduces the quasiparticle spectral weight at $\omega = 0$ for on-Fermi-surface $\vec{k}$-vectors, $\vec{k}_F$, and pushes the spectral weight to the higher energies $|\omega|$, i.e., into the incoherent side bands. That is qualitatively the type of spectral weight redistribution required for the Mott-Hubbard gap formation.

Our results for the second- or fourth-order self-consistent diagram approximation to the two-dimensional Hubbard model ($n_{max} = 2$ or $n_{max} = 4$ respectively) at low temperature clearly exhibit all the expected characteristics of a Fermi liquid [27] as described by Equation (D.4). First, when the momentum vector $\vec{k}$ moves towards the Fermi surface, as shown in Figure 4.10 and Figure 4.11 respectively, the peak of $A(\vec{k},\omega)$ becomes sharper; whereas the peak of $A(\vec{k},\omega)$ gets broadened when $\vec{k}$ moves away from the Fermi surface. Second, for $\vec{k}$ on the Fermi surface, as shown in Figure 4.12. as the temperature is lowered, the quasiparticle peak of $A(\vec{k},\omega)$ gets sharper. This behavior is consistent with Luttinger's fundamental proof [25][26][27] that any finite-order self-consistent diagram approximation to an interacting Fermion system with translation invariance in the infinite system limit $N \to \infty$ obeys Fermi liquid theory for $T \to 0$. Therefore, at any finite approximation order n_{max}, our diagrammatic approximation scheme will always lead to Fermi liquid behavior, for any band filling ρ_e with $0 < \rho_e < 1$, including $\rho_e = 1/2$, if we take the limit $N \to \infty$ and then study the system asymptotically in the low-temperature limit $T \to 0$. Fermi liquid behavior implies that the system would be metallic and therefore would not exhibit the Mott-Hubbard insulator behavior. However, it is still possible that, without violating the Luttinger theorem, the physically expected Mott-Hubbard insulator behavior can be recovered from our Fermi-liquid approximation scheme by going to higher approximation orders. This would require that the quasiparticle peak spectral weight for $\vec{k}$-points on or near the Fermi surface decreases to zero,

as the approximation order n_{max} is systematically increased to infinity. Qualitatively, this is indeed what we find in our comparison of the second- and fourth-order results of $A(\vec{k},\omega)$ discussed above: the quasiparticle spectral weight for $\vec{k}$ on the Fermi surface is reduced in going from the second- to the fourth-order. However, this quasiparticle peak spectral weight reduction is rather weak and it indicates that one may have to go to even higher order n_{max} to see a substantial further reduction that would approximate the Mott-Hubbard gap behavior.

4.5 Dispersion

It is also of great interest to study how the quasiparticle dispersion is affected by the interaction. To do this, we now define the interacting quasiparticle energy $E_{\vec{k}}$ as the frequency $\omega = E_{\vec{k}}$ of the largest peak in $A(\vec{k},\omega)$. For $n_{max} = 1$, $E_{\vec{k}} = \epsilon_{\vec{k}} - \mu^{(0)}$, as discussed in Section 4.4. For $n_{max} \geq 2$, we get $E_{\vec{k}}$ numerically from the spectral weight function $A(\vec{k},\omega)$, which is calculated from the imaginary-frequency Green's function data by the maximum entropy method.

From our result, shown in Figure 4.14, with each lattice momentum $\vec{k}$, one can see that the quasiparticle band $E(\vec{k})$ is flatter than the non-interacting band. This quasiparticle band flattening becomes more pronounced as we lower the temperature, i.e., more precisely:

$$|E_{\vec{k}}(T = 0.5)| \leq |E_{\vec{k}}(T = 0.8)| \leq |\epsilon_{\vec{k}}| \tag{4.5}$$

where the equality occurs only at $\epsilon_{\vec{k}} = 0$. In other words, the quasiparticle band is flattened by the interaction and this flattening becomes more pronounced as we lower the temperatures. The flattening of the quasiparticle band can be interpreted as a "mass-enhancement", since it implies that at a given momentum $\vec{k}$, the quasiparticle velocity is reduced. The quasiparticle's velocity is defined as

$$\vec{v}_{QP} = \frac{\partial \tilde{E}}{\partial \vec{k}}, \tag{4.6}$$

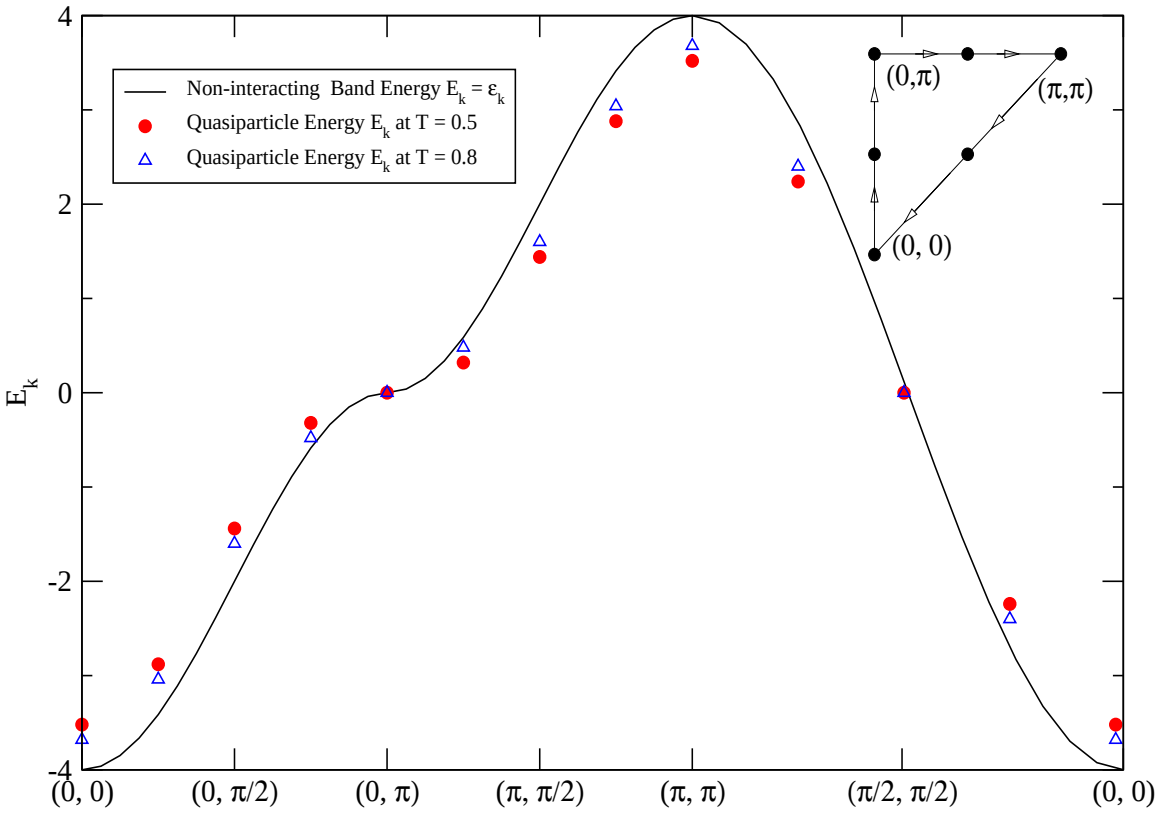

Figure 4.14: Quasiparticle energy $E_{\vec{k}}$ of the interacting system compared to the non-interacting band energy $E_{\vec{k}} = \epsilon_{\vec{k}}$ along $\Gamma \rightarrow \mathrm{X} \rightarrow \mathrm{Z} \rightarrow \Gamma$, tested on an 8×8 square lattice with $U = 8t_1$ and $\mu = U/2$ by second order approximation.

and the quasiparticle mass enhancement corresponds to having a mass-enhancement factor

$$Z_{\vec{k}} = \frac{|\vec{v}_0(\vec{k})|}{|\vec{v}_{QP}(\vec{k})|} > 1 \tag{4.7}$$

where $\vec{v}_0(\vec{k})$ is the non-interacting quasiparticle's velocity, given by

$$\vec{v}_0(\vec{k}) = \frac{\partial \epsilon_{\vec{k}}}{\partial \vec{k}}$$

Within the framework of Fermi liquid theory, the mass enhancement on or near the Fermi surface is related to the reduction in the spectral weight under the quasiparticle peak in $A(\vec{k}, \omega)$, such that $1/Z_{\vec{k}}$ equals the fraction of spectral weight of the quasiparticle peak, according to Equation (D.6). If the development of the Mott-Hubbard gap Δ is indeed accompanied by a gradual disappearance of the quasiparticle spectral weight on and near the Fermi surface, then this should also be seen in a gradual divergence of the mass enhancement factor $Z_{\vec{k}} \to \infty$, i.e., in a very severe flattening of the quasiparticle band near the Fermi surface, as well as in a severe loss of spectral weight under the quasiparticle peak, given by $1/Z_{\vec{k}}$ according to Fermi liquid theory. As can be seen in Figure 4.14, as well as Figure 4.12 and Figure 4.13, the mass enhancement is only about $Z_{\vec{k}} = 1.14$ near $\vec{k}_F = (0, \pi)$, $(\pi, 0)$ and about $Z_{\vec{k}} = 1.26$ near $\vec{k}_F = (\pi/2, \pi/2)$. This is much weaker than the large $Z_{\vec{k}} \gg 1$ one should expect in the range $T < \Delta$ where the Mott-Hubbard gap should start to form with Δ of the order of U.

4.6 Density of States

The density of states $D(\omega)$ of the two-dimensional Hubbard model is calculated from the single particle spectral weight function $A(\vec{k}, \omega)$ by Equation (3.80).

Figure 4.15 compares $D(\omega)$ of a 4×4 particle-hole symmetric Hubbard model at different temperatures. At high temperature, for example, $T = 1.0t_1$ and $0.4t_1$, the density of states is a broadened smooth Gaussian-like curve centered on zero frequency. As the temperature decreases, more and more weight is shifted to the higher frequency range. Two side peaks

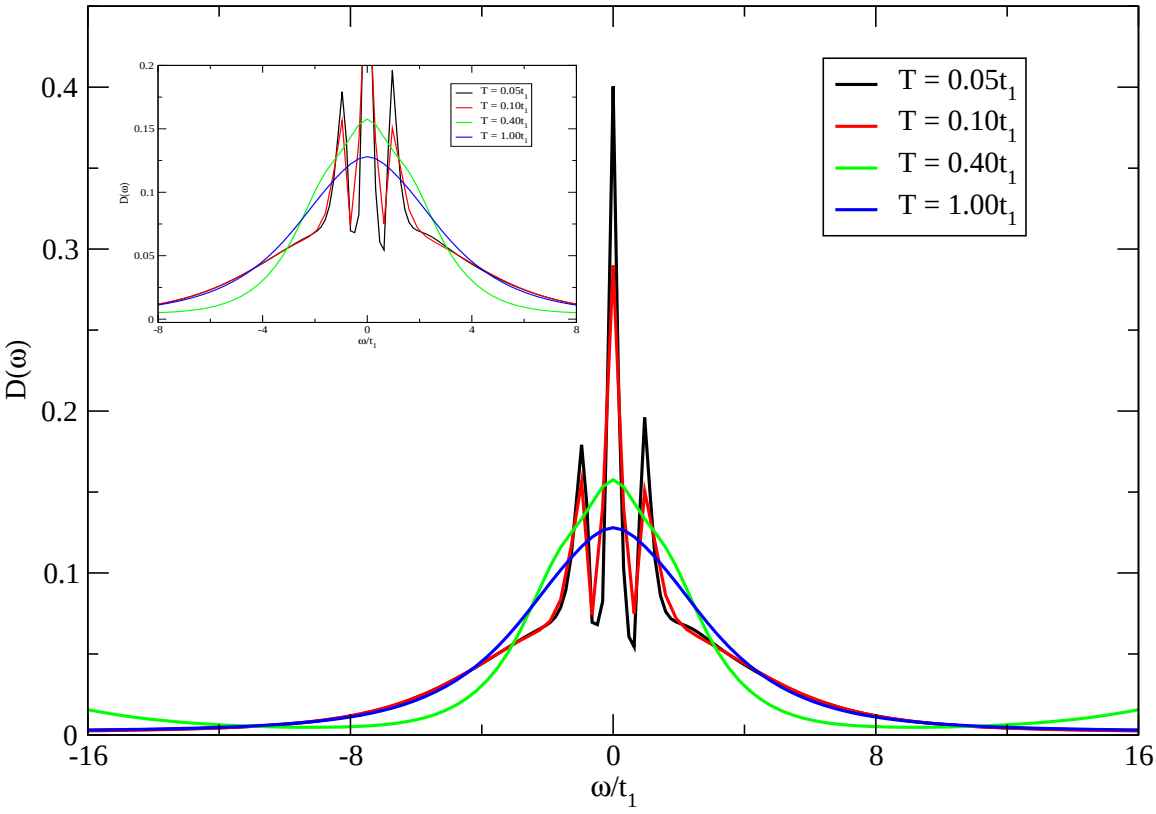

Figure 4.15: The density of states $D(\omega)$ of the Hubbard model on a 4×4 lattice with $U = 8.0t_1$ and $\mu = U/2$. The inset emphasizes the difference between $D(\omega)$ of various temperatures' in details. The results shown comes from the imaginary frequency Green's function $G(\vec{k}, i\nu_m)$, which is calculated by second-order approximation. The insets of (A) and (B) are the comparison in a larger range of ω.

start to appear as the temperature is lowered to $0.1t_1$, and are obvious at $T = 0.05t_1$. The density of states looks like the sum of several smeared delta functions, which is not the same as White's exact quantum Monte Carlo result [3], in which a very strong depression of spectral weight appears at the center around $\omega = 0$ (low frequency). It is reasonable to expect that at even lower temperature the density of states may be strongly suppressed in our diagram approximation. Zlatić's spectral weight function at half-filling is also peaked at zero-frequency. There is an interesting phenomenon that most of the perturbation approaches generate a delta-function-like sharp peak on the Fermi surface, but the exact quantum Monte Carlo method yields a gap-like depression.

Just as for the single particle spectral weight function $A(\vec{k}, \omega)$, the density of states of Hubbard model $D(\omega)$ depends on the the order of the diagrammatic approximation n_{max} Figure 4.16 compares the density of states $D(\omega)$ calculated by second-order approximation with the $D(\omega)$ calculated by fourth-order approximation. The peak at $\omega = 0$ in $D(\omega)$, which corresponds to the quasiparticle peak of $A(\vec{k}_F, \omega)$ for on-Fermi-surface $\vec{k}$-vector, is suppressed with higher order diagrammatic approximation, whereas, the side peaks at $\omega \neq 0$ in the $D(\omega)$, which correspond to the quasiparticle peaks of $A(\vec{k}, \omega)$ for off-Fermi-surface $\vec{k}$-vectors, show less dependence on the order of diagrammatic approximation. Qualitatively, the inclusion of the higher order ($n_{max} = 4$) produces the results as expected for the formation of the Mott-Hubbard gap, i.e., the spectral weight at low ω ($|\omega| < U/2$) is suppressed by the higher order ($n_{max} = 4$) correction.

The lattice size is also a factor that affects the system property. There are more discrete $\epsilon_{\vec{k}} \in \mathcal{B}_L$ in a larger lattice size. This of course affects the density of states $D(\omega)$, even for the non-interacting system, according to Equation (3.80). Due to the limitation on CPU time, we've only completed the calculation of self-energy on an 8×8 lattice at temperature $T = 0.5t_1$ and $0.8t_1$, which are not sufficiently low. From the density of states of an 8×8 lattice at half-filling (Figure 4.17) and its comparison to those for another similar system, but on a 4×4 lattice at high temperature, the size effect on the density of states is not

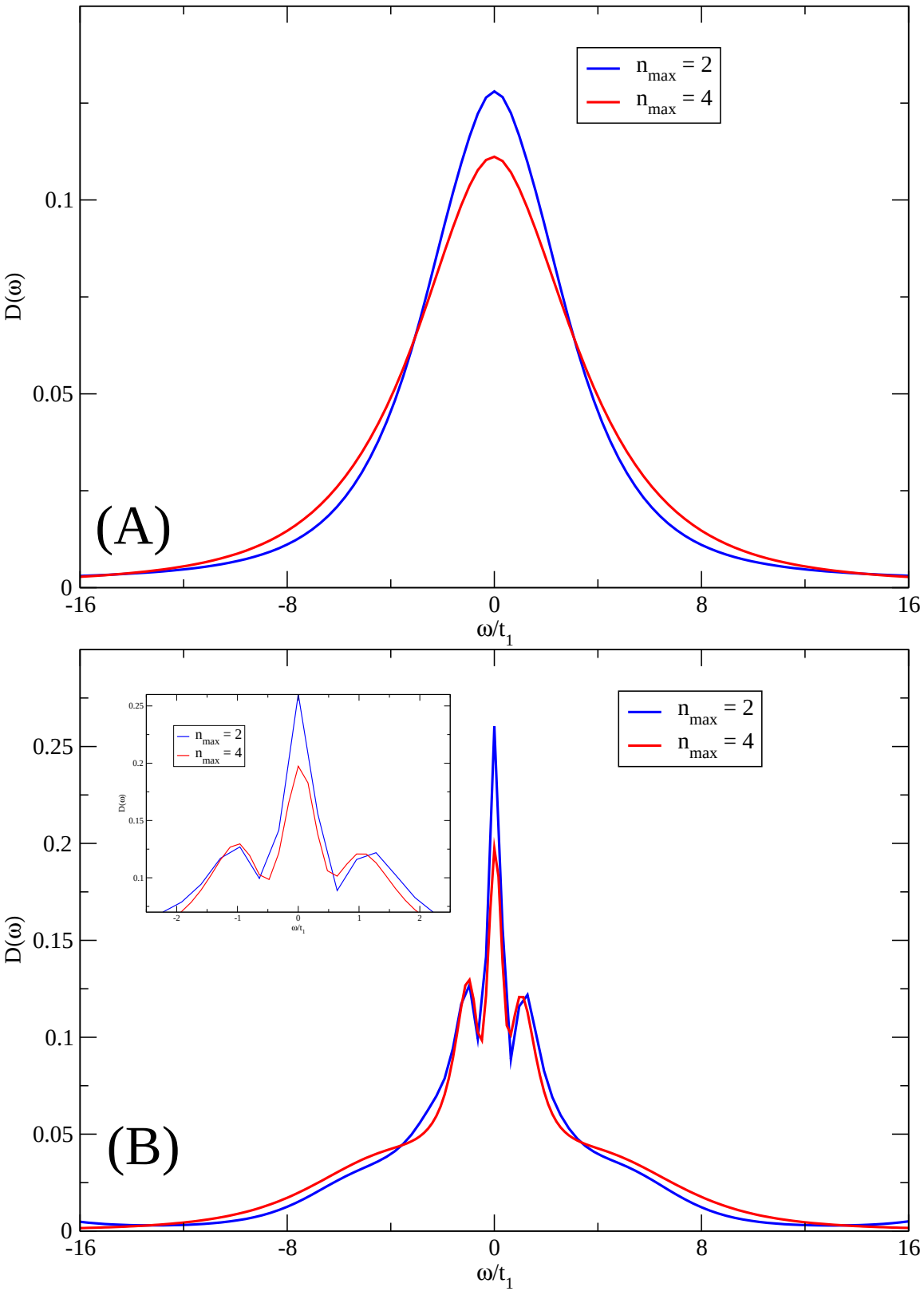

Figure 4.16: Comparison of density of states with second- or fourth-order approximation on a 4×4 square lattice, whose on-site repulsion U is $8t_1$ and μ is $U/2$, at (A) $T = 1.0t_1$ and (B) $T = 0.2t_1$. The insets of (B) shows the difference of the density of states between second- and fourth-order difference in detail.

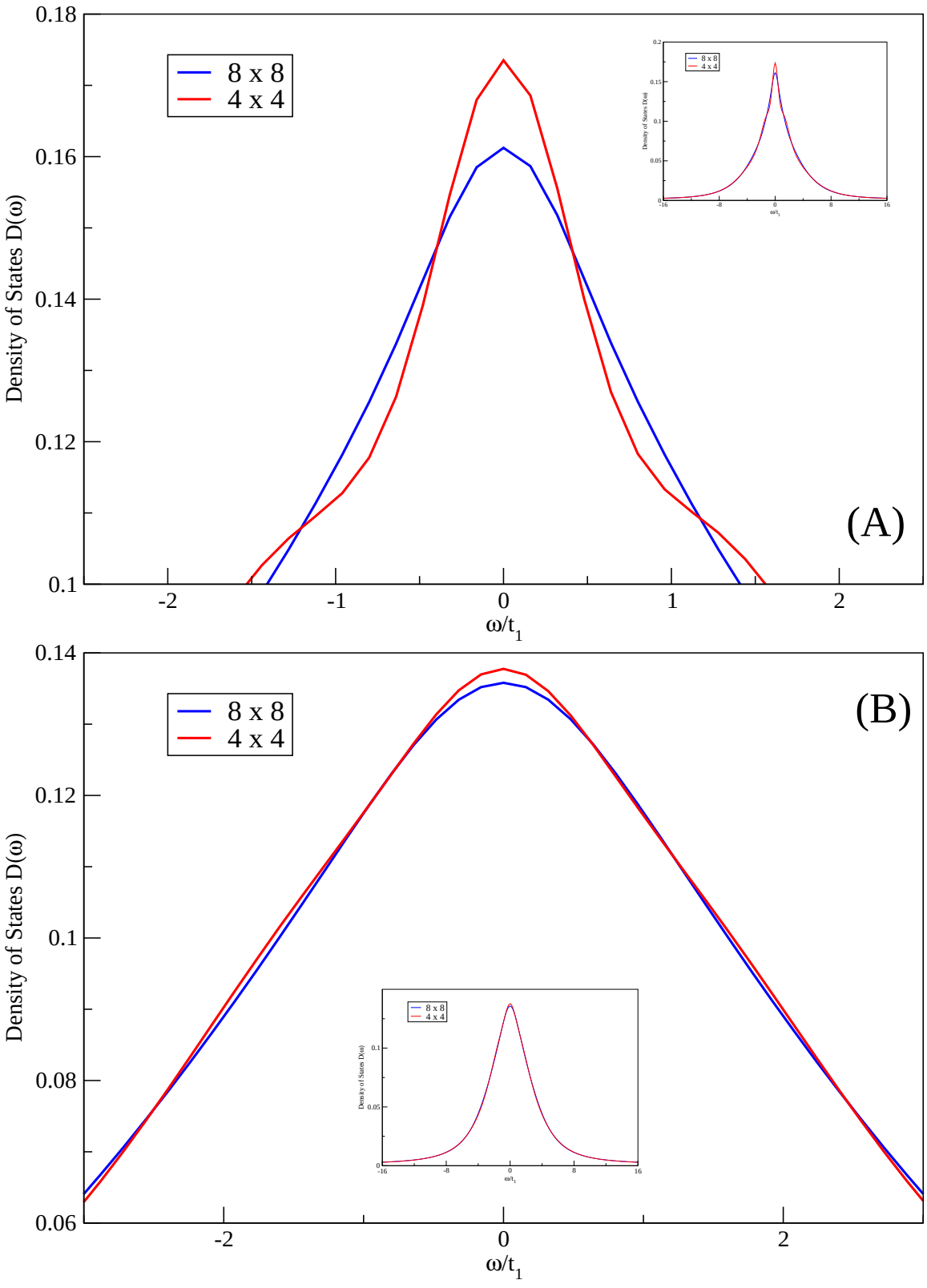

Figure 4.17: The comparison of the density of states on various sizes of Hubbard model, 8×8 and 4×4, with $U = 8t_1$ and $\mu = U/2$, at (A) $T = 0.5t_1$ (B) $T = 0.8t_1$

obvious. However, as expected from the non-interacting case, the finite size effect increases with decreasing temperature T. More extensive studies at lower T and larger lattices will be required to further explore the finite size dependence.

This finite size dependence is in contrast with the results obtained by the deterministic quantum Monte Carlo at the same temperature. In the quantum Monte Carlo results [3], a strong finite size dependence is found and the gap depression of the density of states becomes surprisingly less pronounced as the lattice size is increased from 4×4 to 8×8 (one needs to notice that this quantum Monte Carlo result was obtained with interaction $U = 4t_1$, i.e, not same as our model configuration $U = 8t_1$ which is shown in Figure 4.17).

On-site repulsive interaction U is another parameter that affects the spectral properties of the Hubbard model. The results, shown in Figure 4.18, were obtained on the 4×4 particle-hole symmetric lattice with on-site interaction $U = 12t_1$. The shape of the corresponding density of states is quite similar to that with $U = 8t_1$. Consistent with our expectation, the density of states is suppressed more with stronger interaction.

On the other hand, the self-consistent calculation has more difficulty to get a converged result with a larger on-site repulsive interaction. The difference is particularly apparent between $U = 8t_1$ and $U = 12t_1$.

We noticed that our solution for the density of states under low temperature at half-filling is quite similar to that of Gebhard for the infinite dimensional case at ground state [50] (Figure 8 and 9). In both of them, the DOS appears to have three peaks. The phenomenon is also observed by Georges and Kotliar [59] in the close to particle-hole symmetric half-filled case.

4.7 Integral Moments of The Spectral Function

We aslo calculated the integral moments from the spectral weight of the simulated results, and compare them with the corresponding analytical value (table 4.2 to table 4.5).

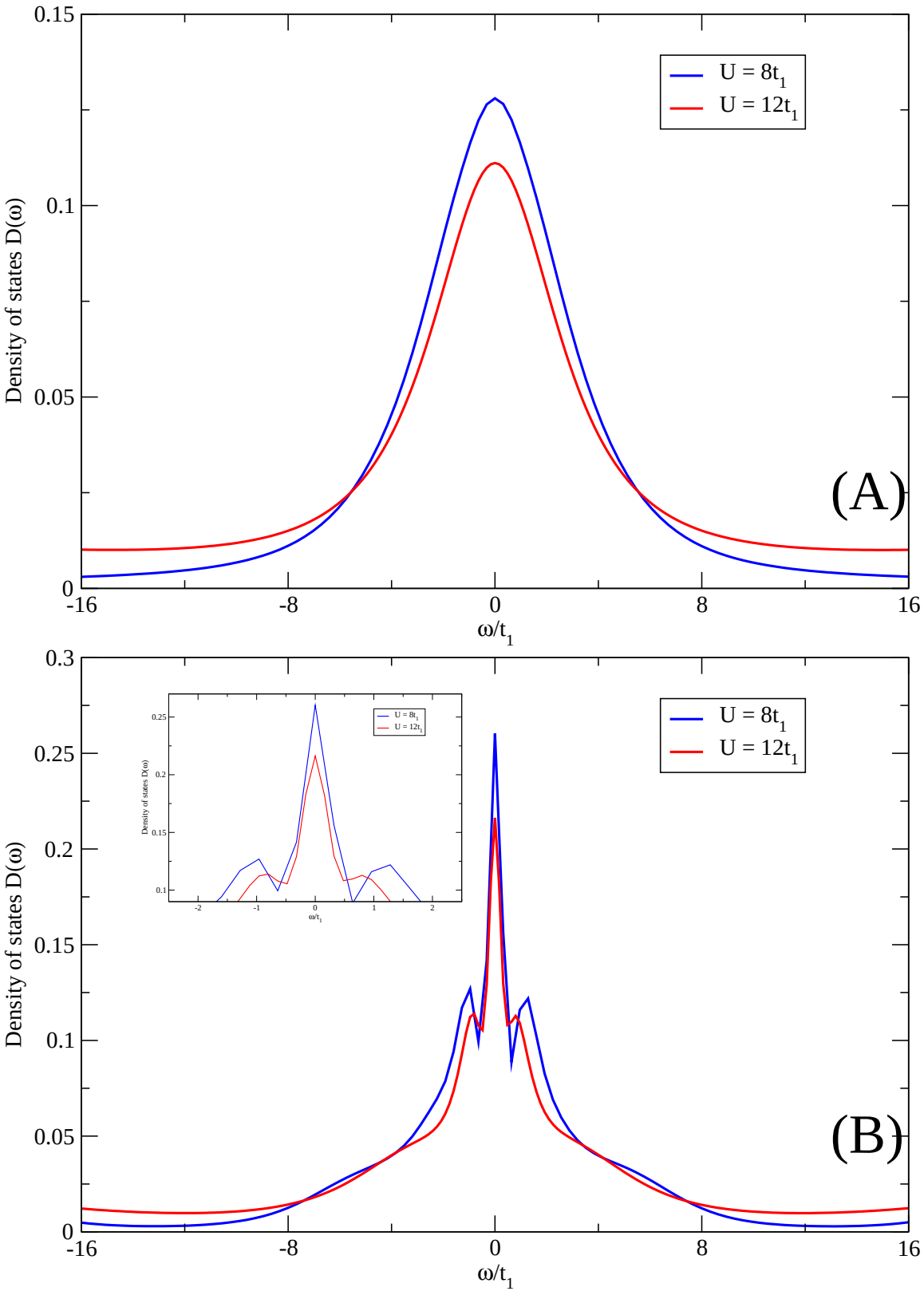

Figure 4.18: shows the density of states of Hubbard model on a 4×4 lattice with $U = 12t_1$, $\mu = U/2 = 6t_1$ and with $U = 8t_1$, $\mu = U/2 = 4t_1$ (A) at $T = 1.0t_1$ (B) at $T = 0.2t_1$.

$\vec{k}$	μ_1		
	exact value	2nd-order approximation	4th-order approximation
$(0,0)$	-4.00	-4.01	-4.03
$(0,\frac{\pi}{2})$	-2.00	-1.98	-2.00
$(0,\pi)$	-0.00	0.00	0.00
$(\frac{\pi}{2},\pi)$	2.00	1.98	2.00
(π,π)	4.00	4.00	4.03
$(\frac{\pi}{2},\frac{\pi}{2})$	0.00	0.00	0.00

Table 4.2: Comparison of μ_1 for Hubbard model on a 4×4 lattice with $U = 8.0t_1$, $\mu = 4.0t_1$ and $t_1 = 1.0t_1$ at $T = 1.0t_1$

$\vec{k}$	μ_2		
	exact value	2nd-order approximation	4th-order approximation
$(0,0)$	32.0	31.6	35.1
$(0,\frac{\pi}{2})$	20.0	19.9	23.0
$(0,\pi)$	16.0	16.5	19.3
$(\frac{\pi}{2},\pi)$	20.0	19.9	22.8
(π,π)	32.0	31.6	35.2
$(\frac{\pi}{2},\frac{\pi}{2})$	16.0	16.6	19.4

Table 4.3: Comparison of μ_2 for Hubbard model on a 4×4 lattice with $U = 8.0t_1$, $\mu = 4.0t_1$ and $t_1 = 1.0$ at $T = 1.0t_1$

$\vec{k}$	μ_1		
	exact value	2nd-order approximation	4th-order approximation
$(0,0)$	-4.00	-4.00	-3.99
$(0,\frac{\pi}{2})$	-2.00	-2.00	-1.98
$(0,\pi)$	-0.00	0.00	0.03
$(\frac{\pi}{2},\pi)$	2.00	1.99	2.02
(π,π)	4.00	4.00	4.04
$(\frac{\pi}{2},\frac{\pi}{2})$	0.00	0.00	0.03

Table 4.4: Comparison of μ_1 for Hubbard model on a 4×4 lattice with $U = 8t_1$, $\mu = 4t_1$ and $t_1 = 1.0$ at $T = 0.2t_1$

$\vec{k}$	μ_2		
	exact value	2nd-order approximation	4th-order approximation
$(0,0)$	32.0	31.5	33.7
$(0,\frac{\pi}{2)}$	20.0	19.5	21.6
$(0,\pi)$	16.0	15.4	17.7
$(\frac{\pi}{2},\pi)$	20.0	19.5	21.8
(π,π)	32.0	31.5	34.1
$(\frac{\pi}{2},\frac{\pi}{2})$	16.0	15.4	17.5

Table 4.5: Comparison of μ_2 for Hubbard model on a 4×4 lattice with $U = 8t_1$, $\mu = 4t_1$ and $t_1 = 1.0$ at $T = 0.2t_1$

$\vec{k}$	Percent Error of μ_2		
	$U = 8t_1$, $\mu = 4t_1$	$U = 12t_1$, $\mu = 6t_1$	$U = 16t_1$, $\mu = 8t_1$
$(0, 0)$	1.57	11.40	6.67
$(0, \frac{\pi}{2})$	2.40	13.96	12.02
$(0, \pi)$	3.62	14.72	14.64
$(\frac{\pi}{2}, \pi)$	2.34	13.61	12.05
(π, π)	1.64	11.13	6.62
$(\frac{\pi}{2}, \frac{\pi}{2})$	3.53	14.80	14.51

Table 4.6: The percent error (to the exact value) of μ_2 for second-order approximation computation with on-site repulsion U is $8t_1$, $12t_1$ and $16t_1$, respectively, and $\mu = U/2$, on a 4×4 Hubbard lattice with $t_1 = 1$ and $T = 0.2t_1$.

The zeroth order moments μ_0, at any approximation order n_{max}, will be exactly equal to 1, due to the fact that the asymptotic behavior $G(\vec{k}, i\nu_m) \cong 1/i\nu_m$, Equation (3.32), which is exactly preserved by the approximation. Table 4.2 (4.3) compare μ_1 (μ_2) obtained by second- ($n_{max} = 2$) and fourth order ($n_{max} = 4$) approximation. Both approximation orders perform well for μ_1 with at most 1% error. The error for μ_2 is a somewhat larger than the other two cases, especially the fourth order approximation. However, the results are acceptable considering the limited numerical accuracy of the MEM analytical continuation.

Table 4.6 also indicates that when on-site repulsion U is larger than or equal to $12t_1$, the second order approximation causes non-negligible errors (mostly larger than 10%) to the exact value. Hence a higher order truncation of the diagram series is essential.

4.8 Away from Particle-hole Symmetry

An alternative, equivalent way to search for the existence of a charge excitation gap is to calculate the occupation numbers $\langle n \rangle$ as a function of the chemical potential μ, and look for regions of μ where $\langle n \rangle$ is constant with changing μ, i.e., for a so-called "plateau" where

$$\frac{\partial \langle n \rangle}{\partial \mu} = 0 \tag{4.8}$$

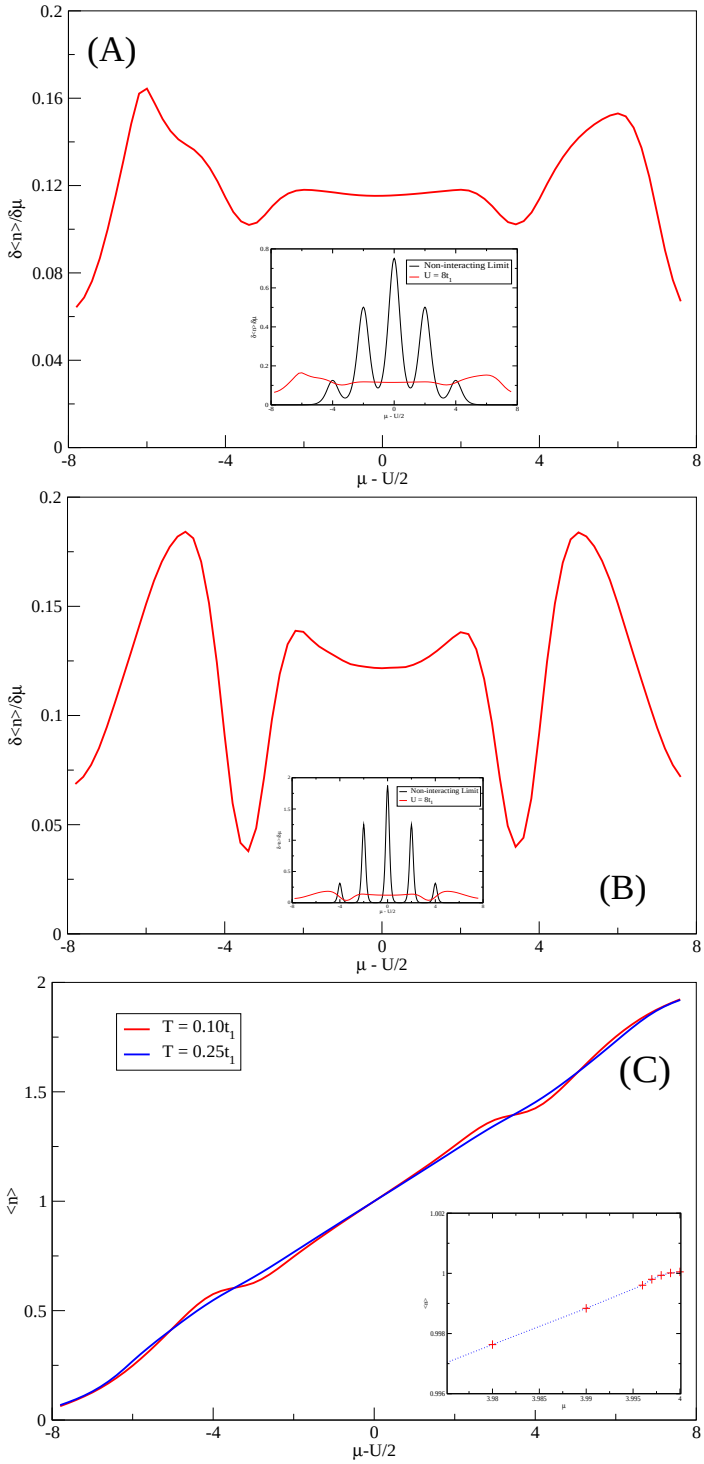

Figure 4.19: The charge susceptibility $\frac{\partial\langle\hat{n}\rangle}{\partial\mu}$ as a function of $\tilde{u} = \mu - U/2$ for the system on a 4×4 lattice, with with $U = 8t_1$ at (A) $T = 0.25t_1$ and (B) $T = 0.10t_1$. In the insets of (A) and (B), the results for non-interacting system are also shown. (C) plots the occupation number as the function of the chemical potential μ at $T = 0.10t_1$ and $0.25t_1$. The inset of (C) shows a detailed plot of $\langle n\rangle$ vs. μ near half-filling at $T = 0.10t_1$. The flat plain of $\langle n\rangle$ is obvious.

over some finite μ-interval denoted by $[\mu_-, \mu_+]$. The charge excitation gap is then given by

$$\Delta = \mu_+ - \mu_-. \tag{4.9}$$

Note that the quantity $\partial\langle n\rangle/\partial\mu$ is actually the charge susceptibility of the system and a measure of its compressibility [60]. Strictly speaking, the gap is defined, and Equation (4.9) holds, only for $N \to \infty$ and $T \to 0$. However, some approximation to this gap-like behavior should be observed even at finite N and T.

The occupancy number $\langle n\rangle$ was evaluated for a finite grid of μ in a certain range by Equation (2.18), (3.11) and (3.36). Using a second-order approximation ($n_{max} = 2$) for $G(\vec{k}, i\nu_m)$, the μ-derivative $\partial\langle n\rangle/\partial\mu$ was evaluated by carrying out a cubic spline interpolation between the μ-grid points. The results are shown in Figure 4.19 in terms of the particle-hole symmetric chemical potential $\tilde{\mu} = \mu - U/2$ (Equation (2.7)) for a range $\tilde{\mu} = -U$ to $\tilde{\mu} = +U$ for a finite grid of 25 $\tilde{\mu}$-points. The occupation number $\langle n\rangle$ increases as the chemical potential is raised, as required by thermodynamic stability, i.e, by $\partial\langle n\rangle/\partial\mu \geq 0$. On the other hand, at low temperature, the increase of $\langle n\rangle$ with μ does not have a uniform slope, but around the particle-hole symmetry point, $\tilde{\mu} = 0$, the slope $\partial\langle n\rangle/\partial\mu$ is depressed, as illustrated in Figure 4.19A and Figure 4.19B. This can also be seen in more detail over a smaller $\tilde{\mu}$-range near $\tilde{\mu} = 0$ in Figure 4.19C. This shows that if particle-hole symmetric chemical potential $\tilde{\mu}$ is within the expected range of the gap ,$[\tilde{\mu}_-, \tilde{\mu}_+]$, with $\tilde{\mu}_- \cong -U/2$ and $\tilde{\mu}_+ \cong +U/2$, $\partial\langle n\rangle/\partial\mu$ becomes very small, though not exactly zero. Such a strong suppression of $\partial\langle n\rangle/\partial\mu$ to very small but non-zero values, over the range from $\tilde{\mu}_-$ to $\tilde{\mu}_+$ is exactly what one expects to observe for a charge excitation gap at low, but finite, temperature. For comparison, we also show $\partial\langle n\rangle/\partial\mu$ for the non-interacting system in the insets of Figure 4.19(A) and Figure 4.19(B). Clearly, $\partial\langle n\rangle/\partial\mu$ for the interacting case is strongly suppressed compared to the non-interacting case for $\tilde{\mu}$ between $\tilde{\mu} \cong -U/2$ and $\tilde{\mu} \cong +U/2$.

By applying the particle-hole transformation, one can show that the plot of $\partial\langle n\rangle/\partial\mu$ versus $\tilde{\mu}$ should be exactly symmetric around $\tilde{\mu} = 0$. This symmetry is approximately obeyed

in Figure 4.19(A) and Figure 4.19(B). The deviations from symmetry are again due to the Monte Carlo statistical error.

Near 1/4 and 3/4 filling, i.e, $\langle n \rangle \cong 0.5$ and $\langle n \rangle \cong 1.5$, implicated by taking the derivative $\partial \langle n \rangle / \partial \mu$, there is a relatively abrupt change in filling with the chemical potential, as indicated by the maxima in $\partial \langle n \rangle / \partial \mu$ at $\tilde{\mu} \cong \pm 5t_1$, indicating that the filling may be close to becoming unstable towards phase separation. Note that the phase separation would require that the charge susceptibility (or compressibility) $\partial \langle n \rangle / \partial \mu$ becomes infinite. Such a phase separation in the two-dimensional Hubbard model near 1/4 (or 3/4) band-filling has been suggested to occur in another study [61].

For the high-T_c cuprates at finite doping, pseudogaps at low excitation energy have been found in experiments [53][54][62][63]. The exact quantum Monte Carlo results also show the existence of such a pseudogap in the two-dimensional Hubbard model upon being doped [4]. Figure 4.20 shows two simulations in p-doped and n-doped cases respectively. A pseudogap is defined as a partial (but not complete) suppression of the spectral weight function in a low energy range around $\omega = 0$. It is interesting to note that our density of states results from the doped system do have an obvious pseudogap around $\omega = 0$. Note also that the two spectral weight functions in Figure 4.20 should be exactly symmetric to each other by particle-hole transformation. The deviations from symmetry in Figure 4.20 are again due to the Monte Carlo statistical error of the $\Sigma(\vec{k}, i\nu_m)$ input data (usually the statistical relative Monte Carlo error is about 10^{-3}). Our result is qualitatively close to the exact quantum Monte Carlo results [4] on the doped model with the same square lattice size.

4.9 Spin Susceptiblity

We calculated the spin susceptibility $\chi(\vec{Q}, i\omega_m = 0)$ at $T = 0.30t_1$ as a function of wave vector $\vec{Q}$ by the second-order approximation, shown in Figure 4.21. The strong antiferromagnetic spin fluctuation is clearly visible there as $\chi^{(zz)}(\vec{Q}, i\omega_m = 0)$ is strongly peaked at $\vec{Q} = (\pi, \pi)$.

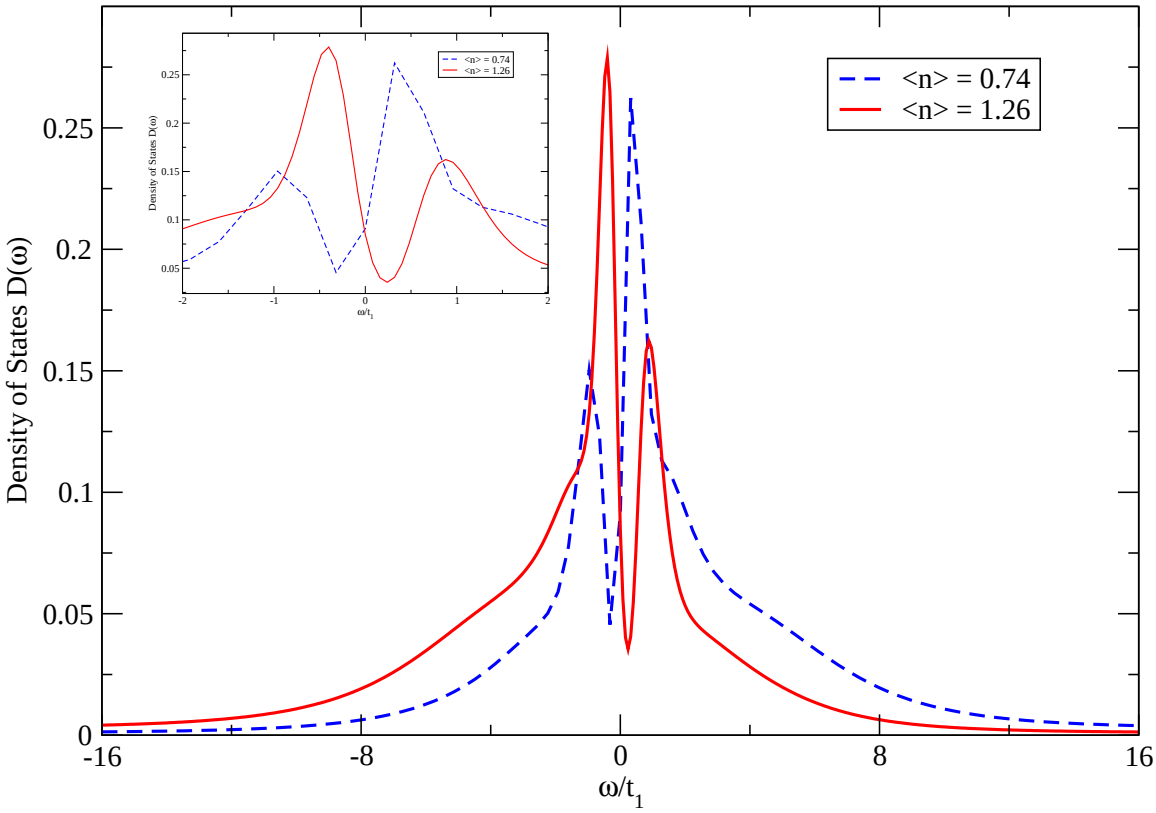

Figure 4.20: The density of states $D(\omega)$ for two-dimensional Hubbard model with doped band. Two simulations with different chemical potential are on a 4×4 lattice with $U = 8t_1$ at $T = 0.25t_1$, resulting at $\langle n \rangle = 0.74$ and $\langle n \rangle = 1.26$ respectively. The inset is a magnified view of the spectral weight function about $\omega = 0$.

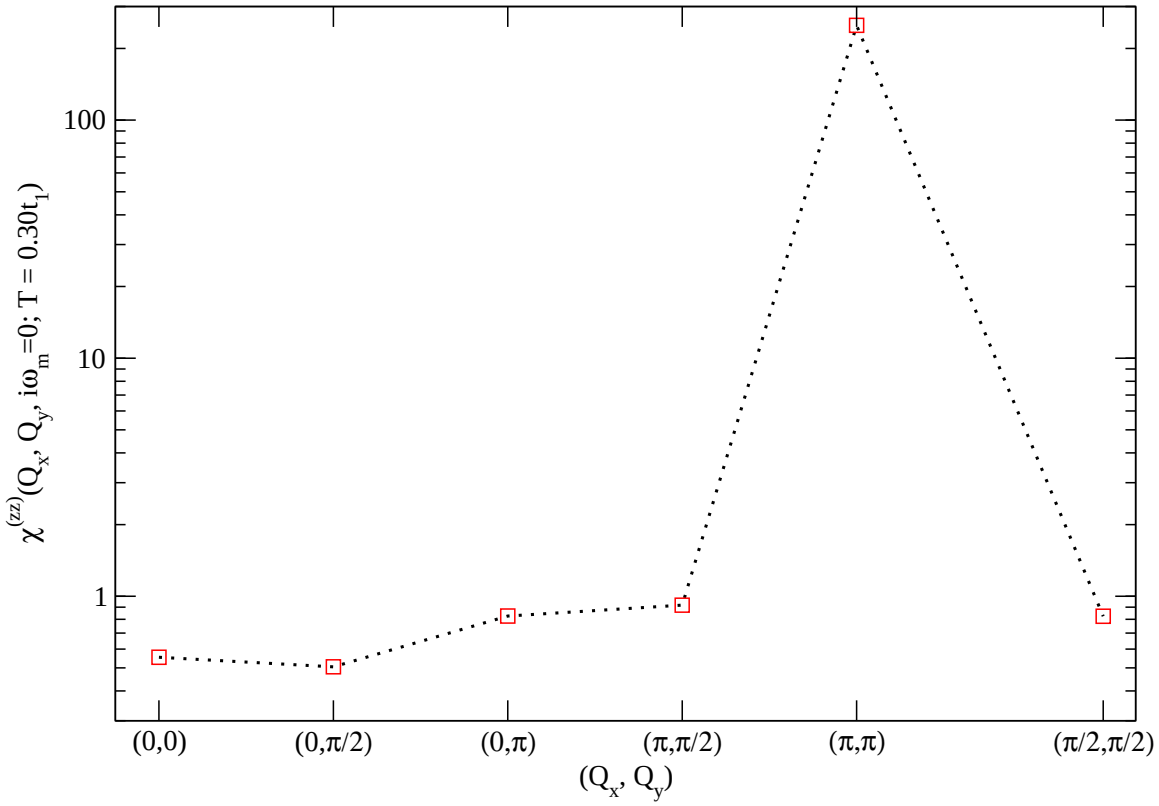

Figure 4.21: Spin susceptibility $\chi^{(zz)}(\vec{Q}, i\omega_m = 0)$ on a 4×4 lattice with $U = 8.0t_1$ and $\mu = U/2$ with the second order approximation. The strong spin fluctuation at antiferromagnetic ordering wave vector $\vec{Q} = (\pi, \pi)$, based on a same model.

This clearly shows that antiferromagnetism is indeed the dominant magnetic fluctuation in the system.

In order to study the antiferromagnetic long-range order of the two dimensional Hubbard model, we calculate the antiferromagnetic spin susceptibility $\chi^{(zz)}(\vec{Q}, i\omega_m = 0)$, i.e., for wave vector $\vec{Q} = (\pi, \pi)$.

Our finite-order self-consistent diagram approach inherits the mean-field theory behavior of the Hartree-Fock approximation, i.e., the first-order approximation $n_{max} = 1$, because our methods to calculate both self-energy and spin susceptibility are an extension of the Hartree-Fock approximation [37]. As a result, we will find a finite antiferromagnetic transition at finite temperature in the two-dimensional Hubbard model. This violates the Mermin-Wagner theorem, which requires a long range order, and, even worse, the theorem that finite systems cannot have a phase transition at finite temperature. Therefore, with a finite order truncation in our perturbation calculation, we don't expect to find the antiferromagnetic transition temperature to be $T = 0$, as required by the fundamental theories. However, we are interested in finding how the contribution from high-order perturbation terms is able to push the transition temperature closer to zero temperature.

For the Hubbard model, the spin susceptibility $\chi^{(zz)}(Q)$ in the first-order approximation (n_{max}) is given by

$$\chi^{(zz)}(Q) = \chi_0^{(zz)}(Q) + U \cdot (\chi_0^{(zz)}(Q))^2 + U^2 \cdot \frac{(\chi_0^{(zz)}(Q))^3}{1 - U \cdot \chi_0^{(zz)}(Q)} \tag{4.10}$$

where, the zeroth order contribution $\chi_0^{(zz)}$ is given by Equation (3.140) or

$$\chi_0^{(zz)}(Q) = (-\frac{T}{N}) \sum_k G(k)G(k+Q). \tag{4.11}$$

and $G(k)$ is the Green's function calculated from the self-energy in first-order approximation $n_{max} = 1$.

With the first order approximation, at particle-hole symmetry, the zeroth order contribution $\chi_0^{(zz)}(Q)$ is independent of on-site interaction U, because the self-energy $\Sigma^{(1)}(\vec{k}, \nu_m)$

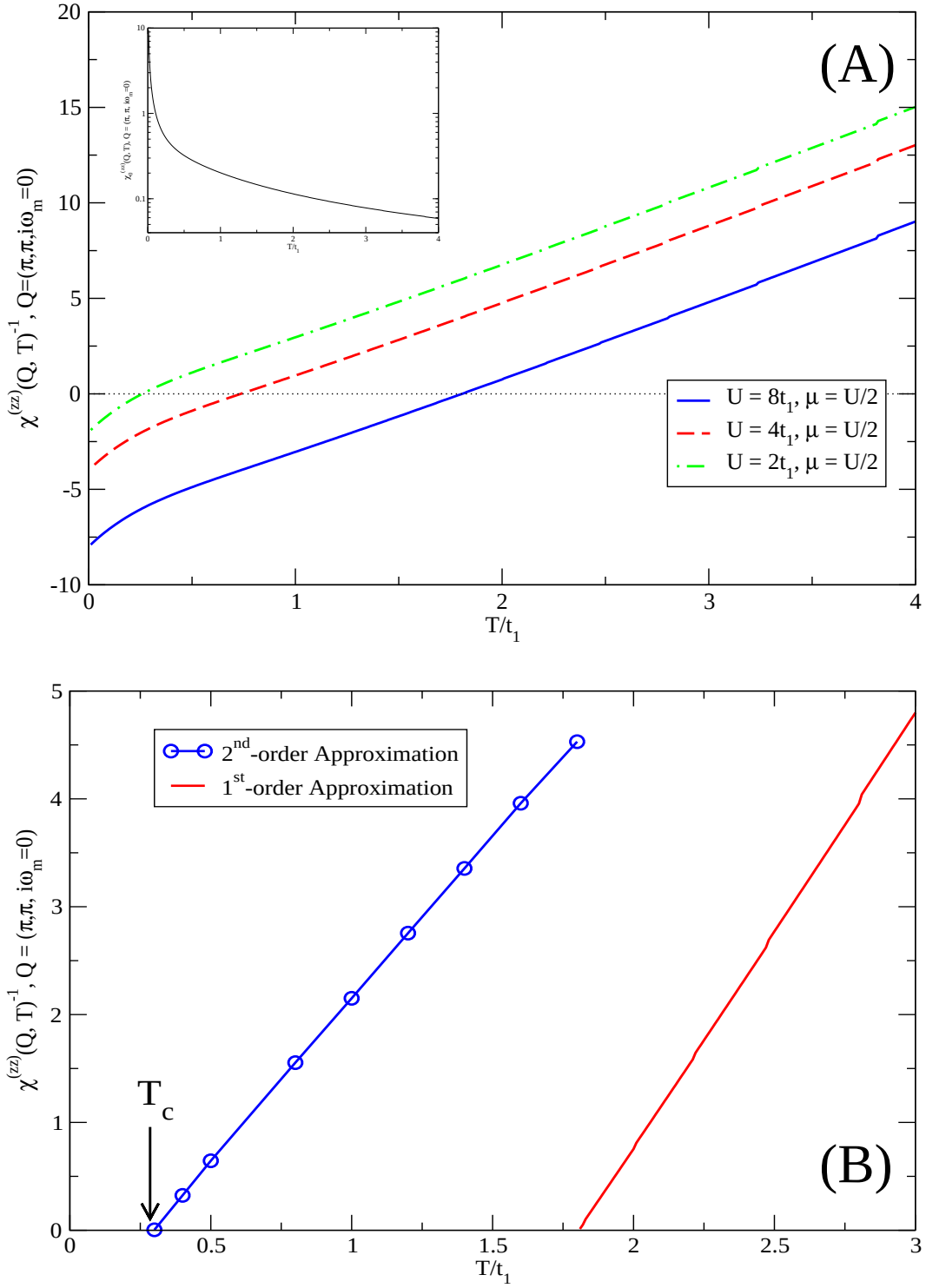

Figure 4.22: The spin susceptibility $\chi^{(zz)}(\vec{Q}, i\omega_m = 0)$, with antiferromagnetic wave vector $\vec{Q} = (\pi, \pi)$, on a 4×4 square lattice at half-filling at various temperatures. (A) gives out the spin susceptibility $\chi^{(zz)}(Q)$ in the first-order approximation with a variety of on-site interaction (including $U = 8t_1$, $4t_1$ and $2t_1$) with $\mu = U/2$ calculated by Equation (4.10) The inset of (A) shows the zeroth order contribution to the spin susceptibility $\chi_0^{(zz)}(Q)$ with $U = 8t_1$ and $\mu = U/2$ in the first-order approximation. (B) compares the spin susceptibilities calculated by the first- and second-order on a 4×4 square lattice with $U = 8t_1$ and $\mu = U/2$.

will cancel μ in Equation (3.12). The inset of Figure 4.22A shows that $\chi_0^{(zz)}(Q)$ is finite at finite temperature, and approaches to infinity as temperature is reduced.

In the first-order approximation ($n_{max} = 1$), according to Equation (4.10), the spin susceptibility will therefore diverge at critical temperature T_c determined by

$$U = 1/\chi_0^{(zz)}(Q). \tag{4.12}$$

The antiferromagnetic phase transition always occurs at a finite temperature T_c even for a finite lattice, since $\chi_0^{(zz)}(Q)$ diverges to ∞ for $T \to 0$, and approaches to zero for $T \to \infty$. At strong-coupling, for example, $U = 8t_1$ shown in Figure 4.22A, the transition temperature $T_c \approx 1.80t_1$.

At weak-coupling and high temperature, the higher order perturbation terms only make trivial contributions to the spin susceptibility. For example, at $T = 1.0t_1$, for a 4×4 Hubbard lattice with half-filled band and on-site repulsion $U = 2t_1$, the spin susceptiblity calculated by the first- and second-order approximation are almost the same within numerical precision,

However, the higher order diagrams do change the behavior of the spin susceptibility at low temperature and intermediate/strong interaction U substantially. At intermediate coupling, the higher order correction is essential. If the on-site interaction $U = 8.0t_1$, the effect of the second-order contribution is significant, which is obviously seen in Figure 4.22B. The critical temperature T_c is pushed to much lower temperature, say $T_c \approx 0.29t_1$ for $n_{max} = 2$, compared with $T_c \approx 1.80t_1$ calculated by Hartree-Fock approximation, $n_{max} = 1$.

Although it still violates the Mermin-Wagner theorem (and the finite-system T_c theorem) due to its mean-field-theory behavior, the second order approximation gives an important improvement for the intermediate and strong coupling regimes.

Below the critical temperature T_c, the spin susceptibility turns negative in any order of approximation up to the second order. This is of course unphysical and violates fundamental thermodynamic stability requirements. To restore thermodynamic stability, one would have to perform calculations in the symmetry-broken antiferromagnetic ordered phase, which is

beyond the scope of this thesis. It is also of limited physical interest, since we know that this symmetry-broken phase is an artifact of our approximation.

At particle-hole symmetry, the sum of the contributions of all third order two-particle vertex diagrams ($n_{max} = 3$) is zero by mutual cancellation, similar to the third order self-energy diagrams. Therefore, all second-order results shown here are actually also correct up to order $n_{max} = 3$.

Chapter 5

Conclusion and Future Work

In summary, we have developed an efficient methodology to calculate the imaginary-frequency one-particle Green's function $G(\vec{k}, i\nu_m)$ and self-energy $\Sigma(\vec{k}, i\mu)$ for the interacting Fermion models, such as the pure and extended Hubbard models by the self-consistent higher order self-energy diagrammatic approximation combined with the Monte Carlo summation technique. Based on the Green' function obtained by this approximation method, we have also developed the methodology to calculate the sum of the the two-particle irreducible vertex functions $\Gamma_{irr}(k, k', Q)$ by Monte Carlo summation of the irreducible vertex diagrams.

We have demonstrated the feasibility of these methodologies by applying them to the two dimensional Hubbard model. Specifically, we have used these new computational methods to search for the Mott-Hubbard gap and the antiferromagnetism in the Hubbard model. Because this work is intended mainly as a feasibility study of our proposed new methodology, our calculations have focused on small finite lattices and a particularly simple limit, the particle-hole symmetry limit, of the Hubbard model.

Based on the single-particle Green's function $G(k)$, we show the existence, or at least the incipient development, of the Mott-Hubbard gap in the two-dimension Hubbard model from three different aspects: (1) the development of the incoherent side bands of the spectral weight function $A(\vec{k}_F, \omega)$ with the on-Fermi-surface $\vec{k}$-vector, $\vec{k}_F$ in the particle-hole symmetric model, (2) the suppression of the single-particle density of states and (3) the strong suppression of the compressibility $\partial\langle n\rangle/\partial\mu$ as a function of particle-hole symmetric chemical potential $\tilde{\mu}$ around $\tilde{\mu} = 0$.

Also, we have demonstrated the strong antiferromagnetism of the two-dimensional Hubbard model at half-filling via its spin susceptibility $\chi^{(zz)}(Q)$, which is obtained from the two-particle vertex diagram $\Gamma_{irr}(k, k', Q)$.

Our results have shown that including higher-order corrections is important to the study of the two-dimensional Hubbard model. The inclusion of higher-order self-energy diagrams in the calculation of the Green's function $G(k)$ causes the suppression of the quasiparticle peak of $A(\vec{k}_F, \omega)$ and helps to develop the corresponding incoherent side bands of $A(\vec{k}_F, \omega)$ at higher energies, as required for gap formation. Also, including second-order vertex diagrams to the spin susceptibility $\chi^{(zz)}(Q)$ pushes the antiferromagnetic transition temperature of the two-dimensional Hubbard model to a much lower temperature compared to the first-order approximation. This is qualitatively consistent with the requirement of statistical mechanics principles preventing a finite antiferromagnetic transition temperature $T_c > 0$ in the two-dimensional Hubbard model on both finite and infinite lattices.

We also notice that our self-consistent diagrammatic approximation results for the two-dimensional Hubbard model are consistent with the Fermi-liquid theory, even though the size of square lattice that we simulate on is finite. We expect the inclusion of high-order ($n_{max} \geq 6$) in the calculation can obtain a better approximation to the Mott-Hubbard gap behavior.

The main limitation of our self-consistent diagrammatic methodology is imposed by the available computational power. It may require more than 5000 hours CPU time in order to calculate the self-energy at a low temperature, for instance $T \leq 0.1t_1$, with the fourth-order approximation. Namely, as long as we have sufficient computational power, we can perform the simulation on any size of lattice (L) to any finite order of diagrammatic approximation (n_{max}) at any temperature (T). The limitation on the diagrammatic approximation order n_{max} is due to super-exponential growth of the number of diagrams. The computing effort grows only linearly with the product of the lattice size and the inverse of the temperature ($\propto N/T$). Therefore, we could extend the calculation to larger lattices with larger parallel

processing systems. Parallelization is perfectly applicable to our method, because the Monte Carlo algorithm is based on a trivial perfect sampling method and one can therefore achieve linear speedup in a trivial parallelization without sacrificing statistical independence of the Monte Carlo sample.

Based on our methodology, it is of interest to extend our current study on the Hubbard model to a wider range of model parameters and system sizes with more available CPU time.

The size effect is very important to study the ordering behavior of the physical models with finite size. We are planning to calculate the one-particle Green's function $G(\vec{k}, i\nu_m)$ or two-particle irreducible vertex function $\Gamma_{irr}(k, k'; Q)$ on a larger lattice size, such as 16×16 or 32×32, and compare the single-particle weight function $A(\vec{k}, \omega)$ or the spin susceptibility $\chi^{(zz)}(Q)$ with $A(\vec{k}, \omega)$ or $\chi^{(zz)}(Q)$ on the 4×4 lattice, respectively.

We should also push the diagrammatic approximation to even higher order, say $n_{max} = 6$ or 8, and see how the higher order diagrammatic corrections affect the single-particle spectral weight function $A(\vec{k}, \omega)$ for the formation of the Mott-Hubbard gap.

One of the center of interests of the high-T_c cuprates is that they can be in a superconducting state if they are doped. Recent studies [64][65][66][67] based on quantum Monte Carlo finite-cluster embedding methods [8] have strongly suggested that the two dimensional Hubbard model does indeed exhibit a superconducting phase at finite doping. Within our diagrammatic approximation scheme, it is straightforward to search for superconducting instabilities by calculating the relevant superconducting pair susceptibilities starting from a Baym-Kadanoff construction of the irreducible particle-particle vertex function. Such a calculation is entirely analogous to our calculation of the magnetic susceptibility starting from the irreducible particle-hole vertex functions and is of the same computational complexity.

Since the Hubbard model is characterized by short-range dynamical fluctuations, the Monte Carlo self-consistent high-order diagrammatical approximation method can be combined into the Dynamical Cluster Approximation [8][68] by replacing the quantum Monte

Carlo method, which might offer us a more powerful tool to explore the Hubbard model on much larger lattice sizes or at least, to extrapolate to infinite system size more efficiently.

Bibliography

[1] J. Hubbard, Proc. R. Soc. (London) Ser. A **276**, 238 (1963)

[2] P. W. Anderson, Science **235**, 1196 (1987)

[3] S. R. White, Phys. Rev. B **46**, 5678 (1992)

[4] S. R. White, Phys. Rev. B **44**, 4670 (1991)

[5] E. Dagotto, A. Moreo, F. Ortolani, J. Riera, and D. J. Scalapino, Phys. Rev. Lett. **67**, 1918 (1991)

[6] A. Georges and G. Kotliar, Phys. Rev. B **45**, 6479 (1992)

[7] M. Jarrell, Phys. Rev. Lett. **69**, 168 (1992)

[8] T. Maier, M. S. Jarrell, T. Pruschke, M. H. Hettler, Rev. Mod. Phys. **77**, 1027 (2005)

[9] E. Dagotto Rev. Mod. Phys. **66**, 763 (1994)

[10] G. Baym, Phys. Rev. **127**, 1391 (1962)

[11] M. C. Gutzwiller, Phys. Rev. Letters **10**, 159 (1963) ; Phys. Rev. **134**, A923 (1964)

[12] Junjiro Kanamori, Prog. Theor. Phys., Kyoto **30** 275 (1963)

[13] E. C. Stoner, Phil. Mag. **21**, 145 (1936); Proc. Roy. Soc. (London) **A165**, 372 (1938); **169**, 339 (1939); J. Phys. et radium **12**, 372 (1951);

[14] Y. Nagaoka, Phys. Rev. 147, 392 (1966)

[15] PW Anderson, Phys. Rev. **79**, 350 (1950)

[16] J. C. Slater, Phys. Rev. **36**, 57 (1930)

[17] J. C. Slater, Phys. Rev. **49**, 537, 931 (1936)

[18] W. F. Brinkmann, T. M. Rice, Phys. Rev. B **2**, 4302 (1970)

[19] A.P. Mackenzie and Y. Maeno, Rev. Mod. Phys. **75**, 657 (2003)

[20] J.G. Bednorz and K.A. Muller, Z.Phys. B **64** 189 (1986)

[21] F. Zhang and T. Rice, Phys. Rev. B **37**, R3759 (1988)

[22] N. Ashcroft, N. Mermin *Solid State Physics* (Holt, Rinehart and Winston, New York, 1976)

[23] H.-B. Schüttler, A. J. Fedro, Phys. Rev. B **45**, 7588 (1992)

[24] M. S. Hybertsen, E. B. Stechel, M. Schlüter, D. R. Jennison, Phys. Rev. **B 41**, 11068 (1990)

[25] W. Kohn and J. M. Luttinger, Phys. Rev. **118**, 41 (1960)

[26] J. M. Luttinger and J. C. Ward, Phys. Rev. **118**, 1417 (1960)

[27] J. M. Luttinger, Phys. Rev. **119**, 1153 (1960)

[28] M. Luttinger, Phys. Rev. **121**, 942 (1960)

[29] W. Kohn, Phys. Rev. **133**, A171 (1964)

[30] E. Manousakis, Rev. Mod. Phys. **63**, 1 (1991)

[31] N. D. Mermin, H. Wagner, Phys. Rev. Lett. **17**, 1133 (1966)

[32] N. D. Mermin, Phys. Rev. **176**, 250 (1968)

[33] V. L. Berezinskii, Sov. Phys. JETP **32**, 493 (1971)

[34] Chakravarty, S., B. I. Halperin, and D. Nelson, Phys. Rev. Lett. **60**, 1057 (1988)

[35] Chakravarty, S., B. I. Halperin, and D. Nelson, Phys. Rev. B **39**, 2344 (1989)

[36] Peter Fulde, *Electron correlations in molecules and solids* (Springer,1995)

[37] A.L. Fetter, J.D. Walecka, *Quantum Theory of Many-Particle Systems* (McGraw-Hill, New York, 1971)

[38] G. D. Mahan, *Many-Particle Physics*, 2nd edn. (Plenum Press, New York, 1981)

[39] A. Kampf and J. R. Schrieffer, Phys. Rev. B **41**, 6399 (1990)

[40] A. P. Kampf and J. R. Schrieffer, Phys. Rev. B **42**, 7967 (1990)

[41] G. Baym, L. Kadanoff, Phys. Rev. **124**, 287 (1961)

[42] J. C. Ward, Phys. Rev. **78**, (1950) 182

[43] Kirchhoff, Ann. Phys. Chem, **72** 497-508 (1847)

[44] R. W. Robinson (unpublished)

[45] R.W. Robinson private communication and Depth-first-search algorithm

[46] V. Zlatić, B. Horvatić, B. Dolicki, S. Grabowski, P. Entel; K. -D. Schotte Phys. Rev. B **63**, 035104 (2001)

[47] K. Yosida, K. Yamada, Prog. Theor. Phys. Supple. **46**, 244 (1970); K. Yamada, Prog. Theor. Phys. **53**, 970 (1975)

[48] P. W. Anderson, Phys. Rev **124**, 41 (1961)

[49] J.K. Freericks, M. Jarrell, Phys. Rev. B **50**, 6939 (1994)

[50] F. Gebhard, E. Jeckelmann, S. Mahlert, S. Nishimoto, R.M. Noack, Eur. Phys. J. B **36**, 491-500 (2003)

[51] J.N. Corcoran, U. Schneider, H. -B. Schüttler, *Perfect Stochastic Summation In High Order Feynman Graph Expansions* (2003)

[52] D. P. Landau and K. Binder, *A Guide to Monte Carlo Simulations in Statistical Physics* (Cambridge University Press, New York, 2000)

[53] Andrea Damascelli, Zahid Hussain, Zhi-Xun Shen, Rev. Mod. Phys. **75**, 473 (2003)

[54] J. Hoffmann et al., Science **297**, 1148 (2002)

[55] J. E. Gubernatis, M. Jarrell, R. N. Silver, D. S. Silvia, Phys. Rev. B **44**, 6011 (1991)

[56] M. Jarrell, private communication

[57] J.Blaizot and G.Ripka, *Quantum Theory of Finite Systems*,(The MIT Press, Cambridge, 1986)

[58] Makoto Matsumoto and Takuji Nishimura, ACM Transactions on Modeling and Computer Simulation, Vol. 8, No. 1, pp 3–30 (1998)

[59] A.Georges and G. Kotliar, Phys. Rev. B **45**, 6479 (1992)

[60] D. Pines and P. Nozierés, *The Theory of Quantum Liquids* (Addison-Wesley, Reading, MA, 1990), Vol. 2

[61] A. Macridin, M. Jarrell, Th. Maier, cond-matt/0506148 (2005)

[62] T. Timusk and B. Statt, Rep. Prog. Phys. **62**, 61 (1999)

[63] M. A. Kastner, R. J. Birgeneau, G. Shirane, Y. Endoh, Rev. Mod. Phys. **70**, 897 (1998)

[64] T. A. Maier, M. S. Jarrell, and D. J. Scalapino, Phys. Rev. Lett. **96**, 047005 (2006)

[65] T. A. Maier, M. Jarrell, T. C. Schulthess, P. R. C. Kent, and J. B. White, Phys. Rev. Lett. **95**, 237001 (2005)

[66] David Sénéchal, P.-L. Lavertu, M.-A. Marois, and A.-M. S. Tremblay, Phys. Rev. Lett. **94**, 156404 (2005)

[67] S. S. Kancharla, M. Civelli, M. Capone, B. Kyung, D. Sénéchal, G. Kotliar, and A.-M. S. Tremblay, cond-mat/0508205

[68] M. H. Hettler, M. Mukherjee, M. Jarrell, and H.R. Krishnamurthy, Phys. Rev. B **61**, 12739 (2000)

[69] K. S. D. Beach, cond-mat/0403055 (2004)

Appendix A

Particle-hole Symmetry in Hubbard Model

A.1 Particle-hole Transformation and Particle-hole Symmetry

In general, the particle-hole transformation is defined on the electron annihilation and creation operators as

$$\bar{c}_{j\sigma} := e^{i\phi_j} c^+_{j\sigma} \tag{A.1}$$

$$\bar{c}^+_{j\sigma} := e^{-i\phi_j} c_{j\sigma}, \tag{A.2}$$

such that new $\bar{c}_{l\sigma}$ and $\bar{c}^+_{l\sigma}$ obey the standard fermion anti-commuting rules, and ϕ_j is some arbitrary phase factor. This transformation can also be expressed in terms of a unitary operator U_{ph} such that [57]

$$\bar{c}_{j\sigma} = U_{ph} c_{j\sigma} U^+_{ph} \tag{A.3}$$

$$\bar{c}^+_{j\sigma} = U_{ph} c^+_{j\sigma} U^+_{ph}. \tag{A.4}$$

The transformed number operator $\hat{\bar{N}}_l$ is thus defined as

$$\hat{\bar{N}}_e := \sum_j \hat{\bar{n}}_j := \sum_{j\sigma} \bar{c}^+_{j\sigma} \bar{c}_{j\sigma} \tag{A.5}$$

and it obeys

$$\hat{\bar{N}}_e = 2N - \hat{N}_e \tag{A.6}$$

for a finite lattice with N sites, j ,and, therefore $2N$ single-particle states, (j, σ), i.e, $\hat{\bar{N}}_e$ counts the number of holes in the system whereas $\hat{N}_e$ counts the number of electrons.

If the particle-hole transformation, as Equation (A.3) and (A.4), is applied to the extended Hubbard model, whose hamiltonian $\hat{H}$ is defined in Equation (2.4), then we have

$$\begin{aligned}\hat{\tilde{H}} &= U_{ph}\hat{H}U_{ph}^{+} \\ &= \sum_{\substack{lj,\sigma \\ l\neq j}}[-t_{lj}\bar{c}_{l\sigma}^{+}\bar{c}_{j\sigma} + \frac{1}{2}V_{lj}(\hat{\bar{n}}_l - 1)(\hat{\bar{n}}_j - 1)] - \tilde{\mu}\hat{\tilde{N}}_e. \end{aligned} \tag{A.7}$$

Then, "particle-hole" symmetry is obeyed in the extended Hubbard model if

$$\hat{\tilde{H}} = \hat{H}, \tag{A.8}$$

or equivalently,

$$U_{ph}\hat{H}U_{ph}^{+} = \hat{H} \quad \text{or} \tag{A.9}$$

$$[U_{ph}, \hat{H}]_{-} = 0 \tag{A.10}$$

for some choice of the phase ϕ_j.

A square lattice can be partitioned into two intervening sub-lattices, say A and B. The necessary and sufficient condition for the extended Hubbard model on a square lattice to obey the particle-hole symmetry is the limitation on the hybridization terms t_{ij}, such that

$$t_{ij} = \begin{cases} 0 & \text{for } l \text{ and } j \text{ on the same sub-lattice } (l, j \in A \text{ or } l, j \in B) \\ \text{arbitrary} & \text{for } l \text{ and } j \text{ on opposite sublattices } (l \in A,\, j \in B \text{ or } l \in B,\, j \in A) \end{cases} \tag{A.11}$$

Then we can choose

$$\phi_j = \begin{cases} 0 & j \in A \\ \pi & j \in B \end{cases} \tag{A.12}$$

so that Equation (A.1) and (A.2) now can be written as

$$\bar{c}_{j\sigma} = (-1)^{\phi_j}c_{j\sigma}^{+} = \begin{cases} +c_{j\sigma}^{+}, & j \in A \\ -c_{j\sigma}^{+}, & j \in B \end{cases} \tag{A.13}$$

$$\bar{c}_{j\sigma}^{+} = (-1)^{\phi_j}c_{j\sigma} = \begin{cases} +c_{j\sigma}, & j \in A \\ -c_{j\sigma}, & j \in B \end{cases} \tag{A.14}$$

A.2 Green's function of Particle-hole Symmetric Model

If the two-dimensional Hubbard model obeys the particle-hole symmetry, according to Equation (A.13) and (A.14), the Green's function in the coordinate space and imaginary-time domain

$$G(j,l;\tau) \;=\; -\langle T_\tau[c_j(\tau)c_l^+(0)]\rangle$$

is particle-hole transformed to

$$\bar{G}(j,l;\tau) \;=\; -\langle T_\tau[\bar{c}_j(\tau)\bar{c}_l^+(0)]\rangle. \tag{A.15}$$

If the model obeys particle-hole symmetry, then

$$G(j,l;\tau) = \bar{G}(j,l;\tau). \tag{A.16}$$

Expressed by the originally defined creation/annihilation operator, by assuming $0 < \tau < \beta$, and using the cyclic relation [38],

$$G(j,l;\tau) = -G(j,l;\tau+\beta) \quad \text{as } -\beta < \tau < 0, \tag{A.17}$$

we have

$$G(j,l;\tau) = \bar{G}(j,l;\tau) = (-1)^{\phi(j-l)}G(l,j;\beta-\tau). \tag{A.18}$$

if the particle-hole symmetry is obeyed.

Combining Equation A.18 with the Fourier transform of the Green's function from the coordinate space to the momentum space

$$G(\vec{k},\tau) \;=\; \frac{1}{N}\sum_{j,l} e^{i\vec{k}\cdot(\vec{r}_j-\vec{r}_l)}(-1)^{\phi(j-l)}G(l,j;\beta-\tau) \tag{A.19}$$

The fact $(-1)^{\phi(j-l)}$ serves like an additional factor $e^{i\vec{K}\cdot(\vec{r}_j-\vec{r}_i)}$, where $\vec{K} = (\pi,\pi)$.

$$(-1)^{\phi(j-l)} = e^{i\vec{K}\cdot(\vec{r}_j-\vec{r}_i)} = \begin{cases} 1 & \text{if } \vec{r}_j - \vec{r}_l \in \text{sublattice A} \\ -1 & \text{if } \vec{r}_j - \vec{r}_l \in \text{sublattice A} \end{cases}$$

Thus,

$$G(\vec{k},\tau) = G(\vec{k}+\vec{K},\beta-\tau), \tag{A.20}$$

if the system is in particle-hole symmetry.

Then we perform the Fourier transformation on imaginary time τ to Matsubara frequency $i\nu_m$. From Equation (A.20) and (3.4), we have the following relation

$$\begin{aligned} \mathrm{Re}G(\vec{k},i\nu_m) &= -\mathrm{Re}G(\vec{k}+\vec{K},i\nu_m) && \text{(A.21)} \\ \mathrm{Im}G(\vec{k},i\nu_m) &= \mathrm{Im}G(\vec{k}+\vec{K},i\nu_m) && \text{(A.22)} \end{aligned}$$

Furthermore, if the t_{ij} are consistent with particle-hole symmetry, i.e, obey Equation (A.11), then

$$\epsilon_{\vec{k}+\vec{K}} = -\epsilon_{\vec{k}}$$

and it is easy to show that

$$\begin{aligned} \mathrm{Re}\Sigma_{>}(\vec{k}+\vec{K},i\nu_m) &= -\mathrm{Re}\Sigma_{>}(\vec{k},i\nu_m) && \text{(A.23)} \\ \mathrm{Im}\Sigma_{>}(\vec{k}+\vec{K},i\nu_m) &= \mathrm{Im}\Sigma_{>}(\vec{k},i\nu_m) && \text{(A.24)} \end{aligned}$$

for $\vec{K} = (\pi,\pi)$.

A.3 Odd-order Self-enegy Diagrams

In the pure Hubbard model with the on-site repulsive interaction U. The Green's function $G(l,j;\tau)$ is given by

$$G(l,j;\tau) = -\langle T_\tau[c_{l\sigma}(\tau)c^+_{j\sigma}(0)]\rangle \tag{A.25}$$

As we do the particle-hole transformation to the Hubbard model, equivalently, we get a model that can be described by

$$\bar{G}(l,j;\tau) = -\langle T_\tau[\bar{c}_{l\uparrow}(\tau)\bar{c}^+_{j\uparrow}(0)]\rangle \tag{A.26}$$

with the on-site attractive interaction

$$\bar{U} = -U, \tag{A.27}$$

For $n \geq 2$, insert Equation (A.25) into Equation (3.46) for nth-order diagrams' contribution $\Sigma^{(n)}(k)$, and insert Equation (A.26) into Equation (3.46) for $\bar{\Sigma}^{(n)}(k)$, then it is easy to show that if the Hubbard model obeys the particle-hole symmetry, then

$$G(\vec{k}, i\nu_m) = \bar{G}(\vec{k}, i\nu_m), \tag{A.28}$$

and as a consequence, for odd order $n \equiv 2l+1$ or even order $n \equiv 2l$:

$$\Sigma^{(2l+1)}(k) = -\bar{\Sigma}^{(2l+1)}(k) = 0 \tag{A.29}$$

$$\Sigma^{(2l)}(k) = \bar{\Sigma}^{(2l)}(k), \tag{A.30}$$

where l is an integer and $l \geq 1$.

Therefore, the odd-order (except the first-order) diagrams have zero contribution to the self-energy $\Sigma(k)$, if the Hubbard model obeys particle-hole symmetry.

Appendix B

Analytical Continuation and Maximum Entropy Method

We use the maximum entropy method to perform the analytical continuation on imaginary-frequency Green's function $G(\vec{k}, i\nu_m)$ to spectral weight function $A(\vec{k}, \omega)$.

B.1 Maximum Entropy Method

In general, the maximum entropy method (MEM) is used to solve the problems of

$$Y_l = \sum_i K_{l,j} A_j \tag{B.1}$$

for A_j with ill-conditioned matrix $K_{i,j}$ and noisy data Y_l. MEM is originally introduced to extract the spectral weight function from quantum Monte Carlo single-particle Green's function in imaginary time space, while the approaches can be generalized to that in imaginary (Matsubara) frequency space with trivial modification [55] [69]. In the following content, ξ is used to denote either τ for imaginary time or $i\nu_m$ for imaginary frequency.

The idea of maximum entropy method is to find the spectral weight $A(\omega)$ that maximizes the conditional probability distribution function (PDF) $P[A|\bar{G}, I]$, where $\bar{G}$ is the input simulation data and I is to denote the relevant background information as the prior knowledge from $A(\omega)$ and also referred to as the "default model". The PDF $P[A|\bar{G}, I]$ is proportional to the product of $P[A|I]$, a prior probability distribution function, and the likelihood function $P[\bar{G}|A, I]$ by Bayes's theorem. The reliability of estimation is indicated by the width of the PDF $P[A|\bar{G}, I]$.

In calculation, the spectral weight function $A(\omega)$ is combined into entropy $S[A]$ as

$$S[A] = -\int d\omega A(\omega) \ln(A(\omega)/D(\omega)). \tag{B.2}$$

where $D(\omega)$ is the default model containing "prior" information. The likelihood function is related to the goodness of fit χ^2, which is give by

$$\chi^2[A] \;=\; \int_a^b \frac{d\xi}{\sigma(\xi)^2} \left| \int d\omega K(\xi,\omega)A(\omega) - \bar{G}(\xi)\right|^2 \tag{B.3}$$

where $\bar{G}(\xi)$ is the input data (Green's function) with noise. The integral limit a and b are 0 and β, or ν_{min} and ν_{max}, for imaginary time or imaginary frequency respectively.

In practice, maximum entropy method tries to minimize the quantity $Q[A] = \chi^2 - \alpha^{-1}S$, using, for example, the gradient search techniques, such as the Newton-Raphson algorithm.

B.2 Implementation of Maximum Entropy Method (MEM)

The maximum entropy method is designed to analytically continue the non-perfect experimental data Y_l in the imaginary frequency domain to the corresponding spectral function A_i in real frequency domain in discrete representation. We need to map our problem, Equation (3.69), to Equation (B.1) as the following:

1. The imaginary-frequency Green's function $G(\vec{k}, i\nu_m)$ is mapped to Y_l as

$$Y_l = \begin{cases} \mathrm{Re}G(\vec{k}, i\nu_m) & \text{for } l = 1, \cdots, N_\nu \\ \mathrm{Im}G(\vec{k}, i\nu_m) & \text{for } l = N_\nu + 1, \cdots, 2N_\nu \end{cases} \tag{B.4}$$

   where N_ν is the number of cut-off Matsubara frequencies.

2. The kernel function $K(l, j)$ is defined as

$$K(l,j) = \begin{cases} \mathrm{Re}(\frac{\delta\omega}{i\nu_l - \omega_j}) & 1 \le l \le N_\nu \\ \mathrm{Im}(\frac{\delta\omega}{i\nu_{l-N_\nu} - \omega_j}) & N_\nu < l \le 2N_\nu \end{cases} \tag{B.5}$$

   where ω_j is defined on a discrete real frequency grid in a finite interval $[\omega_{min}, \omega_{max}]$ of size N_ω, such that

$$\omega_j = \omega_{min} + (j-1) \times \delta\omega \quad \text{for } j = 1, \cdots, N_\omega \tag{B.6}$$

   and

$$\delta\omega = \frac{\omega_{max} - \omega_{min}}{N_\omega - 1}. \tag{B.7}$$

3. The spectral weight function $A(\vec{k},\omega)$ to solve by MEM is mapped to A_j, such that

$$A(\vec{k},\omega) \rightarrow A(\vec{k},\omega_j) \tag{B.8}$$

4. Then Equation (3.69) is thus mapped to Equation (B.1) as

$$\mathrm{Re}G(\vec{k},\mathrm{i}\nu_m) = \sum_j K(m,j)A(\vec{k},\omega_j) \tag{B.9}$$

$$\mathrm{Im}G(\vec{k},\mathrm{i}\nu_m) = \sum_j K(m+N_\nu,j)A(\vec{k},\omega_j). \tag{B.10}$$

The MEM solution for $A(\vec{k},\omega)$ also require the default model as the the "prior knowledge". We construct the default model of the information of high-frequency behavior of the Green's function (Equation (3.32)) [56]. First we solve M_p from the high imaginary-frequency Green's function

$$G(i\nu_m) = \sum_{p=0}^{p_{max}} (\frac{1}{i\nu_m})^{p+1} M_p \tag{B.11}$$

by least square fit method, and p_{max} is chosen by experience. Then, we can generate a default model m_j (for each ω_j, $j = 1,\cdots,N_\omega$) by maximizing the following function

$$\sum_j m_j \ln(m_j) - \sum_{p=0}^{p_{max}} \lambda_p (\sum_j m_j \omega_j^p - M_p) \tag{B.12}$$

to the constants λ_p. Hence, with the solutions, λ_p for $p = 0,\cdots,p_{max}$, the default model is generated as

$$m_j = \exp(\sum_{p=0}^{p_{max}} \lambda_p \omega_j^p - 1) \tag{B.13}$$

Appendix C

Monte Carlo Statistical Error and Self-consistent Iteration Convergence Criterion

C.1 Monte Carlo Error

In the computation with Monte Carlo summation technique, we need to estimate the Monte Carlo error of the data simulated. Suppose that we perform R repetitions of the Monte Carlo calculation. In each repetition, there are M sampled data points $(\vec{k}_1, \cdots, \vec{k}_n)$. Therefore, the absolute MC error σ_A and relative MC error r_A are

$$\sigma \equiv \sqrt{\frac{1}{R}(\langle|\langle A\rangle|^2\rangle - \langle|\langle A\rangle|\rangle^2)} \tag{C.1}$$

$$r \equiv \frac{\sigma_A}{|\langle\langle A\rangle\rangle|} \tag{C.2}$$

where,

$$\begin{aligned}
\langle A\rangle_r &= \frac{1}{M}\sum_{i=1}^{M} A(\vec{x}_i)_r \\
\langle\langle A\rangle\rangle &= \frac{1}{R}\sum_{r=1}^{R}\langle A\rangle_r \\
\langle|\langle A\rangle|^2\rangle &= \frac{1}{R}\sum_{r=1}^{R}|\langle A\rangle_r|^2
\end{aligned}$$

M is the sampling size; r denotes each of R repetitions.

C.2 Monte Carlo Error of The Self-energy

Assume that $\vec{X}$ is a vector on a set of different value $\vec{k}$. $\vec{k}$ can be either a vector or scaler as either a complex number or real number. Therefore, the norm of $\vec{X}$ can be defined as

$$||X|| \equiv \sqrt{\sum_k |X(k)|^2}$$

Given R repetitions of Monte Carlo simulation on $\langle X(k)\rangle$

$$\sigma(X) = \sqrt{\frac{\langle||\langle X(k)\rangle_M||^2\rangle_R - ||\langle\langle X(k)\rangle_M\rangle_R||^2}{R}} \tag{C.3}$$

We can treat $\Sigma(k)$ as a vector, which component is a distinct value of 3-momentum k, in order to find a single (aggregate) Monte Carlo error of it. According to Equation C.3, for self-consistency iteration p,

$$\sigma(\Sigma) \quad = \quad \sqrt{\frac{\langle||\langle\hat{\Sigma}_r^{(p)}(k)\rangle_M||^2\rangle_R - ||\langle\langle\hat{\Sigma}_r^{(p)}(k)\rangle_M\rangle_R||^2}{R}}$$

and relative MC error is defined as

$$r(\Sigma) = \frac{\sigma(\Sigma)}{||\langle\langle\hat{\Sigma}_r^{(p)}(k)\rangle_R\rangle_M||}$$

Since the goal to calculate $\sigma(\Sigma)$ is for its variation among various repetitions. we can use $\Sigma(k)^{(r)}$ in the place of $\langle\Sigma\rangle_M$, because $\Sigma(k)^{(r)}$ contains the average of *score function* and it is obtained by *Monte Carlo* procedure.

Thus, after all, the MC error for the self-energy is

$$\sigma(\Sigma) \equiv \sqrt{\frac{\langle||\hat{\Sigma}_r^{(p)}(k)||^2\rangle_R - ||\langle\hat{\Sigma}_r^{(p)}(k)\rangle_R||^2}{R}} \tag{C.4}$$

C.3 Self-consistency Iteration Convergence Criterion

In the self-consistent algorithm, one of the most important aspect is to judge whether the convergence is achieved. We use the difference of self-energy $\Sigma(k)$ between two adjacent iteration to determine whether the self-consistent computation reaches convergence.

We denote the absolute and relative different between iterations as δ_a and δ_r respectively. The absolute difference of self-energy between iteration l and m

$$\delta_a \quad = \quad \frac{\sum_k |\bar{\Sigma}^{(l)}(k) - \bar{\Sigma}^{(m)}(k)|}{K} \tag{C.5}$$

where K is the number of all possible momentum-imaginary-frequency vector k on an N-site lattice with cut-off Matsubara frequencies, as defined in Section 3.8.

The corresponding relative difference is defined as relative difference between Iteration l and m:

$$\delta_r = \frac{\sqrt{\sum_k |\bar{\Sigma}^{(l)}(k) - \bar{\Sigma}^{(m)}(k)|^2/K}}{\sqrt{\sum_k |(\bar{\Sigma}^{(l)}(k) + \bar{\Sigma}^{(m)}(k))/2|^2/K}} \tag{C.6}$$

In our simulation, we set the self-consistency iteration convergence criterion for self-energy as the relative difference between two adjacent iterations $\delta_r < 0.001$. δ_r is usually 2 to 3 times larger than the relative Monte Carlo error $\sigma(\Sigma)$.

Appendix D

Fermi Liquid Theory

The Fermi liquid theory [27] describes an interacting behavior of the Fermion model near the Fermi surface ($\vec{k} \to \vec{k}_F$) at the temperature that is sufficiently close to zero ($T \to 0$) in the thermodynamic limit ($N \to \infty$) at low excitation energies $\omega \to 0$. The higher-order contribution to the self-eneryg $\Sigma_>(\vec{k}, \omega + i0^+)$ for $|\omega| \to 0$ is then asymptotically given by

$$\Sigma_>(\vec{k}, \omega + i0^+) \cong E^>_{\vec{k}} + (1 - Z_{\vec{k}})\omega + i(Y_{\vec{k}}\omega^p + X_{\vec{k}}T^p), \tag{D.1}$$

where the power $p \geq 2$, and $X_{\vec{k}}$, $Y_{\vec{k}}$ and $Z_{\vec{k}}$ are real functions of $\vec{k}$-vector. The corresponding Green's function $G(\vec{k}, \omega)$ is given by

$$G(\vec{k}, \omega) = [Z_{\vec{k}}\omega - (\epsilon_{\vec{k}} - \mu + \Sigma^{(1)}(\vec{k}) + E^>_{\vec{k}}) - i(Y_{\vec{k}}\omega^p + X_{\vec{k}}T^p)]^{-1} \tag{D.2}$$

The single-particle spectral weight function $A(\vec{k}, \omega)$ is composed of the coherent spectral weight $A_{coh}(\vec{k}, \omega)$ and $A_{inc}(\vec{k}, \omega)$

$$A(\vec{k}, \omega) \cong A_{coh}(\vec{k}, \omega) + A_{inc}(\vec{k}, \omega), \tag{D.3}$$

where $A_{coh}(\vec{k}, \omega)$ describes a low-energy quasiparticle peak

$$A_{coh}(\vec{k}, \omega) = \frac{1}{\pi Z_{\vec{k}}} \frac{\gamma_{\vec{k}}}{(\omega - E_{\vec{k}})^2 + \gamma^2_{\vec{k}}} \tag{D.4}$$

with the quasiparticle band energy $E_{\vec{k}}$ and the quasiparticle width $\gamma_{\vec{k}}$, which is defined as

$$\gamma_{\vec{k}} \cong \frac{1}{Z_{\vec{k}}}(Y_{\vec{k}}E^p_{\vec{k}} + X_{\vec{k}}T^p). \tag{D.5}$$

The integral of $A_{coh}(\vec{k}, \omega)$ and $A_{inc}(\vec{k}, \omega)$ are

$$\int d\omega A_{coh}(\vec{k}, \omega) = \frac{1}{Z_{\vec{k}}} < 1 \tag{D.6}$$

$$\int d\omega A_{inc}(\vec{k}, \omega) = 1 - \frac{1}{Z_{\vec{k}}} < 1 \tag{D.7}$$

The quasiparticle band energy $E_{\vec{k}}$ is described as

$$E_{\vec{k}} = \frac{1}{Z_{\vec{k}}}[\epsilon_{\vec{k}} - \mu + \Sigma^{(1)}(\vec{k}) + E^{>}_{\vec{k}}] \tag{D.8}$$

The Fermi surface is defined with the $\vec{k}$-vector, $\vec{k}_F$, as

$$E_{\vec{k}_F} = 0 \tag{D.9}$$